Dissertation
submitted to the
Combined Faculties for the Natural Sciences and for Mathematics
of the Ruperto-Carola University of Heidelberg, Germany
for the degree of
Doctor of Natural Sciences

presented by
Borja Aragüés
born in Zaragoza, Spain

Oral examination: May 20th, 2011

Nano-patterned, mechano-tunable, ECM mimetic substrates for cell adhesion studies under strain

Referees:
Prof. Dr. Joachim Spatz
Prof. Dr. Rainer Dahint

Abstract

Adherent cells are sensitive to physical and chemical cues in their environment and can adapt their response accordingly. Receptors in cells membrane are crucial elements in the recognition of such signals by binding external ligands (key-and-lock principle). Thereby these receptors and associated proteins transduce external cues in internal signals. Chemical nature of the ligands and their spatial arrangement can provide important information to the cells. In particular, spatial clustering of the ligands at the nanometer scale is considered to be a general principle by which the signal transduction of many biological processes gets modulated. Examples are the formation of focal adhesions (FAs) or of the immunological synapse. To investigate such clustering effects at the molecular scale, there is an immanent need for the precise chemical modification of surfaces.

Therefore, the aim of this work was to (i) develop a substrate on which the spatial arrangement of bound particles could be precisely controlled and varied at the nanometer scale, and (ii) to demonstrate the utility of such substrates in cell adhesion studies.

During this work an elastic poly(ethyleneglycol)-diacrylate (PEG-DA) hydrogel (HG) was used as carrier substrate on which an array of gold nano-particles (AuNPs) with well defined inter-particle distances (ΔL) was immobilized. ΔL could be successfully varied at the nanometer scale by mechanical stretching of the carrier substrate.

For cell adhesion studies the AuNPs were functionalized with a c(RGDfK) peptide so that integrin binding was preferentially invoked. Due to the protein repellent properties of PEG, the AuNPs constituted the only anchor points on which cells could adhere. Thereby nanometer precision on the spatial arrangement of the ligands was achieved. To show the versatility of PEG-DA HGs as bio-mimetic substrates, the surfaces of a series of HGs were homogeneously functionalized with Fibronectin (FN). Strain applied to the HGs was successfully transmitted to cells and FAs and their reaction to the strain and to the change in inter-ligand distances was monitored and analyzed. The anisotropy generated in the ligand array by the uni-axial stretching influenced cell adhesion. FAs reaction was more prominent when stretched on HGs + FN than on HGs + AuNPs + RGD.

In summary, fabrication of a material system for the dynamic variation of ΔL in the tens of nanometers was accomplished in this work. By rendering these substrates bio-mimetic, cell adhesion studies with dynamic variation of inter-ligand distances could be performed.

Zusammenfassung

Adhärente Zellen vermögen es sowohl mit physikalischen als auch mit chemischen Signalen in ihrer unmittelbaren Umgebung zu interagieren. Sogennante Zellmembranrezeptoren erfüllen dabei eine entscheidende Aufgabe. Sie vermögen es extrazelluläre Signale von spezifischen Liganden in intrazelluläre Signale umzuwandeln (Schlüssel-Schloss-Prinzip). Sowohl die chemische Natur dieser Liganden als auch ihre räumliche Anordnung übermitteln den Zellen wichtige Information. So vermag es die räumliche Anordnung der Liganden und Rezeptoren auf der Nanometerskala die Signaltransduktion vieler biologischer Prozesse zu modulieren. Beispiele dafür sind die Bildungen von fokalen Adhäsionskontakten (FAs) oder der immunologischen Synapse. Zur Untersuchung dieser Proteincluster und ihrer Wirkungsweise auf molekularer Ebene besteht ein zwingender Bedarf an präziser chemischer Oberflächenmodifikation.

Das Ziel dieser Arbeit war es (i) ein Substrat zu entwickeln, auf welchem die räumliche Anordnung von gebundenen Partikeln dynamisch auf der Nanometerskala kontrolliert und verändert werden kann und anschließend (ii) die Funktionalität eines solchen Substrates in Zelladhäsionstudien zu zeigen. Hierzu wurde ein elastisches auf Polyethylenglykoldiacrylat (PEG-DA) basierendes Hydrogel (HG) als Trägersubstrat verwendet, auf welchem regelmäßig angeordnete Goldnanopartikel (AuNPs) mit definierten Interpartikelabständen (ΔL) chemisch gebunden wurden. Diese Abstände konnten durch mechanische Dehnung des Trägersubstrats auf der Nanometerskala variiert werden. Für Zelladhäsionsexperimente wurden die AuNPs mit dem Peptid c(RGDfK) funktionalisiert, welches spezifisch an den Membranrezeptor Integrin bindet. Aufgrund der proteinabweisenden Eigenschaften des PEG-Hydrogels erwiesen sich die AuNPs als die einzigen Ankerpunkte für die Zellen. Somit wurde eine präzise räumliche Anordnung der Liganden in Nanometerbereich erreicht. Um die Vielseitigkeit von PEG-Hydrogelen als biomimetische Substrate zu zeigen, wurden diese ebenso homogen mit Fibronektin (FN) funktionalisiert. Die Dehnung der Hydrogele wurde auf die Zellen und ihre FAs erfolgreich übertragen. Die dadurch hervorgerufenen Zellreaktionen und die Veränderungen in ihrem Interligandabstand wurden analysiert. Durch die einachsige Substratdehnung wird die Ligandenanordnung variiert und somit die Zelladhäsion beeinflusst. Die Reaktion der FAs war ausgeprägter bei einer Dehnung von HGs + FN Substraten im Vergleich zu HGs + AuNPs + RGD Substraten.

Zusammengefasst wurde in dieser Arbeit die Anfertigung eines Substrates zur dynamischen Variation von Nanopartikelnabständen im Bereich von wenigen Nanometerzehnteln erreicht. Durch die Bio-funktionalisierung dieser Substrate konnten biomimetische Zelladhäsionsstudien mit einer dynamischen Variation von Interligandabständen durchgeführt werden.

Contents

I Introduction **1**

1 Mechano-sensing capabilities of the cells **3**
- 1.1 Cells and their environments . . . 3
  - 1.1.1 Homeostasis as a coordinative success . . . 3
  - 1.1.2 Ubiquitous forces acting on the cells *in vivo* . . . 3
  - 1.1.3 Cell responses tailored to the mechanical stimuli . . . 4
- 1.2 Mechano-transduction . . . 4
  - 1.2.1 Hierarchically coordinated process . . . 4
  - 1.2.2 Importance of the inter-ligand distance . . . 8
- 1.3 Bio-physical models describing FAs . . . 8

2 Mechano-tunable, nano-patterned, stretchable ECM-mimetic substrates **13**
- 2.1 The setup . . . 13
- 2.2 Nature of the scaffold . . . 14
  - 2.2.1 ECM-mimetic polymeric scaffolds and their applications in science . 14
  - 2.2.2 Poly(ethylene glycol) hydrogels . . . 15
- 2.3 Patterning of the surface: Poly(ethylene glycol)-diacrylate . . . 16
  - 2.3.1 Block Copolymer Micellar Nano-lithography (BCMN) . . . 16
  - 2.3.2 Transfer nano-lithography and functionalization with RGD motif . . 18
  - 2.3.3 Copolymerization of the PEG-DA chains with carboxyl moieties . . 18
- 2.4 Mechanical traction of the functionalized HG . . . 20
- 2.5 Summary of the substrates fabrication . . . 21

II Materials and Methods **23**

3 Fabrication of the substrates **25**
- 3.1 Polymeric, ECM-mimetic, elastic scaffolds . . . 25

3.2 Functionalization of the HGs' surface 26
3.2.1 Self-assembly of the nano-pattern by BCMN 26
3.2.2 Transfer nano-lithography 27
3.2.3 Casting of the prepolymer in the customized mold and UV photo-polymerization 29
3.2.4 Copolymerization of the PEG-DA chains with carboxyl moieties . . 30
3.3 Surface characterization 31
3.3.1 Scanning Electron Microscope and cryo SEM 31
3.3.2 Scanning Probe Microscope 31

4 Experimental Design **33**
4.1 Cell system 33
4.1.1 Maintenance of cells in culture 33
4.1.2 Cell seeding 33
4.2 Uniaxial, static stretching 34
4.2.1 Important elements of the stimuli unit 34
4.2.2 Stretching procedure 36
4.3 Live-cell imaging: Optical microscopy 36
4.3.1 Differential Interference Contrast microscopy (DIC) 36
4.3.2 Fluorescence microscopy 37
4.3.3 Integration of complementary software: A custom-written Visual Basic for Applications (VBA) program 37
4.4 Experiment description 37

5 Image processing and analysis **39**
5.1 Requirements of the data analysis 39
5.2 Image processing with ImageJ 40
5.2.1 Processing of the images acquired with the AxioCam MRm CCD camera 40
5.2.2 Custom self-written routines for image analysis 40
5.3 Data analysis with MatLab 44
5.3.1 Extracting the information from the text files of each position for the different conditions 44
5.3.2 Data segmentation 44
5.3.3 Statistics and plotting 45

III Results and Discussion **47**

6 Characterization of the ECM-mimetic, elastic PEG-DA HGs **49**
6.1 Self-assembly of the nano-pattern by BCMN 49
6.2 Transfer of the AuNPs to a stretchable substrate 51

6.3 Cell adhesion on ECM-mimetic, elastic PEG-DA HGs 53
6.3.1 Functionalization with the RGD motif to control the biochemical signals 53
6.3.2 Stiffness of the substrates 54
6.4 Uniaxial, static stretching of the HGs 55
6.4.1 Stretching method combining casting and pulling 55
6.4.2 Characterization of the strain field 60
6.4.3 Anisotropy in the AuNPs pattern 60

7 Cell response to uniaxial, static strain 63
7.1 REF-YFP-Pax cells morphology on the HGs 63
7.2 Transmission of strain to cells and FAs 65
7.2.1 Cell adhesion under strain 65
7.2.2 Quantification of strain applied to the cells and FAs 66
7.3 Analysis of cells' temporal change in the stretched state 70
7.4 Analysis of FAs' temporal change in the stretched state 75

IV Conclusion and Outlook 81

8 Nano-patterned, mechanotunable substrates 83
8.1 Applicability of the setup 83
8.2 Temporal change of cells and of FAs response in the stretched state 83
8.3 Outlook 84
8.3.1 Further experimentation 84

List of Figures 87

Bibliography 91

A Appendix 105
A.1 Abbreviations 105
A.2 ^{1}H-NMR-Characterization of PEG-DA modification 106
A.3 Customized VBA macro 106
A.4 Strain Analysis 108
A.5 Evolution in time of FAs' parameters discriminating between small and large particles 110
A.6 List of publications 112

Part I

Introduction

Chapter

1

Mechano-sensing capabilities of the cells

1.1 Cells and their environments

1.1.1 Homeostasis as a coordinative success

A human body is the synergistic sum of about 10^{13} cells acting in a globally coordinated, yet locally tailored manner to environments and forces. This coordination entails a clear hierarchy that down-scales from entity, to systems, organs, tissues, cells, cell-organelles, protein clusters and finally molecules, all of them working in coordinated homeostasis: a state of inner stability in an environment with fluctuating conditions. Each hierarchical level is differentiated serving specialized purposes and posing different requirements. We undoubtedly exist in an environment where the scarcity of resources leads to tough competition. Since the earliest of ancient times synergistic collaborations between complementary modules of growing complexity have brought the key to efficiency, adaptation and ultimately to survival over less developed assemblies (sometimes at the expensive cost of entropy): from atoms to molecules, amino-acids, proteins, nucleic acids, prokaryotes, eukaryotes and finally to multi-cellular organisms.

1.1.2 Ubiquitous forces acting on the cells *in vivo*

Development biology is a scientific discipline not yet fully-understood with still many open questions. Likewise, tissue physiology and the epigenetic factors* accounting for a wide variety of diseases are unknown. Tissue homeostasis and cell fate is often influenced by physical cues [Alenghat and Ingber, 2002, Ingber, 2004, Wang and Thampatty, 2006]. In all living organisms, cells are constantly subjected to a compendium of changing forces and physical signals and there is already some understanding on how forces acting at the organ level may affect functioning of cells at the tissue level and dictate either a healthy existence or a fatal disease (Figure 1.1 [Shefelbine et al., 2005]).

---

*Non-genetic factors that cause phenotypic changes

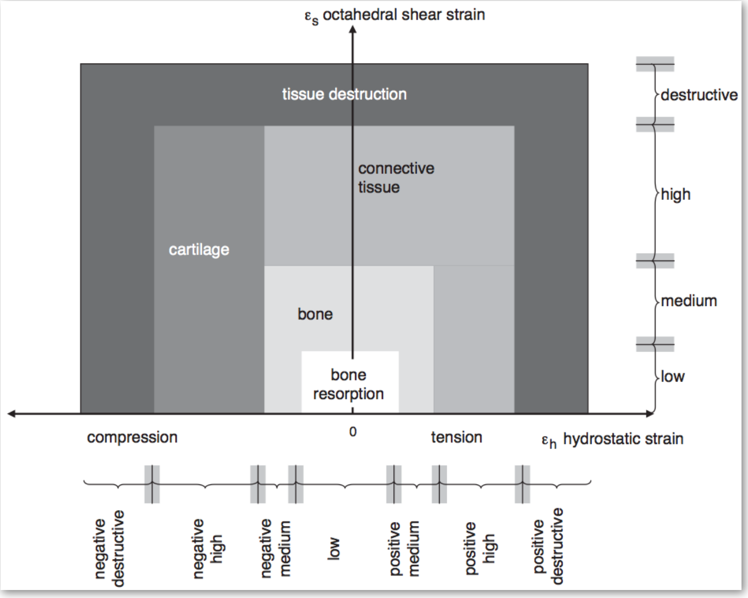

Figure 1.1: Representation of how the magnitude of hydrostatic strain (x-axis) and octahedral shear strain (y-axis) dictate cell phenotype *in vivo* and may even lead to tissue destruction [Shefelbine et al., 2005].

1.1.3 Cell responses tailored to the mechanical stimuli

Literature abounds in articles describing how cells effectively react in a coordinated, specific, localized manner to external stimuli and how, in turn, they are capable of influencing it by producing integral components or exerting forces to further structure it [Hahn and Schwartz, 2009, Ingber, 2006, Jaalouk and Lammerding, 2009]. A clear example is how soft substrates that mimic the brain are shown to be neurogenic, stiffer substrates that mimic muscle are myogenic, while rigid substrates that mimic bone are osteogenic [Engler et al., 2006]. It is also well known how fibroblasts and endothelial cells can not spread efficiently on surfaces softer than 3 kPa because of their incapacity of generating enough tension [Pelham and Wang, 1997, Yeung et al., 2005] or how other cells adapt their functions and morphologies to the periodic pulsation or the shear forces in blood vessels [Schwartz, 2009, Wang and Thampatty, 2006]. Furthermore, lower-level assemblies like Triton cytoskeletons [Sawada and Sheetz, 2002] or even smaller structures [Schwarz and Bischofs, 2005] have been shown to transduce matrix forces. Notably, FAs grew in response to force to achieve coefficients of proportionality of $5\,nN/\mu m^2$ [Balaban et al., 2001]. For a comprehensive review of the effect of cell stimulations on cells see Wang and Thampatty [2006]

1.2 Mechano-transduction

1.2.1 Hierarchically coordinated process

Mechano-transduction is defined as the conversion of external mechanical stimuli into internal cell signals. Cells are organized hierarchically hence the global coordination of mechano-transduction can be expected to be hierarchical too.

Cells and cytoskeleton

Tensegrity model describes whole cells as an equilibrated balance of counteracting forces generated by the different but complementary elements of the cytoskeleton [Ingber, 1993]. Cells consist of tense elements (myosin II motors acting on actin filaments) physically linked to a second subset of elements that resists compression (microtubuli), bringing the whole system to an isometric tension and yielding an overall very stable construction. Furthermore, depending on the mechanical characteristics of their native environments tension maintained by the cells will have a specific magnitude, higher in stiffer surfaces where cells can apply higher tensions. This is indeed one of the proposed mechanisms by which cells can adapt their mechanical properties and their reactions to their surroundings. This mechano-sensitive feedback loop between inner tension and external environment modulates cellular functions as diverse as migration, proliferation, differentiation and apoptosis, and is crucial for organ development and homeostasis. Figure 1.2 depicts a simplified representation of how mechanical events can elicit cellular responses. Although mechano-sensing and mechano-transduction have been the focus of extensive decades of research, still basic questions arise as to what the actual underlying mechanism is: How do cells adapt to an ever-changing environment? How is it possible that *in vitro* the rigidity preferences of cells generally reflect their native environments? How can cells generate, sense and respond to physical forces? What dictates cells their specific long-term lineage?

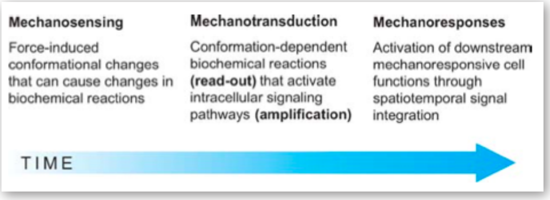

Figure 1.2: Progress in time of how mechanical events can elicit cellular responses. Force sensitive molecules cause biochemical reactions that are amplified through signaling pathways and influence mechanoresponsive cells functions [Vogel, 2006].

What set of tools do cells (the fundamental unit of structure, function and organization in all living organisms) have when it comes to the sensing of their surrounding environment? Although the principles of how specialized cells respond to mechanical stimuli are highly conserved among organisms [Coombs et al., 2002, Gillespie and Walker, 2001, Ingber, 2006] it's a two-way communication pathway in which despite cross-cultural, multinational and multidisciplinary efforts many milestones have remained obscure. Figure 1.3 shows the suggested mediators of cellular mechano-transduction [Ingber, 2006].

Since this work's focus lays in cell adhesion to their underlying substrate we will pay a closer attention to those elements involved in this process: cell-extra cellular matrix (ECM) adhesions (FAs and integrins) and components of the ECM (FN, collagen, proteoglycans and the basement membrane).

Focal adhesions and integrins

FAs as the points of molecular interaction between cells and ECM are of paramount relevance. Abundant papers have been written about the spatiotemporal evolution of these structures and how for example their coordinated assembly-maturation-disassembly

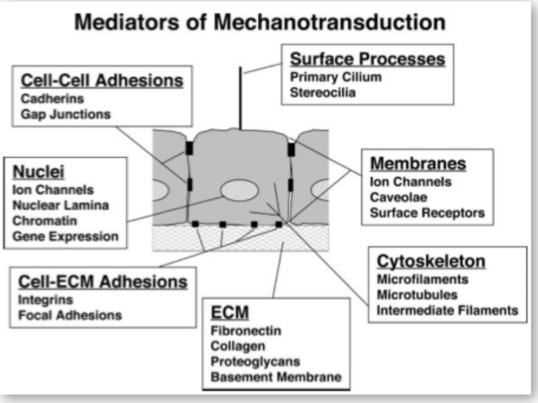

Figure 1.3: Representation of a cell and the proposed mediators of mechano-transduction [Ingber, 2006].

facilitates the locomotion of cells [Doyle et al., 2009, Lauffenburger and Horwitz, 1996, Vicente-Manzanares et al., 2005, Wolfenson et al., 2009]. More notably, these structures have been shown to be reactive to the levels of tension applied upon them with coefficients of force to surface proportionality of $(5\,nN/\mu m^2$ [Balaban et al., 2001]) proving their relevance as multifunctional mechano-sensing organelles. Proof of that is how FAs are involved in force transmission, cytoskeletal regulation and signaling [Bershadsky et al., 2003, Geiger et al., 2001, 2009, Papusheva and Heisenberg, 2010, Riveline et al., 2001]. FAs are basically a dense network [Zaidel-Bar et al., 2007] containing more than 80 types of proteins (commonly referred to as “plaque proteins”) located at the interface between the transmembrane adhesion receptors and the actin cytoskeleton.

Quite recently [Kanchanawong et al., 2010] more information on the molecular architecture of such structures has been obtained showing it is strata-based and that each layer has a definite composition and function. Grouped around the vertical scaffolding protein talin the following strata can be noticed: 1) an integrin signaling layer containing integrin cytoplasmatic tails, focal adhesion kinase and paxillin; 2) an intermediate force-transduction layer containing talin and vinculin; and 3) a topping actin regulatory layer containing zyxin, vasodilator-stimulated phosphoprotein and α-actinin. Furthermore, this layered structure apparently holds true for FAs of varied sizes and morphologies and even across two quite different cell lines suggesting a cell-type independent ”functional stratifying” that persists throughout FAs maduration stages. Figure 1.4 shows the suggested architecture.

Integrins as the most-extern element of the cells bridging their cytosolic components to the ECM play a crucial role in mechano-transduction [Ingber, 1991]. Integrins are obligate heterodimers containing two non-covalently associated transmembrane subunits, termed α (alpha) and β (beta) subunits. Each subunit contains a separate tails that penetrates the plasma membrane and possesses a small cytoplasmic domain [Hynes, 2002]. In mammals, eighteen α and eight β subunits have been characterized that may form 24 different heterodimers. The combination of these determines the ligand specificity of the integrin. Furthermore, to date there are five mechanisms that have been proposed as to how cells can effectively sense through integrins [Moore et al., 2010]:

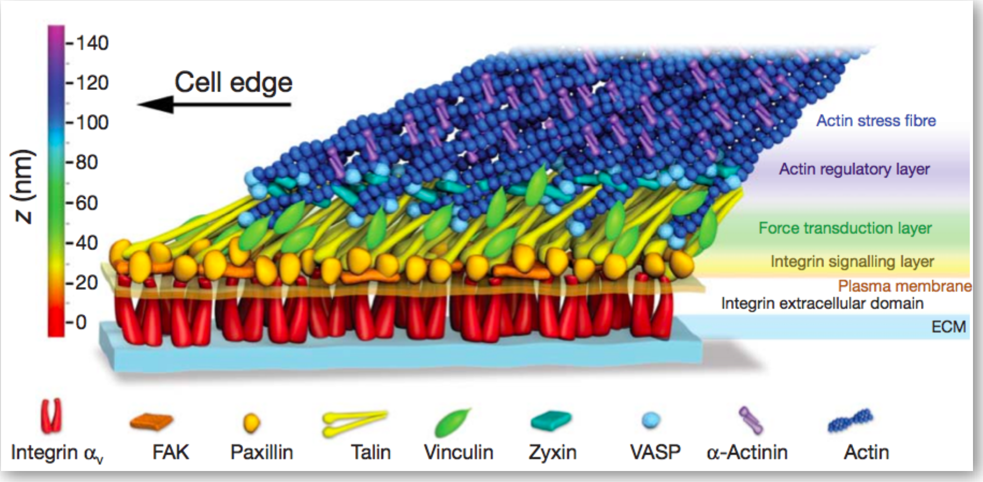

Figure 1.4: Detailed representation of a FAs' architecture. Three layers can be distinguished as one passes from the ECM to the actin stress fibres following the z-axis [Kanchanawong et al., 2010].

- **Catch bond formation:** A subset of interactions that counter-logically strengthen when a force is applied on them [Kong et al., 2009].
- **Channel opening:** Force perpendicular to the membranes where the channels are embedded or cytoskeletal forces pulling from the earliest stages from an adhesion complex which shall be associated to the channel via integrins [Sukharev and Corey, 2004].
- **Enzyme regulation:** Kinases, phosphatases, adenylate cyclases and GTPases changing their kinetics in response to mechanical stimulation [Cooper et al., 2003].
- **Exposure of phosphorylation sites:** Marked increase of tyrosine phosphorylation by cell stretching and matrix stiffening [Glogauer et al., 1997, Pelham and Wang, 1997].
- **Exposure of binding sites:** Exposure of protein-protein binding sites by stretch [Rio et al., 2009, Vogel, 2006].

It would be almost naïve to think that one single element of the list acts as THE mechano-sensor at the integrins level, but rather that a combination of several of them acting perhaps at different stages and localizations sums up yielding a force-induced cell reaction.

ECM elements: Fibronectin and RGD motif

FN is a 230–250 kDa dymeric glycoprotein that consists of two poly-peptidic chains each presenting repeats of types *FnI*, *FnII* and *FnIII* [Vogel, 2006]. The subunits are interconnected through two disulfur bonds. FN contains specific binding sites to several other proteins involved in cell adhesion mediation. Among them we can find collagen binding sequences, heparin binding sequences and the so called "RGD" sequences, a tripeptide motif consisting of arginine (R), glycine (G) and aspartic acid (D) identified already almost thirty years ago as the minimal essential cell adhesion peptide sequence in FN [Pierschbacher and Ruoslahti, 1984]. The RGD motif is, as a matter of fact, the most effective and most often employed peptide sequence for stimulated cell adhesion on synthetic surfaces [Hersel et al., 2003] being able to address more than one cell adhesion receptor. From the many variants that to date exist, the peptides in a cyclic form have improved activity and receptor selectivity [Kessler] as it is known that different integrins distinguish differences in the conformation and sequential environment of various RGD sites [Pfaff et al., 1994].

1.2.2 Importance of the inter-ligand distance

A great contribution to the understanding of integrin signaling was the determination of the minimum ligand density essential for a stable assembly of the FAs [Arnold et al., 2004, Cavalcanti-Adam et al., 2007]. Since a RGD-motif was used as ligand bound to the particles, integrins were invoked in the adhesive process. Under the assumption that due to sterical hindrances only one integrin binds per motif, it could be demonstrated that there is a critical inter-ligand spacing of 73 nm over which immature adhesions fail to develop into focal adhesions and the number of cells per mm^2 decreases dramatically (Figure 1.5 **(A)**). Moreover, as observed in the lower part of the figure, the turnover of the FAs increases correlative with an increasing inter-ligand distance demonstrated by the color-shift from red-yellow to bluish in the paxillin (Figure 1.4) containing structures (red means old, yellow means unchanged and blue means new). This indicates that the dynamics of FAs turnover are sensitive to the inter-ligand distance.

1.3 Bio-physical models describing FAs

The main difference between the bio-physical models describing FAs lies in the physical principles that account for the mechano-transduction. As presented in Bershadsky et al. [2006] and depicted in figure 1.6 three physical principles may be the underlying cause: Stress (force), strain (deformation) or chemical potential. Each model poses different physical requirements and hence can be assessed in terms of their feasibility.

Stress models rely on molecular switches reacting to the force by modifying their state from inactive to active [Bruinsma, 2005, Vogel, 2006]. For the model to hold true the thermodynamic work produced by the stress has to decrease the activation energy of the molecular switch transition to an extent that it is energetically favorable. Equation 1.1[†] represents the energy produced by the stress. In order for the stress to be sensed, the conformational transition must produce a protein stretching of ΔL. This value can be estimated from the $|\Delta F|$ (that must at least exceed the characteristic thermal energy as

---

[†] γ is the lateral tension of the protein; L_{per} is the protein's linear dimension.

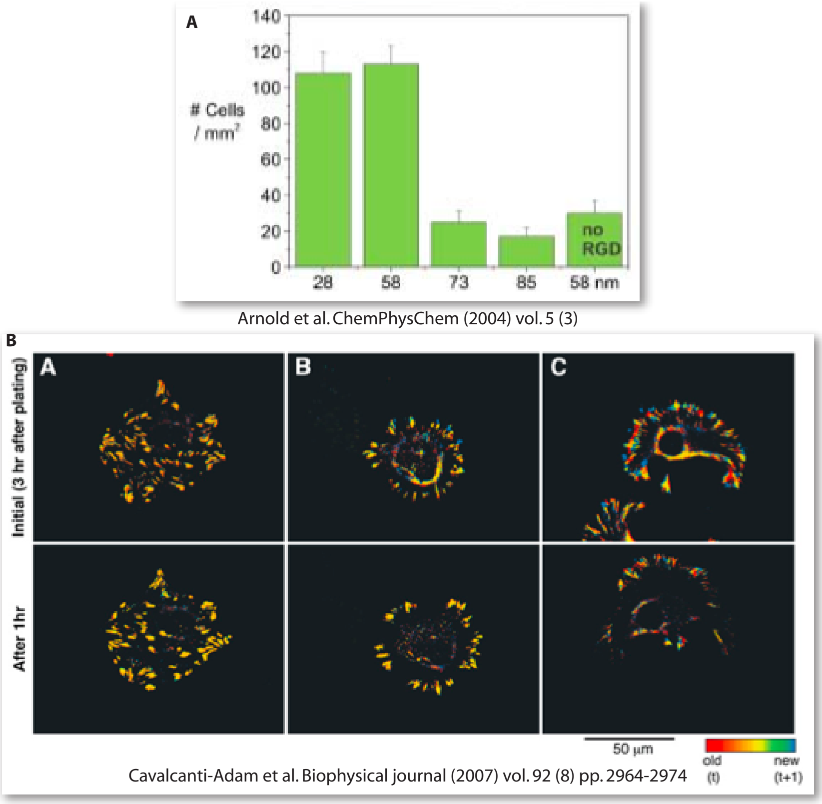

Arnold et al. ChemPhysChem (2004) vol. 5 (3)

Cavalcanti-Adam et al. Biophysical journal (2007) vol. 92 (8) pp. 2964-2974

Figure 1.5: (A) Effect of the inter-ligand spacing in cells adhesion capabilities: at a value of 73 nm the number of cells per mm^2 decreases dramatically. **(B)** FRIT images (fluorescence ratio of images at different time points) of movies showing REF cells transfected with YFP-paxillin on (A) control surface, (B) 58 nm, and (C) 108 nm RGD-nanopattern in initial and after 1 hour conditions. The images are temporal ratios of two consecutive frames: structures that appear only at the later image are shown in blue, whereas structures present at the earlier time point are red. Unchanged paxillin locations are represented in yellow.

shown in Equation 1.2[‡]) and the knowledge that $\gamma \cdot L_{per} \approx 1\,pN$ [Balaban et al., 2001]. This results in a $\Delta L > 4\,nm$ which is in the order of magnitude of the protein itself and hence a caveat of this model.

$$\Delta F = -\gamma \cdot L_{per} \cdot \Delta L \tag{1.1}$$

$$|\Delta F| > k_B T \approx 0.6\ kcal/mol \tag{1.2}$$

Strain models hypothesize that there is a mechano-sensor switch that reacts to either extension or compression and to changes on protein affinity [Besser and Safran, 2006, Nicolas and Safran, 2006, Nicolas et al., 2004]. FAs are modeled as a two-layers structure, one being deformed by the acting force (upper layer linked to the actin cytoskeleton) and

---

[‡] k_B is Boltzmann constant and T the absolute temperature.

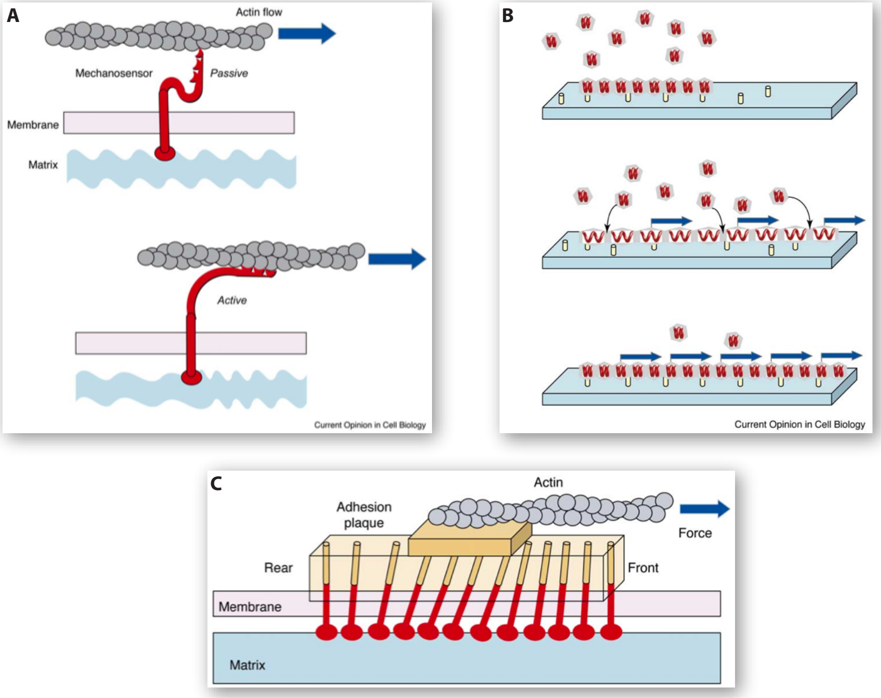

Figure 1.6: Theoretical models accounting for FAs evolution under mechanical stimuli. **(A)** Strain model. **(B)** Thermodynamical model. **(C)** Strain Model. [Bershadsky et al., 2006]

the lower attached to the substrate and containing integrins. Strain sensing relies in the dependence of the upper layer's affinity on the deformation of the underlying mechano-sensing layer: a deformation should compress the front edge of the underlying mechano-sensing layer increasing its affinity for the plaque proteins and leading to a grow of the FA in the direction of the force application (anisotropic growth). In order for the process to be energetically favorable the sensor layer's stretching-compression rigidity κ must have a value larger than $0.15\,mN/m$ (Equation 1.3 where α is the binding-coupled deformation $\approx 5\,nm$) which is in the order of magnitude of the stretching rigidities of other biological materials [Gittes et al., 1993] and hence realizable.

$$\kappa > (k_B T)/\alpha^2 \tag{1.3}$$

Finally, thermodynamical models defend that the FAs are elastic in nature and are stretched upon the imposition of a stress. As an effect of the stretching stress, the chemical potential of the plaque proteins is reduced thereby enhancing the assembly as it becomes favorable that new plaque molecules are added to the ensemble (isotropic growth) [Shemesh et al., 2005]. It implies, as mentioned above, the elastic nature of the FA plaque and its ability to incorporate new proteins without getting ruptured in the process. As candidate for such peculiar roles, proteins from the formin family are proposed [Faix and Grosse, 2006, Kovar, 2006]. According to the authors, thermodynamical models are the only models accounting for all the FA mechano-sensing phenomenological behaviours observed so far.

More importantly, the monitoring of FAs evolution in time in response to an externally induced stimuli can be performed by means of light and fluorescence microscopy as they involve μ-scaled features of the cells (silhouette of the cells or the FAs). An observed growing at the front edge (relative to the acting force) will support the strain model, whereas an uniform grow will do for the thermodynamical model.

Chapter

2

Mechano-tunable, nano-patterned, stretchable ECM-mimetic substrates

2.1 The setup

Herein we propose the application of a previously described modular, tunable substrate [Graeter et al., 2007] to perform cell adhesion studies under mechanical strain. In vivo, cells are surrounded by the extracellular matrix (ECM) which possesses determined mechanical, structural and biochemical properties. In an attempt to bring our laboratory practices closer to the natural environment cells encounter, we have envisaged a setup with a series of characteristics that we can arbitrarily vary so we have a combination that mimic these properties. Figure 2.1 shows the micro-, and nano-tools we have at our disposal in our attempt to dissect some guiding principles of cell adhesion events.

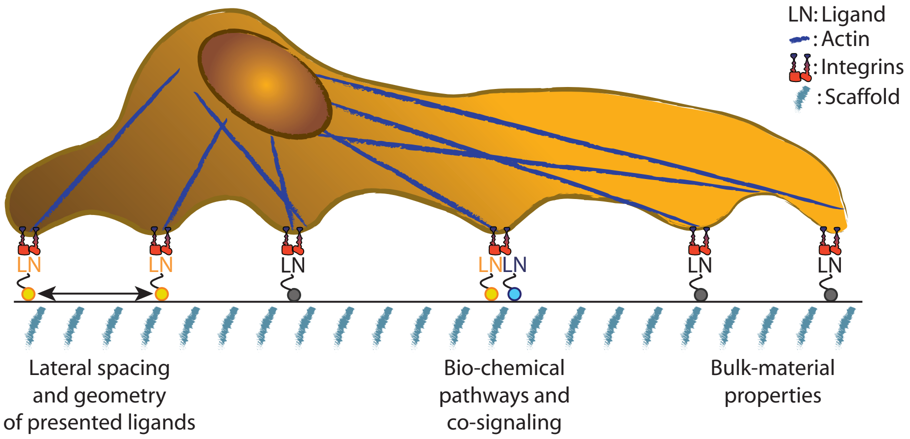

Figure 2.1: Outside-in cell signaling. A bio-engineered scaffold can present cells with varied, tunable features such a deterministic presentation of anchoring points, the choice of determined bio-chemical pathways or different bulk-material properties

What features of the scaffold can we control? First, the nature of the underlying substrate which will serve as support for the cells and as vehicle to transmit the applied stimuli. Second, the geometry and the distance between the biochemical ligands the cells will be presented with, as well as about the very nature of the motives presented. Finally, the method of choice to transmit an uniaxial, static strain to the substrates. In order to be able to address the pertinent questions there are certain requirements the setup has to comply with. The clearer challenges we face are: How to render the surface of the scaffold inert to protein adhesion so that we can control the anchoring points of the cells? How to position the anchoring points on the substrates' surface with a nano-metric spatial resolution? How to apply in a consistent and reproducible manner the uniaxial, static load to the substrates? How to monitor the cell reaction in the relevant time range, extract a valid data-set from the images and process and present the results reliably?

2.2 Nature of the scaffold

Requirements on the scaffold:

1. **Biocompatibility similar to ECM:** The two most important parameters are stiffness (so that cells can build effectively their cytoskeleton and reach an inner homeostatic tension) and of course toxicity.

2. **Support mechanical loading elastically** so we can plan more complex experiments in the future, such as a combination of stimuli and relaxation or a cyclical type of loading.

3. **Protein repellent** in order to force the cells to adhere only on the anchor points we provide.

4. **Surface decoration:** It has to invoke integrin signaling pathway: RGD-motif. Furthermore, small ΔLs are needed so we can stretch without overcoming the critical ΔL that permits a successful adhesion.

2.2.1 ECM-mimetic polymeric scaffolds and their applications in science

Polymeric scaffolds have been used extensively in the field of tissue engineering during the last decades [Drury and Mooney, 2003, Lee and Mooney, 2001, Lutolf and Hubbell, 2005]. They can be used to deliver bioactive molecules in a controlled manner, as three-dimensional scaffolding platforms presenting cells with stimuli that promotes the formation of a desired tissue, or as mere space-filling agents. Generally, the scope of tissue engineering is to fabricate living replacements of parts of the body but simplified versions are used in basic research too. An essential property of these scaffolds is *biomimicry*: the possession of salient material features of natural ECM molecules that turns scaffolds in a close synthetic replica of the conditions and signals cells encounter in their native micro-environments: cell-binding signals, cell-cell adhesive interactions, soluble growth factors and mechanical stimuli.

2.2.2 Poly(ethylene glycol) hydrogels

In vivo the external region of a cell membrane is a glycoprotein-polysaccharide cover known as the glycocalyx, a dense network of highly hydrated glycosylated molecules. Due to the maximization of entropic repulsion and the associated steric hindrances, this cover constitutes a shield against non-specific adhesion [Holland et al., 1998]. The desired cell-cell, cell-surface interactions are then mediated through the specific interaction between cell-surface receptor molecules [Anselme, 2000, Zanini et al., 2010]. The combination of non-specific resistance and specific interaction constitutes a fascinating mechanism by which cells attain high selectivities in the connections with their immediate environments. PEG-based hydrogels (HGs) can mimic this mechanism: PEG has excellent antifouling properties having been found to construct similar glycocalyx-mimic surfaces [Fan et al., 2006, Gombotz et al., 1991, Harris, 1992, Merrill, 1987, Ostuni et al., 2001, Schwendel et al., 2001]. Due to its hydrophilic character PEG gets hydrated exhibiting many of the structural, physical and chemical properties characteristic of the ECM [Hoffman, 2001]. HGs are basically highly hydrated polymer materials composed of hydrophilic polymer networks that may absorb from 10–20 % up to thousands of times their dry weight in water [Harland and Prud'homme, 2009]. HGs because they have structural similarity to the macromolecular-based components in the body and are considered to be biocompatible [Drury and Mooney, 2003, Hoffman, 2001, **?**]. What are the choices in terms of HGs?

- **Type of the HGs:** physically cross-linked (reversible interaction) or chemically cross-linked (permanent interaction HGs.
- **Composition:** natural polymers (Collagen and gelatin, hyaluronate, fibrin, alginate, agarose, chitosan) vs. synthetic polymers (Poly(acrylic acid) and its derivatives, poly(ethylene glycol) (PEG) and its copolymers, poly(vinyl alcohol), polyphosphazene, polypeptides).
- **Molecular structures:** Linear polymers, block copolymers, graft copolymers, inter-penetrating networks or polyblends.

In order to form the HG the macromers have to be interconnected as otherwise they would get dissolved in water during the swelling process: the interaction can be reversible (physical or ionic) or permanent (chain-growth [Zhu et al., 2009], step-growth [Lutolf and Hubbell, 2003] or even copper-free click chemistry [DeForest et al., 2009]). We cross-linked the macromers chemically so that the polymerized network could withstand the mechanical stretching. In terms of composition, whereas natural polymers may either be components or have similar properties to the natural occurring proteins of the ECM, their chemistry and properties are usually not controllable and reproducible, so we work with PEG synthetic polymers (section 2.2.2). Given that the final polymerized network does not need to include advanced features, we work with simple linear monomers as building blocks. The optimal choice of more reactive functional groups replacing the PEG's hydroxyl end-groups chains will be one that allows us to cross-link them together plus simultaneously to add receptors that promote specific cell-substrate interactions. In the literature a broad variety of end-groups have been used to create PEG HGs: isocyanates, methacrylates, acrylates [Watkins and Anseth, 2005], cinnamylidene acetate, nitrocinnamate and urethane, among others [Krsko and Libera, 2005]. In this work acrylate groups were used because they have kinetics in the order of minutes (are hence easily controllable) and are heavily used in the group.

2.3 Patterning of the surface: Poly(ethylene glycol)-diacrylate

As mentioned above, one of the salient properties of PEG-based HGs is their repellant nature against protein adsorption. In order for PEG-based HGs to mimic glycocalyx surfaces, they need to additionally present cells with specific adhesion-motives as a customized decoration, i.e. they must be patterned. Patterning is the process by which a material is structured in two or three dimensions. At the nano-, and micro-scale pattern features are at the scale of proteins and cells, respectively. A decisive criteria is hence the minimum feature size achievable by a patterning method, on the order of few microns for photolithographic patterning (small-molecule diffusion in the pre-polymer mix) or at the nano-scale for electron-beam patterning. Photolithographic polymerization was chosen basically because the setup is much simpler and the procedure faster. In order to overcome the main caveat of photolithographic polymerization (patterning at the micro-scale) we obtained previously the necessary nano-lateral resolution by means of a self-assembly procedure and then such nano-pattern was transferred to the HGs. In order to incorporate other molecules or functional groups to the HGs' surface it suffices to add an acrylate group to the feature of interest and mix it with the macromers. During the photo-polymerization the acrylate moities will get covalently bound and the features of interest will belong to the polymerized network.

2.3.1 Block Copolymer Micellar Nano-lithography (BCMN)

Amphiphiles (from Greek *"amphis"*: both, *"philia"*: love) are molecules that consist of both a hydrophobic and a hydrophilic part. When such molecules are put in contact with a solvent they will adapt an orientation where the domain with the highest affinity for the solvent will face toward that solvent and the less affine part will be turned to avoid contact with the solvent. Under these conditions, amphiphilic molecules self-assemble and give rise to a large variety of micro-topologies with an assembly architecture determined by the ratio between the size of the hydrophilic and the hydrophobic parts as well as the nature of the solvent. Solvent parameter (in some studies related to Hildebrand solubility parameter) is a quantitative measure of the capability of solvents for interaction with solutes (IUPAC), i.e. a numerical estimate of the degree of interaction between materials. Materials having similar values are likely to be miscible, whereas those with disparate values tend to segregate. See Figure 2.2 for a visual description of these processes [Förster and Antonietti, 1998, Förster et al., 1996]. The simplest kind of polymeric amphiphiles are diblock copolymers, synthetic molecules where two antagonistic parts (A and B) have been tethered together. Following the commonly used nomenclature A is the part affine to the solvent and becoming the solvated, highly stretched corona and B is the part antagonistic to the solvent and hence forming the melted core. The three main parameters characterizing A–B diblock copolymers are the degree of polymerization, $N = N_A + N_B$, the composition, $f_A = N_A/N$, and the Flory–Huggins interaction parameter χ between the monomers A and B [Förster et al., 1996].

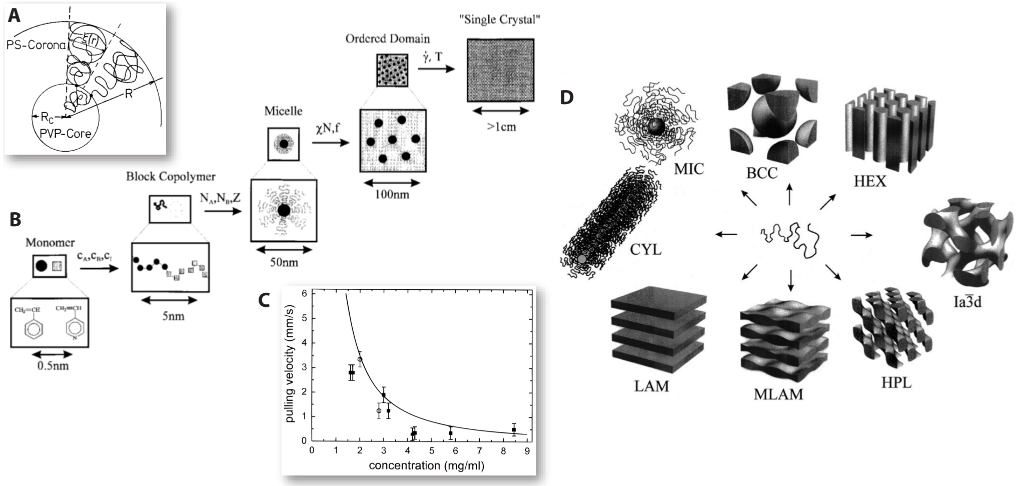

Figure 2.2: Block-copolymer micellar nano-lithography. **(A)** Detailed representation of micelles architecture. **(B)** Scaling hierarchy of the self-assembly process [Förster and Antonietti, 1998]. **(C)** Relation between concentration of the micellar solution and the retraction velocity needed to obtain a monolayer on the dip-coated substrates. **(D)** Structures obtainable by the right choice of diblock-copolymers and selective solvent [Förster and Antonietti, 1998].

Notably, it has been widely shown that under determined conditions the adsorptions of diblock copolymers from a selective solvent followed by a rapid solvent extraction can lead to highly ordered lateral microstructures [Gao and Eisenberg, 1993, Krishnamoorthy et al., 2006a,b, Spatz et al., 1995, 1996a,b]. One such system is poly(styrene)-block-poly(2-vinylpiridine) (P(S-b-2VP)) solved in toluene (a selective solvent for the PS block). The micellar core-shell structure can be seen as a nano-reactor allowing the selective loading of metal precursor salts into the P2VP core (coordination between the gold salt's anions and the positively charged PVP units). Via dip-coating [Glass et al., 2003, 2004] large areas are covered with high accuracy and hence reproducibility.The immersion of the substrate in the solution is irrelevant as free polymer chains bind to the surface resulting in a polymer brush. It is actually during the retraction of the substrate out of the micellar solution that the micelles form a monolayer on the substrate [Antonietti et al., 1994] through a precipitation of the micelles from the solution [Meiners et al., 1997]. The important parameter is the speed of retraction necessary to obtain a film thickness which contains enough polymer to form a closed packed hexagonal lattice of loaded micelles. The driving force is the evaporation of the toluene at the immersion edge. Through the complete removal of copolymers by plasma treatment a pure array of nano-particles is created with the original arrangement of micelles.

The micelle size is controlled by the tendency toward separation to a non-soluble micelle core as well as by the osmotic repulsion of the solvating chains once assembled in the micelle. The osmotic repulsion is directly proportional to the molecular weight of the solvating blocks and tends towards a maximum accessible volume realized in the spherical morphology [Antonietti et al., 1994]. Consequently, anisometric micelles can only be observed in the case of small solvating chains or of bad solvents conditions where this beneficial (for the shape) stretching is not so energetically favored.This is one of the potential reasons why with small diblock copolymers a broader size distribution of micelles is obtained [Rabani et al., 2003] leading to arrays of nano-particles without long range order.

2.3.2 Transfer nano-lithography and functionalization with RGD motif

Transfer nano-lithography is the technique developed in the group that allows the transfer of AuNPs from a rigid substrate to PEG-DA based HGs [Graeter et al., 2007]. The ordered array of AuNPs are incubated with a thiol-acrylate linker. Through the acrylate moiety the linker will get cross-linked with the acrylate groups in the PEG-DA macromers during the UV photo-polymerization step acting as a bridge between the AuNPs and the macromers (a sort of cross-linkable ”fingers” grabbing on the particles). During the swelling process of the polymerized HGs the particles will detach (lateral forces) from their rigid support and become the decoration of the elastic substrates. A detailed representation of the radical chain-growth photo-polymerization follows in Figure 2.3.

The AuNPs were finally functionalized with a peptide containing the RGD motif and shown in figure 2.4 (kindly provided by Prof Kessler at the Technische Universität München) in order to invoke integrin ($\alpha_v\beta_3$, $\alpha_5\beta_1$ and $\alpha_{IIb}\beta_3$) signaling (section 1.2.1). Advantages of peptides vs. entire proteins are manifold: proteins have to be isolated from different organisms eliciting undesirable immune responses, are subjected to proteolytic degradation and when used for surface coating they can adopt unnatural conformations/orientations (interactions with the surface either through the hydrophobic or the hydrophilic amino acids side chains).

2.3.3 Copolymerization of the PEG-DA chains with carboxyl moieties

In order to show the versatility of PEG-DA HGs as scaffolds for cell adhesion studies under mechanical strain where the geometry and localization of the ligands presented to the cells is not relevant, the surface of the HGs was homogeneously functionalized. Given the fact that PEG surfaces are protein repellent, physisorption (the commonly used protocol for surface coating) was not possible and covalent bond between the HGs and the protein of interest had to be established. Taking advantage of the reactivity of acrylate groups the surface of the HGs was functionalized with carboxyl moieties to which FN (section 1.2.1) was linked through the common amide bonding between carboxyl groups

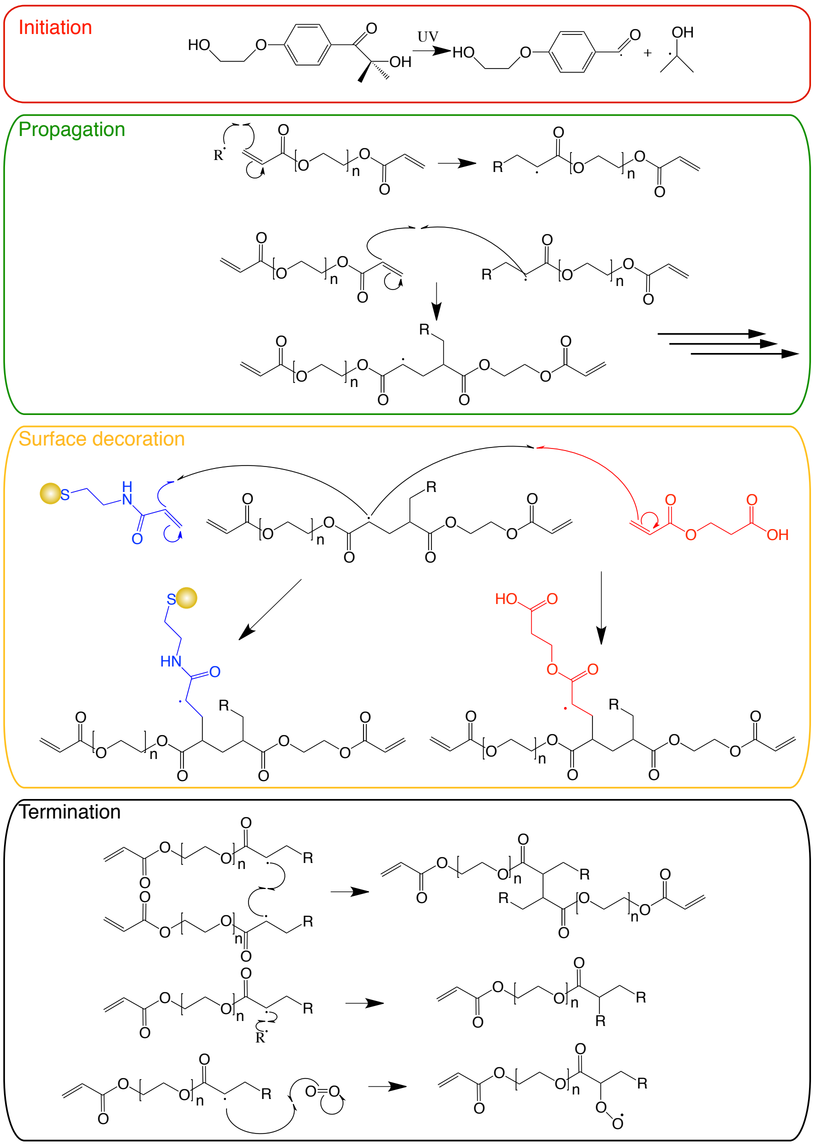

Figure 2.3: UV-photopolymerization chain reaction showing the characteristic phases of initiation, propagation and termination. Surface decoration represents the transfer of the AuNPS from the coverslip to the HG via the thiol linker (blue) or the incorporation of carboxylic groups via 2-(carboxyethyl)-acrylate (red) for posterior amide bonding.

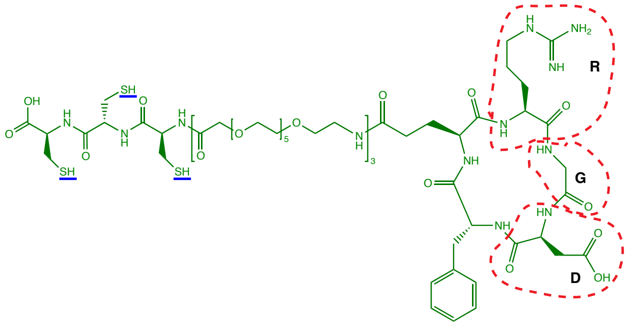

Figure 2.4: Detail of the RGD peptide mimetic used in this work to bio-functionalize the AuNPs. Underlined in blue are the thiol groups that bind to the AuNPs. In the red-dashed areas are the three amino-acids.

(2-(carboxyethyl)-acrylate) and primary amines (present in the amino terminus of FN).

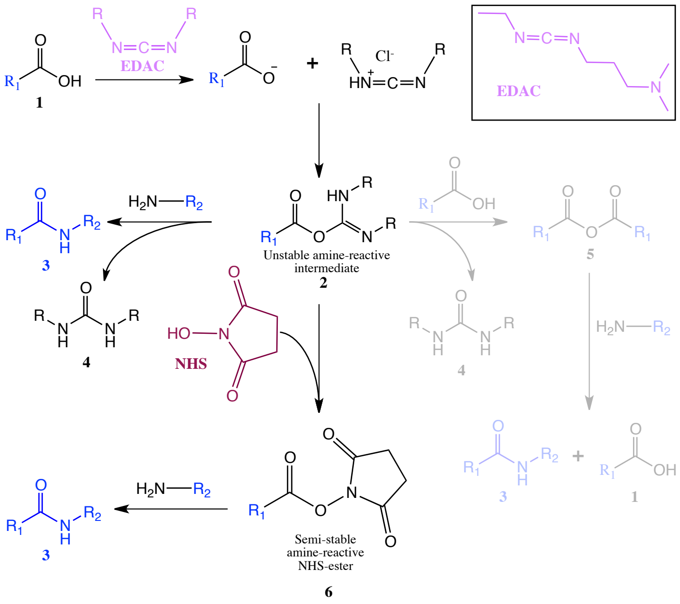

Figure 2.5: Peptide binding between carboxyl- and amino-groups. The compound EDAC (1-Ethyl-3-(3-dimethylaminopropyl)carbodiimide) is used as a carboxyl activating agent. The addition of N-Hydroxysuccinimide (NHS) increased the efficiency of EDAC-mediated coupling reactions [Grabarek and Gergely, 1990]. The faded segment in the figure represents a reduced probability of occurrence because reactant 2 will tend to react more favorably with $R_2 - NH_2$ than with the carboxylic acid (the former is more nucleophilic)

2.4 Mechanical traction of the functionalized HG

A thorough review of the available techniques for cell stimulation *in vitro* has been done elsewhere [Brown, 2000]. In short, the apparatuses presented include compressive loading systems, longitudinal stretch systems, systems utilizing substrate bending, out-of-plane circular and in-plane substrate distention and fluid shear systems. In terms of longitudinal stretch systems the main difference between the systems is how the motion is transmitted to the substrate [Langelier et al., 1999]. Flexible cables serving as motion transmitter have the disadvantage that can't apply compressive loads whereas rigid bars can act both pulling and pushing. Regarding the amplitude of the stretching, it has to be physiologically relevant [Brown, 2000], not so high that promotes cell apoptosis [Shefelbine et al., 2005], high enough so that cells can sense it [Hirschfeld-Warneken et al., 2008] and most importantly doable with the stretching method of choice.

2.5 Summary of the substrates fabrication

As a summary figure 2.6 shows the steps to be taken in order to fabricate the substrates. Their application to perform cell adhesions studies under mechanical strain is outlined.

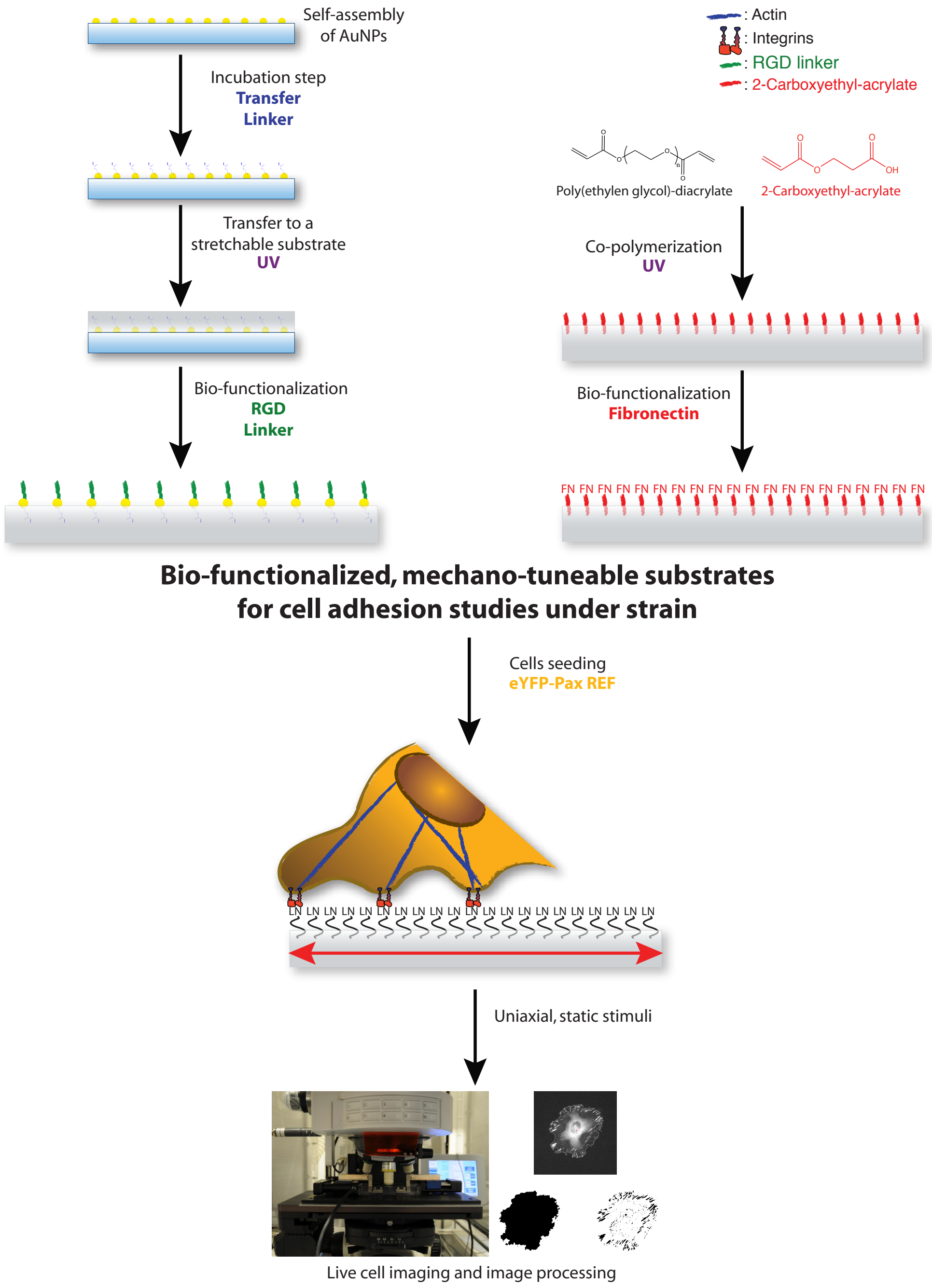

Figure 2.6: Fabrication of the substrates. HGs + AuNPs + RGD and HGs + FN used for cell adhesion studies under strain.

Part II

Materials and Methods

Chapter

3

Fabrication of the substrates

3.1 Polymeric, ECM-mimetic, elastic scaffolds

Modifying the end groups of the PEG chains to cross-linkable PEG-DA

First, PEG was dried via co-distillation with toluene: PEG-10000 (chains with a M_w of 10,000 g/mol from Fluka, Basel, Switzerland, 5 mmol) were placed in a brown flask, 250 mL toluene (p.a., Merck, Darmstadt, Germany) were added and waited until the solid was completely solved. Then the reaction mixture was connected to a rotary evaporator and was rotated at $40°C$ and 150 rpm until no toluene was left (final pressure 40 $mbar$). This whole process was repeated twice. Then the PEG chains were functionalized with acryloyl chloride: 125 mL dichloromethane (p.a., Merck, Darmstadt, Germany) and 75 mL toluene were added to the brown flask and under N_2 atmosphere triethlyamine (15 mmol) (SIGMA-ALDRICH Chemie GmbH, Taufkirchen, Germany) and acrylic acid chloride (15 mmol) (SIGMA-ALDRICH Chemie GmbH, Taufkirchen, Germany) were added. The reaction mixture was allowed to stir over night.

The mixture was filtered over a 2 cm plug of alumina* through a filter with mesh size 4 applying low vacuum. The aluminum oxide bed was rinsed twice with dichloromethane (40 to 50 mL each time) and was allowed to dry completely for the second time. 12.5 g of potassium carbonate (K_2CO_3) (SIGMA-ALDRICH Chemie GmbH, Taufkirchen, Germany) were added to the filtrated solution and stirred for 1.5 h protected from light. The potassium carbonate was filtered and washed with dichloromethane to ensure a complete recovery of the PEG-DA. Then the solution was transferred to a 500 mL brown flask and concentrated under vacuum in a a rotary evaporator at $25°C$ until no dichloromethane was left (final pressure 100 $mbar$). The product was then precipitated by addition of diethylether (500 mL, Merck, Darmstadt, Germany) and further stirred for 2 h. The slurry was filtrated in the frit by applying gentle vacuum. The remaining white solid was resuspended in 100 mL of diethylether and dried over the frit. Finally the product was transferred to a brown flask and connected to the oil pump for the final dry overnight. Usually 40 - 45 g of pure product were obtained (80 - 90 % yield).

---

*Mix of aluminum oxide and dichloromethane to a proportion that a thick creamy consistency is obtained.

The degree of modification of the PEG chains' OH-terminus with acrylate moieties is of great importance because it determines the cross-linking density of the cured HGs [Lin et al., 2005], factor from which depends to a great extent the integrity of the substrates and their elastic behavior. For this reason a ^{1}H-NMR analysis of the final product was performed (Dr. Roberto Fiammengo) (Figure A.1). As shown in figure A.1 and in equation A.1, 85 % of the end groups were successfully modified to acrylate.

3.2 Functionalization of the HGs' surface

3.2.1 Self-assembly of the nano-pattern by BCMN

As presented in the introduction by means of a diblock-copolymer self-assembly driven process glass surfaces can be patterned with a quasi-hexagonal array of AuNPs and varying ΔLs [Glass et al., 2003].

Cleaning the coverslips by piranha treatment

Prior to the nano-patterning the substrates have to be free from any organic residue. For that purpose they were immersed in freshly prepared Piranha solution (a mixture 3:1 of concentrated sulfuric acid (H_2SO_4, 98 %, JT Baker, Deventer, Holland) and hydrogen peroxide (H_2O_2, 30 %, Carlo Erba, Rodano, Italy)) with the help of a self-developed teflon holder. Usually the substrates were kept in the solution for one hour, time during which the solution cooled down. Afterwards they were extensively rinsed with deionized water and blown dry with N_2 right before the dip-coating took place.

Dip-coating

Micellar solutions used in this work consist of poly(styrene)-block-poly(2-vinylpiridine) (P(S-b-2VP)) diblock copolymers dissolved in toluene. Compositions and polydispersity indices (I_P M_w/M_n[†]) of the diblock-copolymes as well as the concentration and loading of the micellar solutions follow in table 3.1.

Table 3.1: Diblock-copolymers parameters and characteristics of the micellar solutions

PS(g/mol)-b-PVP(g/mol)	PS units	PVP units	I_P	C [mg/mL]	L	Name
PS(16,000)-b-PVP(3,500)	154	33	1.05	5	0.5	154er
PS(25,000)-b-PVP(15,000)	240	143	1.04	5	0.5	240er
PS(52,200)-b-PVP(34,000)	501	323	1.05	5	0.5	501er

In short, the designated amount of diblock-copolymer was weighed and stirred over night in toluene (*p.a.*, Merck, Darmstadt, Germany) protected from light. On the following day the core of the micelles were loaded with tetrachloroauric acid ($HAuCl_4$)

[†] Measure of the distribution of molecular mass in a given polymer sample [Iza et al., 1998]

(SIGMA-ALDRICH Chemie GmbH, Taufkirchen, Germany) in the glove box under Ar atmosphere (tetrachloroauric acid is extremely hygroscopic). The loading (L) was such that stochiometrically every second 2-VP unit formed a complex with $HAuCl_4$, i.e. a L of 0.5 $(P(S-b-2VP(HAuCl_4)_{0.5})$ and calculated through the equation 3.1. The solution was again allowed to stir over night protected from light.

$$L = \frac{n[HAuCl_4]VP}{mVP} \tag{3.1}$$

Dip-coating was performed as described in Glass et al. [2003] and shortly summarized in figure 3.1 at a retraction speed of 0.2 mm/s. After the substrates were dip-coated, the copolymer shell in the micelles was completely removed and the metal precursor reduced to metal by the exposure of the substrates to reactive oxygen ($0.4\,mbar\ O_2; 150\,W\ 15\,min$) and hydrogen ($0.4\,mbar\ H_2; 150\,W\ 15\,min$) microwave induced plasma (TePla 100-E, Germany). Every batch of dip-coated coverslips was checked under the SEM for the appearance of multi-dots, undesired leftovers of copolymers or wide areas not being covered with particles. If so, the batch was not used for further experimentation. ΔL and ordering parameter (ranges from 0 to 1 the proportion of particles having six neighbors) were obtained through an ImageJ plugin developed in the group (*Dot Analyzer*).

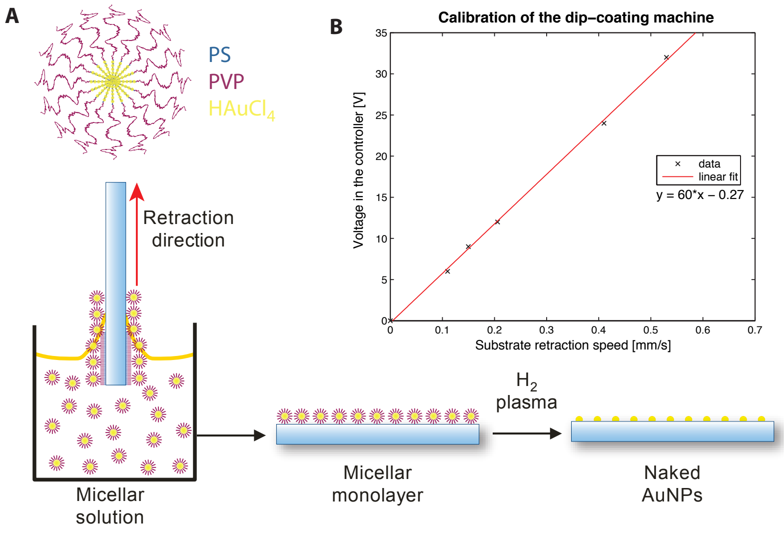

Figure 3.1: Dip-coating. **(A)** Schematic representation of the dip-coating process with a sketch of the micellar architecture. **(B)** Linear relation between controller voltage [V] and retraction speed [mm/s] of the dip-coating machine.

3.2.2 Transfer nano-lithography

AuNPs transfer occurs quite reliably and with reproducibility following the procedure described in Graeter et al. [2007]. A schematic representation of the steps necessary for the simultaneous transfer of the AuNPs from the glass coverslips to the PEG-DA chains and their cross-linking into polymerized HGs follows in figure 3.2.

Prior to the incubation in the transfer linker, dipped surfaces were plasma treated to ensure a clean gold surface: 15 min O_2 + 30 min H_2 ($0.4\,mbar$; 150 W). H_2 treatment serves the purpose of reducing back the Au_2O_3 to elemental Au so that the thiol group

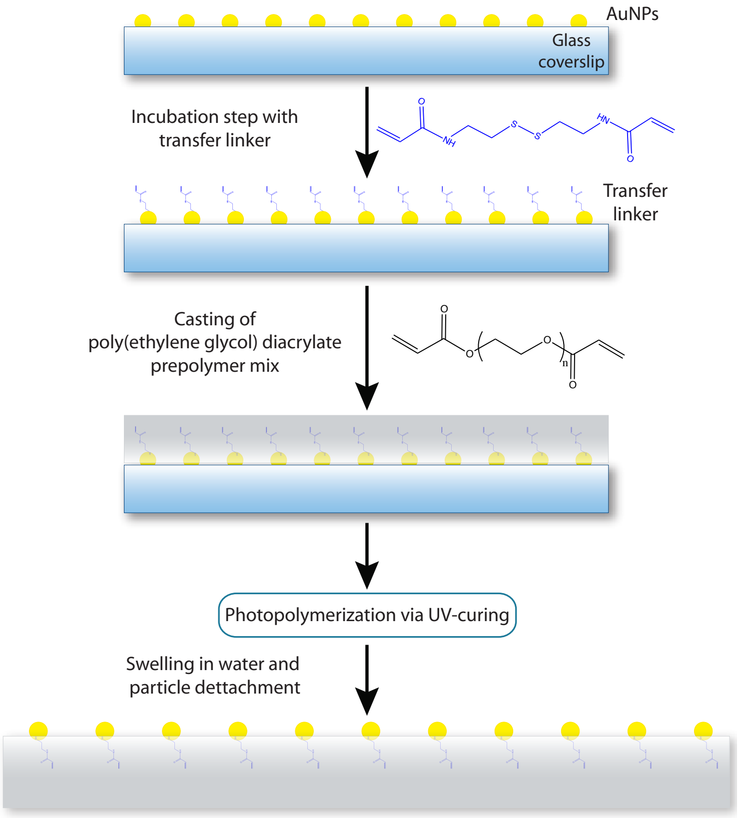

Figure 3.2: AuNPs are incubated in transfer linker (binds to the AuNPs via the thiol moiety). Prepolymer mixture of PEG-10K-DA is casted over the particles. Via UV-initiated photo-polymerization PEG chains and transfer linker (via their acrylate moiety) get cross-linked. In the swelling process the AuNPs bound to the transfer linker get detached from the glass and become the functionalization of the HGs.

in the transfer linker can bind. Directly after the plasma treatment the activated surfaces were incubated for 60 min in transfer linker solution protected from light. To prepare a 1mM transfer linker solution, 2.60 mg of N,N‘-Bis(acryloyl)cystamine (Mw: 260.38 g/mol, #14460 Fluka, Basel, Switzerland) were dissolved under N_2 atmosphere in 10 mL ethanol (EtOH) p.a. After the incubation surfaces were washed 3 times á 10 min in EtOH p.a. protected from light and dried under vacuum (desiccator). To prepare the saturated initiator solution, 15.2 mg of 2-Hydroxy-4’-(2-Hydroxyethoxy)-2-Methylpropiophenone[‡] (Mw: 224.25 g/mol, SIGMA-ALDRICH Chemie GmbH, Taufkirchen, Germany) were stirred ca 30 min at 40°C in a UV-save flask containing 2 mL degassed H_2O (in a warmed H_2O-bath under N_2 in a Schlenk Flask) and allowed to cool down before adding it to the prepolymer mix. To prepare the 40 % w/v prepolymer mixture, 400 mg of PEG-DA were added under N_2 to the designated amount of degassed H_2O and stirred until the solid was completely dissolved. 60 μL of the saturated initiator solution were added to the mix and further stirred. In order to avoid a partial inhibition of the chain reaction by O_2, the PEG-DA solution was degassed by alternating N_2-vacuum cycles. Vacuum should be applied only a few seconds to avoid excessive H_2O evaporation.

[‡] Advantages of this initiator are that it is not cytotoxic and allows the usage of water as solvent system [Bryant et al., 2000, Hageman, 1985]

3.2.3 Casting of the prepolymer in the customized mold and UV photo-polymerization

The prepolymer solution of PEG-10K-DA (40 % w/v) is a viscous liquid before polymerization.This enabled us to control easily the flowing of the mixture and hence the final form of the polymerized network by choosing the appropriate casting mold. Some thoughts had to be given to the design of the casting mold because it had to go hand-by-hand with the stretching method: The mold defined the final shape of the HGs and these in turn defined the needed clamping procedure, so the optimal combination between mold and pulling method had to be chosen. Figure 3.3 shows the decision tree for the optimal combination.

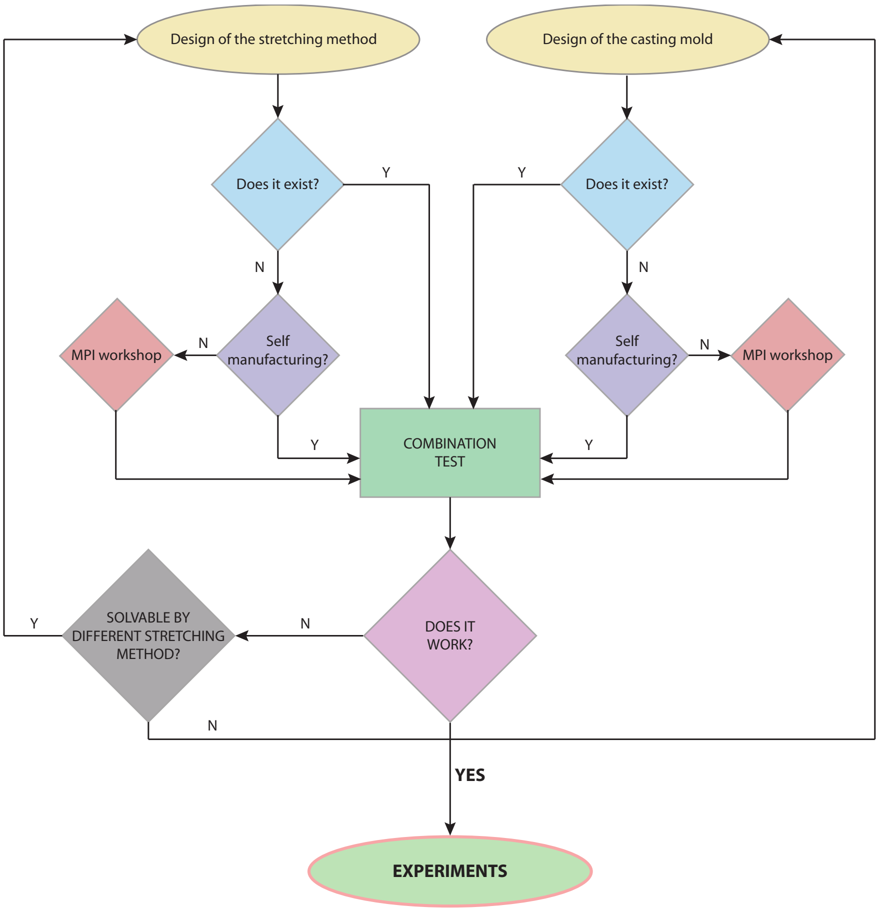

Figure 3.3: Decision tree followed to find the working combination between casting mold and stretching method (Y: Yes, N: No). First a mold was designed and manufactured. HGs were polymerized with the final form determined by the mold and the stretching method was designed. Combination was tested, if successful, experiments could be conducted, otherwise an alternative stretching method was designed. New combination was tested. If unsuccessful, a new mold had to be designed and the decision tree started again.

The casting itself was done with the equipment shown in figure 6.13. The casting mold was assembled into a partially closed construction with a quartz-glass slide laying on the platforms (black-dashed areas) and on the turrets (blue-dashed areas) and held by the black clamps from the sides. The white teflon sheets serve the purpose of limiting the progress of the prepolymer towards the sides and determining the final length of the polymerized HGs. This way the length of the HGs could be varied by using teflon pieces of different widths without needing newly manufactured casting molds. The stirring of the prepolymer mix in the brown UV-safe flask was stopped and under N_2 atmosphere a certain amount of liquid was extracted with a glass Pasteur pipette. The casting had to start at the upper-left part of the mold and the mold had to be tilted so that the complete left side got filled with liquid. Then the mold could be hold parallel again and the liquid allowed to flow through the central part and over the AuNPs. Final area to get filled was the right side. An homogeneous covering of the complete area is paramount for the robustness of the HGs and that was achieved by the adaptive tilting of the mold and the pressure regulation via the Pasteur pipette. The air outflows (yellow-dashed areas) facilitate this process immensely. For the strain characterization experiments, the HGs were copolymerized with polystyrene μ-beads (LB11-1ML, SIGMA-ALDRICH Chemie GmbH, Taufkirchen, Germany) 1.1 μm in diameter and at an approximate density of 100 μ-beads/mm^3. The prepolymer mix was cured during 5 minutes using a Hamamatsu Lightning cure LC8 lamp with an UV intensity output of 4,500 mW/cm^2. After the curing step, the now cross-linked HGs were immersed in deionized H_2O for at least 48 hours for three reasons: Washing out of the un-polymerized PEG-DA chains per diffusion; to guarantee that the HGs reach their H_2O uptake equilibrium; and to complete detachment of the AuNPs from the glass coverslips by means of the lateral forces generated by the isotropic swelling of the HGs in H_2O. In order to calculate the swelling ratio of the HGs, HGs were measured via slide gauge after each photo-polymerization process and their swelling was calculated by comparison with the dimensions of the casting mold.

Functionalization with the RGD motif

Substrates were incubated with 40 μL of a 25 μM solution of the ligand (Figure 2.4) covered with a fitting piece of Parafilm to ensure a homogeneous distribution of the solution for 45 minutes. Afterwards the linker that was non-covalently bound to the AuNPs was washed away by extensively rinsing with deionized H_2O. Following, the HGs were sterilized for 30 minutes in 70 % EtOH under the flow bench, rinsed 3x with sterile deionized H_2O and left further over night in H_2O in sterile conditions to guarantee a complete removal of the noxious EtOH. Prior to cell seeding, they were at least 2 hours soaking in cell medium in order to avoid the harmful effect of the low ionic strength of deionized H_2O in the living cells. On the following, HGs patterned with AuNPs and functionalized with the RGD motif are named as: HGs + AuNPs + RGD.

3.2.4 Copolymerization of the PEG-DA chains with carboxyl moieties

Through this procedure (Figure 2.5) a peptide binding between carboxyl- and amino-groups is established. The compound EDAC (1-Ethyl-3-(3-dimethylaminopropyl) carbodiimide) is used as a carboxyl activating agent, as it reacts with carboxyls to form an intermediate that gets stabilized by reacting with amines thereby forming a peptidic bond without spacer length. However, the intermediate is also susceptible to hydrolysis, making it unstable and short-lived in aqueous solution. The addition of N-Hydroxysuccinimide (NHS) stabilizes the amine-reactive intermediate by converting it to an amine-reactive NHS-ester, thus increasing the efficiency of EDAC-mediated coupling reactions [Grabarek and Gergely, 1990]. The process was performed on ice, for that the samples to be functionalized were placed on a metallic platform on ice so that they could start cooling down. 78 mg of EDAC and 19.5 mg of NHS were dissolved in 1 mL of Milli-Q H_2O only minutes before the functionalization process. 100 μL of the mix for each sample was placed in a Petri-dish and the samples were placed on them with the surfaces to be functionalized facing downwards and incubated for 1 hour. In the meantime two phosphate buffered saline (PBS) solutions were prepared with different final concentrations: 25 and 50 mM. The 25 mM PBS solution was used to prepare the Fibronectin solution (100 $\mu g/mL$) and the samples were incubated for 50 minutes following the same procedure as before. The 50 mM PBS solution was then used to wash the samples 3 times á 10 minutes. On the following, HGs homogeneously coated with FN are named as: HGs + FN.

3.3 Surface characterization

3.3.1 Scanning Electron Microscope and cryo SEM

Since the optical resolution of light microscopy can't resolve the AuNPs a Zeiss Ultra 55 e^--microscope and its InLens detector at an acceleration voltage of 5k̇V was used to scan the AuNPs on the glass substrates. Non-conductive glass coverslips were sputter-coated with a 5 nm thick graphite layer prior to SEM investigations. The geometrical order and inter-particle spacing were then analyzed using ImageJ's plugin "Gold dot Analyzer" developed in the group.

HGs as they are can't be subjected to the ultra-high vacuum conditions needed for the SEM investigations. There can't be any H_2O in liquid phase during the imaging and for that the samples were frozen in liquid N_2 and the formed ice was subsequently sublimated (BAL-TECH MED 020 sublimation machine). A BAL-TECH VLC 100 shuttle and loading system were used to transfer the PEG-DA HGs into the cryo-SEM chamber.

3.3.2 Scanning Probe Microscope

Atomic Force Microscopy was performed with a Nano Wizard II SPM (JPK Instruments AG, Berlin, Germany) mounted on a Leica microscope enabling simultaneous phase contrast, fluorescent and SPM microscopy. Veeco NanoProbe NP-S cantilevers (Veeco, Camarillo, USA) were used for image acquisition. Spring constants were determined by the thermal noise calibration method embedded in the JPK desktop software and were always in the range of 1 N/m which is good for Intermittent Contact Mode operation in liquid where capillary forces between tip and sample are minimized.

Chapter

4

Experimental Design

Design of the experiments conducted for cell adhesion studies under strain.

4.1 Cell system

In this section a short description of the cell system used as well as of the cell culture and seeding prior to the stretching experiments is given.

4.1.1 Maintenance of cells in culture

For all experiments a fibroblast system was used for a number of reasons: fibroblasts have been extensively shown to be sensitive to forces most probably because they themselves are *in vivo* subjected to constant stimuli; fibroblasts are quite robust cells and hence appropriate for this work where stress of different kinds (restricted ligand density, restricted medium supplementation, fluorescent light, strain,...) was imposed upon the cells; rat embryonic fibroblasts (REF) cells stably expressing paxillin fused with yellow fluorescent protein (YFP) were kindly provided by Benny Geiger from the Weizmann Institute of Science (Rehovot, Israel). Since no further transfection with fluorescent proteins was needed, this cellular system was very attractive for live cell imaging. The REF cells were maintained in DMEM GlutaMAX (#31966-021, Gibco, Invitrogen GmbH, Darmstadt, Germany) cell medium supplemented with 10 % fetal bovine serum (FBS) at $37°C$ and 5 % CO_2. After the cells reached 80–90 % confluence, they were first rinsed with sterile PBS and then released from the underlying support by incubating them with a trypsin-EDTA 0.25 % solution (Gibco, Invitrogen GmbH, Darmstadt, Germany) for 3–5 minutes. Trypsin effect was stopped by using DMEM Glutamax supplemented with 10 % FBS. The resulting cell suspension was centrifuged and the supernatant discarded. Cells were resuspended in fresh medium and plated in a new cell culture flasks at a 1:10 dilution.

4.1.2 Cell seeding

For adhesion studies, cells were trypsinized in 0.25 % trypsin-EDTA and plated on the biofunctionalized PEG-DA HGs equilibrated in DMEM containing 10 % FBS. Cell seeding was done at a density of $200\,cells/mm^2$, for what a Neubauer counting cell chamber was used. Cells were allowed to attach and spread over night and experiments were conducted the following day. A fluorescent image of the cells can be seen in Figure 4.1.

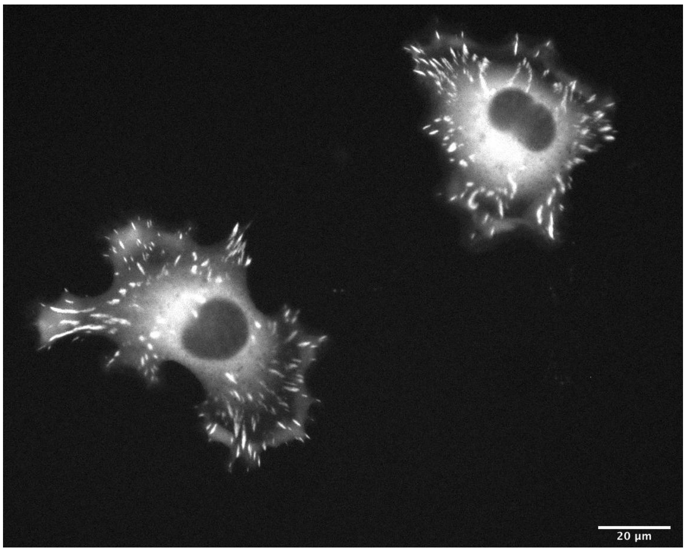

Figure 4.1: Rat Embryonic Fibroblasts eYFP-Pax stably transfected.

One hour prior to the experiment the cell medium was changed for sterile-filtered L-15 Leibovitz (#L1518 SIGMA-ALDRICH Chemie GmbH, Taufkirchen, Germany) supplemented with 3 % FBS and 1 % Penicillin/Streptomycin to eliminate the noxious effect of Phenol Red[*] and to be able to work in CO_2 free conditions[†]. The usual 10 % FBS supplementation of cell medium was reduced to further avoid interference during the live cell imaging due to autofluorescence.

4.2 Uniaxial, static stretching

4.2.1 Important elements of the stimuli unit

The stimuli apparatus used was self-developed and consisted of a perforated support plate (allowing transmitted light microscopy techniques to be performed on the setup) on which two lineal motors from Physik Instrumente (Physik Instrumente (PI) GmbH & Co.KG, Karslruhe, Germany) were mounted at a fixed position. Furthermore, to these motors were attached self-designed metallic clamps that transmitted the stimuli to the PEG-DA HGs. Figure 4.2 shows the actual apparatus with the important elements listed:

(A) Linear motors employed to stretch uniaxially from both sides of the PEG-10k-DA HGs simultaneously.

---

[*] pH indicator routinely used in common cell culture mediums to check for contaminations in cell culture flasks

[†] L-15 is buffered by a complement of salts, free base amino acids and galactose substituted for glucose to help maintain physiological pH control

(B) Metallic clamps used to pull from the HGs. An important feature of the horizontal platform where the HGs lay are the cylinders placed so that their position correlates exactly with the position of the holes in the HGs.

(C) Reservoir (made of glass to allow DIC microscopy) to keep the HGs constantly in cell medium.

(D) Mounting plate to serve as underlying support for all different elements.

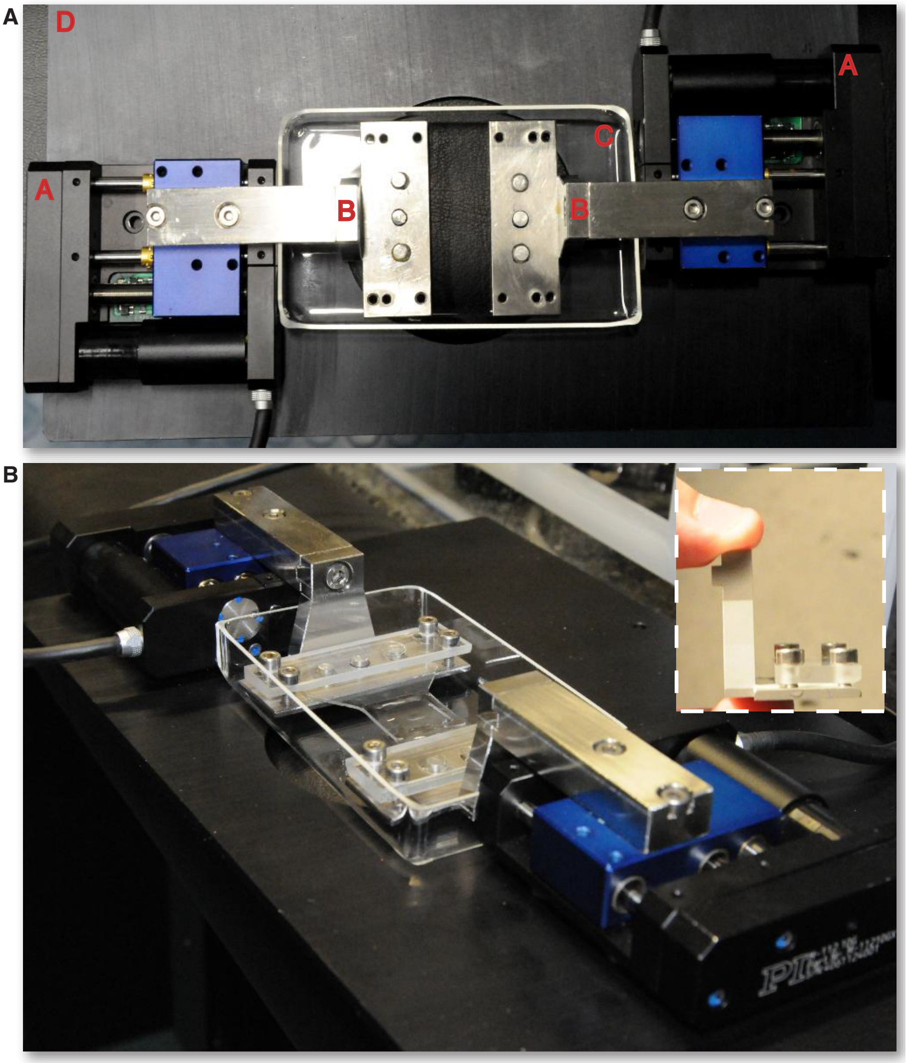

Figure 4.2: Stimuli unit. **(A)** top view of the self developed stimuli unit used in the thesis. (A) Physik Instruments stepper motors. (B) Clamps. (C) Glass reservoir. (D) Support plate. **(B)** Lateral view of the stimuli unit with a HG mounted. White dashed area shows an insert with a close-up on the metallic clamps with rounded edges and a glass upper part.

In the lower part of the figure a lateral view of the same setup is presented were also the spanned PEG-DA HG with its characteristic dog-bone shape can be seen. Additionally, as small insert, a close view of the clamps is presented. Two details worth noting are: The edges of both upper and lower parts of the clamp are rounded to avoid any sharpness that could damage the HGs; the upper part is made out of glass in order to visually monitor the homogeneous deformation exerted on the HGs upon stretching. The apparatus was then attached to the stage of a Zeiss Axio Examiner.Z1 microscope (Carl Zeiss AG, Oberkochen, Germany) in a heated chamber with a temperature close to physiological conditions (37°C). The microscope itself was mounted on a pneumatic isolation table (CVI Melles griot, Albuquerque, USA) in order to avoid disturbances during the live cell imaging.

4.2.2 Stretching procedure

Most important aspects of the procedure was to ensure the maintenance of sterile conditions and the integrity of the HGs along their manipulation, transport and mounting on the clamps of the stimuli unit in the microscope. For that the microscope and all single elements of the apparatus were thoroughly wiped with EtOH (70 %) and dried with fuzz-free paper. Then the HGs (already equilibrated in L-15 medium) were transported in their sterile Petri-dish to the microscope and immediately introduced in the heated chamber in order to avoid unnecessary stress for the cells. Subsequently, with help of a teflon tweezer (without sharp edges) the HG was transferred to its final location making coincide holes and cylinders. The upper glass parts of the clamps were screwed to the bottom parts guaranteeing that no slipping away of the HGs would occur in the middle of the experiment. The reservoir was then filled with 50 mL L-15 medium (Sigma-Aldrich) supplemented with 3 % FBS and 1 % Penicillin/Streptomycin and the HG was pre-spanned so no curvature would pre-condition the behavior of the cells. After 30 minutes the experiment started. Amplitude of the stretching was 15 % applied in two 7.5 % consecutive steps.

4.3 Live-cell imaging: Optical microscopy

4.3.1 Differential Interference Contrast microscopy (DIC)

DIC (also known as Normarski Interference Contrast (NIC) [Allen et al., 1969, Pluta, 1846]) was used for the autofocus routine so that photobleaching[‡] was minimized. In order to have the best possible illumination conditions the light path was adjusted according to Köhler and Normarski principles. The set-up was mounted on a motorized upright Zeiss Axio Examiner.Z1 microscope (Carl Zeiss AG, Oberkochen, Germany) equipped with a 40x immersion objective. Images were acquired with an AxioCam MRm CCD camera (Carl Zeiss AG, Oberkochen, Germany) and saved in Zeiss customary format (.zvi). Since it is usually impossible to image large 3-D objects entirely in focus, cells were optically sectioned through a Z-Stack acquisition consisting of 5 planes, 0.3 μM separated from each other to guarantee that the focal plane of interest was included. Time-lapse between the images is described in section 4.4.

[‡] Photochemical destruction of a fluorophore by the incident fluorescent light

4.3.2 Fluorescence microscopy

Photomicrographs were acquired on a Zeiss Axio Examiner.Z1 microscope (Carl Zeiss AG, Oberkochen, Germany), with a 40x immersion objective, a YFP filter set (46, Zeiss AG) and an AxioCam MRm CCD camera (Carl Zeiss AG, Oberkochen, Germany) and saved in Zeiss customary format (.zvi). Cells were optically sectioned through a Z-Stack acquisition consisting of 5 planes, $0.3\,\mu$M separated from each other to guarantee that the focal plane of interest was included. Time-lapse between the images is described in section 4.4[§].

4.3.3 Integration of complementary software: A custom-written Visual Basic for Applications (VBA) program

Figure A.3 presents the interface of the VBA program (Marc Gronle). The program allows the simultaneous control of Zeiss Axiovision and Physik Instrumente softwares enabling us to synchronize the actions of the microscope and the motors actuating on the PEG-DA HGs. As a result, we could design at our ease the single steps along our experiments in a drag-and-drop way.

4.4 Experiment description

Images were taken at 5 different positions on each HG from the central area (homogeneous strain field) by DIC and fluorescence microscopy. As depicted in figure 4.3 for every position observed, three differentiated phases were set, established in relation to the stretching step and serving to complementary purposes.

1. **Before the stretching step:** To identify the cells on the central area of the substrate that will be monitored. It consists of 1 image from the 5 positions which are not further processed.

2. **During the stretching step (Stretch):** Due to the stretching the Z-position of the cells varies and the focus plane has to be redefined. It consists of 2 images from the 5 positions with a lapse of 1 minute among them.

3. **After the stretching step (Stretched observation):** Monitoring of the cells after the stimuli has been applied to them. It consists of three sub-phases with different time-lapses among the pictures.
    - Phase *I*: 10 images from the 5 positions with a lapse of 1 minute among them.
    - Phase *II*: 10 images from the 5 positions with a lapse of 2 minutes among them.
    - Phase *III*: 5 images from the 5 positions with a lapse of 5 minutes among them to complete a total of 45 minutes of observation.

[§] Basics of light microscopy can be found in Murphy [2001]

Figure 4.3 shows the evolution in time of the potential readouts from the observation of one single cell. Colored lines represents the potential temporal change of a readout in response to the transmitted strain. Green would correspond to a readout showing an increasing change sustained during the observation. Red would correspond to a readout showing a transient increasing change returning to initial conditions after the stimuli. Purple would correspond to a readout showing no effect to the stimuli. Blue would correspond to a readout showing a decreasing change sustained during the observation.

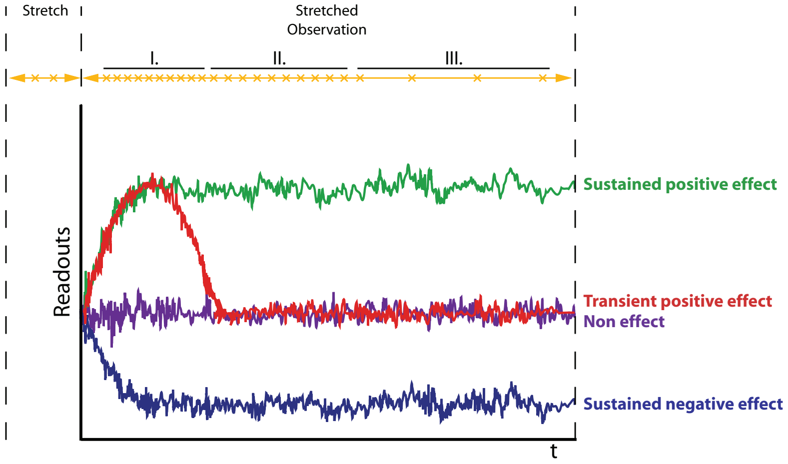

Figure 4.3: Experiment design. Schema showing the time-lapse experimental design and the potential manifold readouts of a cell's response. I. represents phase I of the stretched observation. II. represents phase II of the stretched observation. III. represents phase III of the stretched observation. Colored lines represents the potential temporal change of a readout in response to the transmitted strain.

Chapter

5

Image processing and analysis

In this chapter the description of the image processing and the data analysis is given. ImageJ (http://rsbweb.nih.gov/ij/) was used for the image processing and MatLab (The MathWorks, Inc., Natick, Massachusetts) was used for the data analysis.

5.1 Requirements of the data analysis

A number of reasons accounts for the complexity of the image analysis conducted during this work:

1. The biological application of this work laid in the study of cell adhesion with dynamic variation of inter-ligand distances. How a cell adheres to its underlying substrate is a complex process which depends upon many parameters and will have a variable nature. An important aspect of this variability will be the number of FAs (number of particles to be analyzed) for a specific time-point which can be different for the cells analyzed. Therefore, the analysis conducted had to be dynamic and adapt to a changing number of particles.

2. Part of the analysis relied in delimiting accurately the silhouette of the cell and of the FAs in order to obtain a series of readouts. For this purpose image processing routines had to be developed.

3. A cell subjected to uniaxial static strain will experience an extension parallel to the stretching direction and a compression perpendicular to the stretching direction. For that reason treating all FAs as an homogeneous population could lead to biased conclusions since it could happen that two sub-populations existed displaying contradictory reactions and that in the averaging they would cancel reciprocally. That's why the possibility of a spatial segmentation of the cells was a feature the analysis had to have.

5.2 Image processing with ImageJ

5.2.1 Processing of the images acquired with the AxioCam MRm CCD camera

ImageJ is a freeware, crow-sourced, Java-based bundle of image processing features that can be further developed with self-written macros. Furthermore new plugins (features) are constantly being written around the world and put at community disposal. Images acquired with the AxioCam MRm CCD camera are a Z-stack of different focal planes and are saved in the Zeiss AxioVision (.zvi, Zeiss Vision Image) format. Unfortunately, ZVI is not a common format that can be imported and edited with the standard image processing programs. One such plugin developed for ImageJ can import ZVI formats: Bio-Formats Importer, a standalone Java library for reading and writing life sciences image formats (LOCI biophotonics research laboratory at the University of Wisconsin-Madison http://www.loci.wisc.edu/software/bio-formats). Furthermore, another plugin (complex wavelet-based method [Forster et al., 2004]) can merge all focal planes contained in the Z-stack into one single plane: Extended Depth of Field (École Polytechnique Fédérale de Lausanne http://bigwww.epfl.ch/demo/edf/). For the processing of the images a self-written macro was used. It consisted of a closed loop so all files in the same folder could be processed sequentially (throughput), the two aforementioned plugins, a segment for conversion to .tiff format and a final segment for saving and closing. With this macro the images were processed reliably and in a semi-automated way. At the end of the loop a stack of single-plane images in .tiff format was obtained that was subsequently analyzed with additional self-written routines.

5.2.2 Custom self-written routines for image analysis

iMacro = *iCell* + *iFAs* + *iCalc*

iMacro was the main ImageJ image processing macro composed of *iCell*, *iFAs* and *iCalc*. Each of these smaller segments had an image processing part (consisting of a combination of sequential processing steps) and an image analysis part (quantifying parameters of relevance). Figure 5.1, shows the image processing parts of *iCell* and *iFAs*. These sequential image processing step were sequentially applied to all the images of each film.

By applying the image processing parts of *iCell* and *iFAs* to the .tiff files it could be obtained from the same initial image the silhouette of the cell as a black body and the FAs as black particles, respectively. By applying the image analysis part of *iCell* to the black body of the cell the total area, shape descriptors (aspect ratio, circularity or formfactor and roundness), its angle to the stretch axis and the center of mass (CofM) could be obtained. By applying the image analysis part of *iFAs* to the black particles their area, elongation, angle to the stretch axis, number and spatial coordinates could be obtained.

Shape descriptors as they appear in ImageJ:

- Circularity: With a value of 1.0 indicating a perfect circle. As the value approaches

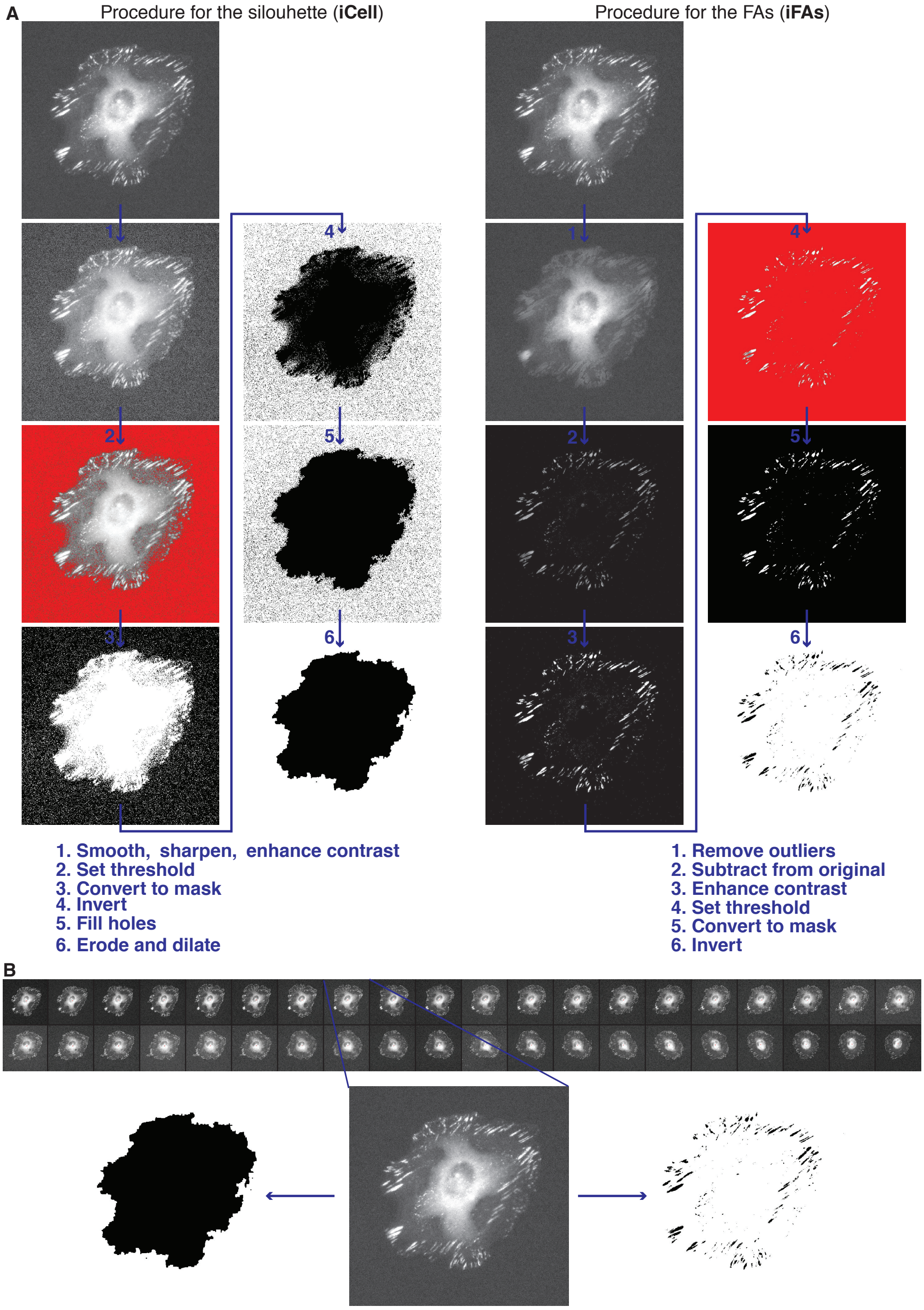

Figure 5.1: Visual description of the image processing performed with the ImageJ *iMacro* macro. **(A)** Combination of sequential image processing steps. *iCell* at the left hand side yielding the cells' silhouette and *iFAs* at the right hand side yielding the FAs as black particles. **(B)** These steps were executed for the total length of the stack.

0.0, it indicates an increasingly elongated shape.

$$\text{Circularity (Circ)} = \frac{4 \times \pi \text{ Area}}{\text{Perimeter}^2} \tag{5.1}$$

- The aspect ratio of the particle's fitted ellipse.

$$\text{Aspect Ratio (AR)} = \frac{\text{Major Axis}}{\text{Minor Axis}} \tag{5.2}$$

- Roundness can be interpreted as the inverse of Aspect Ratio.

$$\text{Roundness (Round)} = \frac{4 \times \text{ Area}}{\pi \times \text{ Major Axis}^2} \tag{5.3}$$

Finally *iCalc* segment compares for every time-point the cell's silhouette relative to the previous one (XOR logical operation implemented in ImageJ shown in figure 5.2) giving an idea on cell's shape variation in time.

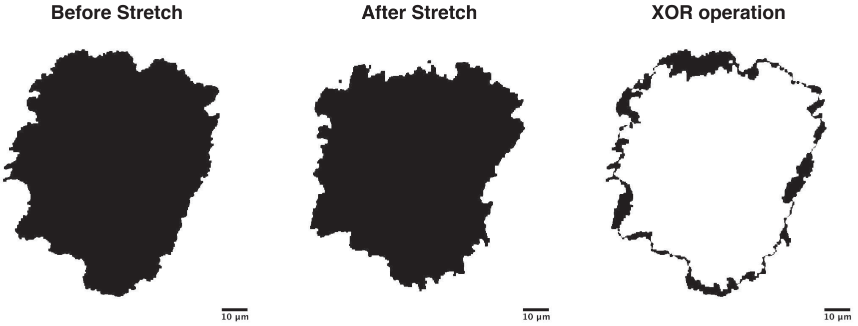

Figure 5.2: Visual description of the ImageJ *iCalc* macro. Using the XOR calculation between images embedded in ImageJ we can quantify protrusion activity.

Additionally, an ellipse is fit to the particle being analyzed and major and minor axis of the best fitting ellipse are measured. Angle is the angle between the major axis and a line parallel to the X-axis of the image which will be useful afterwards to determine whether the cell was predominantly parallel to the stretch direction or predominantly perpendicular (see figure 5.3).

iPixel

In order to quantify the strain applied to the substrates and verify that the cells were indeed subjected to the stimuli, a macro was designed that scans the picture from the left to the right side and then from up to down reading at each line how many black pixels the cell is composed of. In the process the width and the height of the cell are measured (Figure 5.4). Expected is that on the central part the width of the cell increases (red line over the gray line in the parallel scan direction) whereas the height decreases (red line

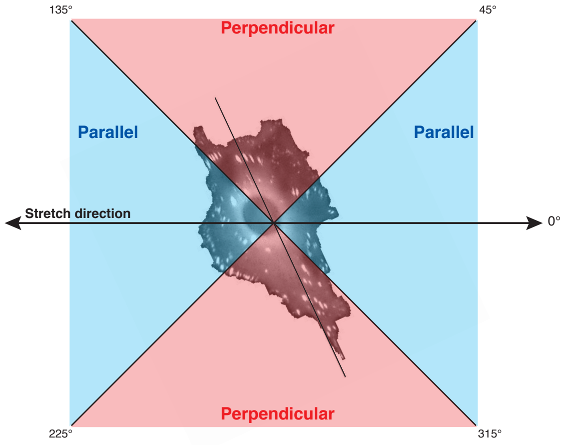

Figure 5.3: Determination of cells angle to the stretch direction. Cells with their major axis falling in the blue area were considered as mainly parallel to the stretch direction. Cells with their major axis falling in the redish area were considered as mainly perpendicular to the stretch direction.

below the gray line in the perpendicular scan direction). Its more useful output was to quantitatively measure how much strain was being applied on the cell on the central part (region of interest was defined as a 30 % taking as origin the CofM of the cell's width and height for the tensile strain and for the compressive strain, respectively).

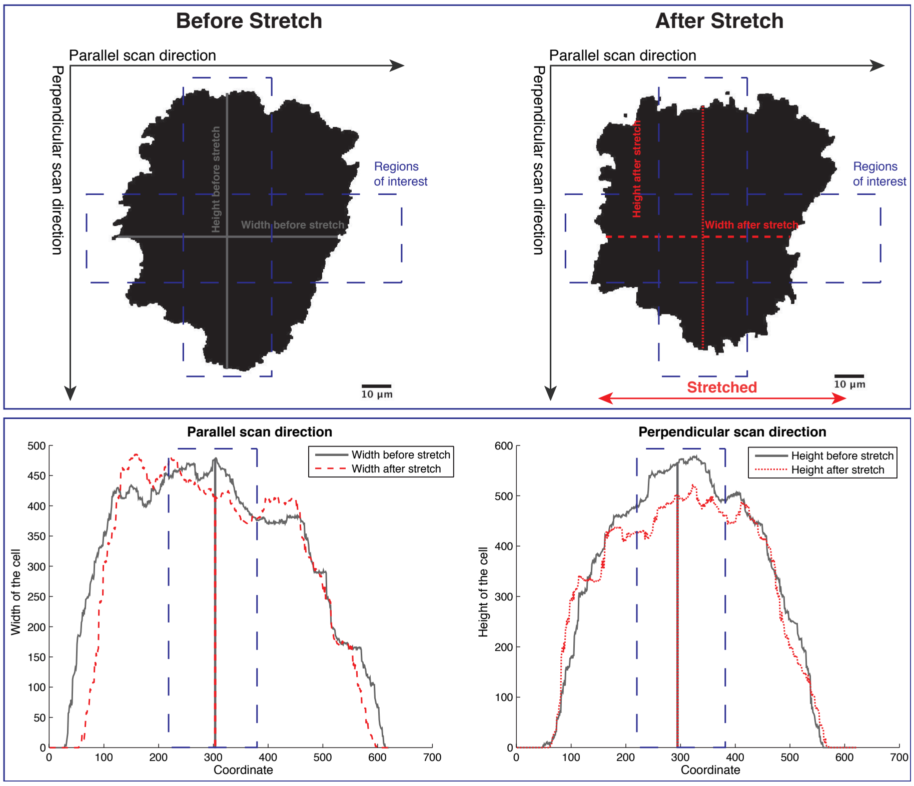

Figure 5.4: Visual description of the ImageJ *iPixel* macro. Pairwise comparison of each gray line with its coordinate-correlated red-dashed line allows to quantify extension (parallel to stretch axis scanning direction) and compression (perpendicular to stretch axis scanning direction) of the cell along its width and height.

Two components of strain were defined and shown in equations 5.4 and 5.5.

$$\text{Tensile strain} = \frac{\text{Width after stretching - Width before stretching}}{\text{Width before stretching}} \times 100 \tag{5.4}$$

$$\text{Compressive strain} = \frac{\text{Height after stretching - Height before stretching}}{\text{Height before stretching}} \times 100 \tag{5.5}$$

As final summary of the ImageJ image processing, table 5.1 presents the text files produced by *iMacro* and the information each of them contains is presented.

Table 5.1: Output of the ImageJ *iMacro* macro.

Name	*iCell.txt*	*iFAs.txt*	*iCalc.txt*	*iPixel.txt*
Information	Area of the cell	Area	Membrane activity	Cell width
	Shape descriptors	Elongation		Cell height
	Time	Number of FAs		
	Angle	Angle		
	Coordinates	Coordinates		

5.3 Data analysis with MatLab

As platform for the subsequent data analysis MatLab was chosen because it allows to process big, heterogeneous (containing both numeric and text data) data-sets fast and because it has a built-in development environment where custom self-written routines can be coded. The self-written MatLab *iMacro* macro had also smaller code segments that obtained the information of the text files generated with ImageJ: *iCell.txt*, *iFAs.txt*, *iCalc.txt* and *iPixel.txt*.

5.3.1 Extracting the information from the text files of each position for the different conditions

Figure 5.5 (A) represents how for the three different conditions the information corresponding to each cell (position) was obtained from the text files.

5.3.2 Data segmentation

Figure 5.5 (B) represents how the information imported from the text files can be used to perform segmented analysis.

Orientation of the cell: Based in the major axis of the best fitted ellipse to the cell and relative to the stretching axis, the orientation of the cell can be defined as predominantly parallel (blue area) or perpendicular (red area) to the stretch direction.

Size of the FAs: Depending on the size of the FAs, they are defined as small ($< 1\,\mu\text{m}^2$) or large ($> 1\,\mu\text{m}^2$) particles.

Position of the FAs in the cell: The coordinates of the CofM of a cell at each time-point as well as the coordinates of the FAs are known. By setting the cell's CofM as the new origin of the particles, their relative position in the cell can be found and a 4-fold segmented analysis can be performed (based in the center of mass of the cell and angles: 45°, 135°, 225° and 315°). In a single-cell analysis, with a sub-division into four segments and considering four parameters the amount of plots and hence the complexity of the analysis is worth to mention.

5.3.3 Statistics and plotting

Figure 5.5 (C) represents how the values of the parameters of interest are averaged for each condition, normalized to their respective initial values, plotted and saved

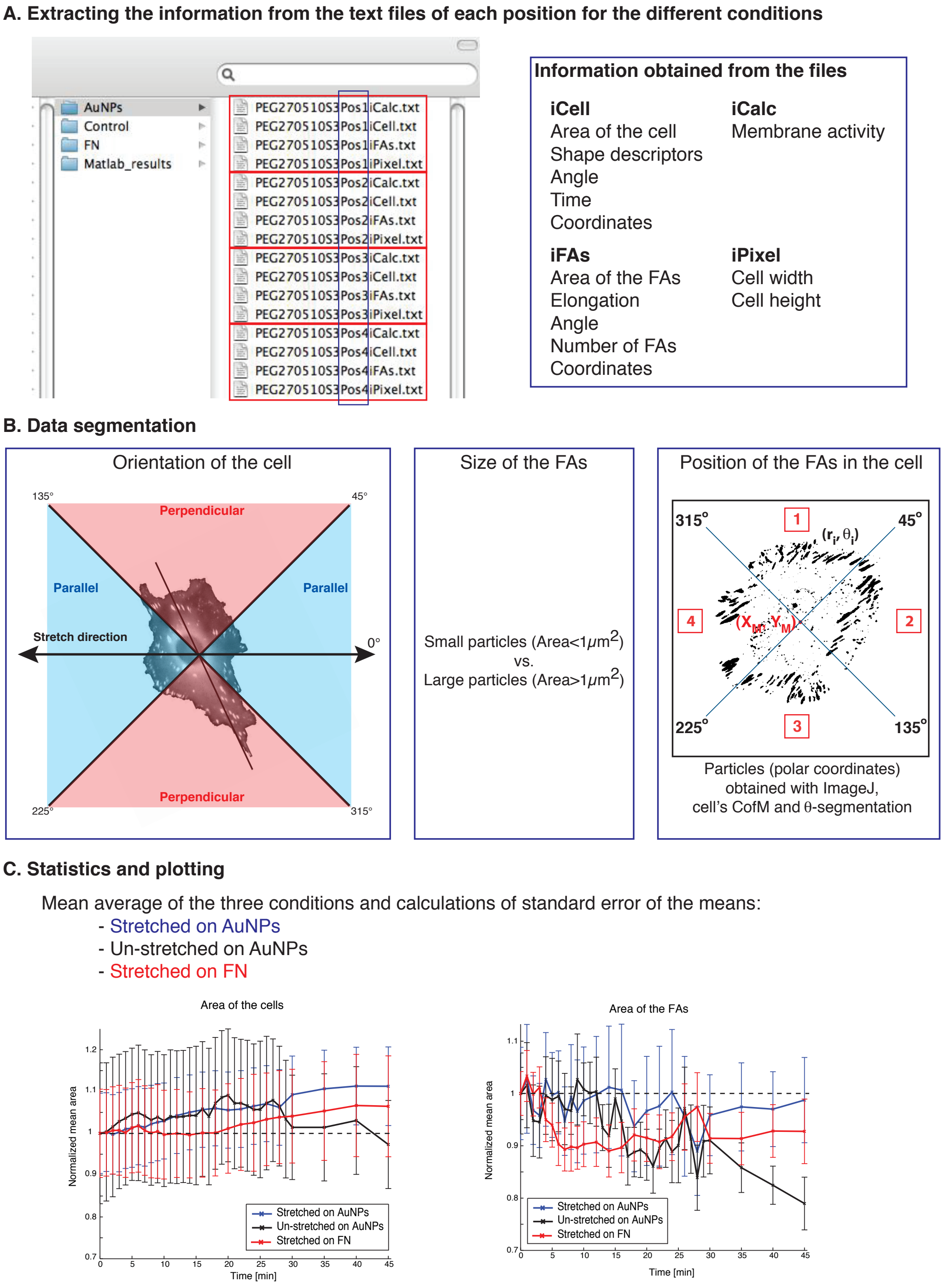

A. Extracting the information from the text files of each position for the different conditions

PEG270510S3Pos1iCalc.txt
PEG270510S3Pos1iCell.txt
PEG270510S3Pos1iFAs.txt
PEG270510S3Pos1iPixel.txt
PEG270510S3Pos2iCalc.txt
PEG270510S3Pos2iCell.txt
PEG270510S3Pos2iFAs.txt
PEG270510S3Pos2iPixel.txt
PEG270510S3Pos3iCalc.txt
PEG270510S3Pos3iCell.txt
PEG270510S3Pos3iFAs.txt
PEG270510S3Pos3iPixel.txt
PEG270510S3Pos4iCalc.txt
PEG270510S3Pos4iCell.txt
PEG270510S3Pos4iFAs.txt
PEG270510S3Pos4iPixel.txt

Information obtained from the files

iCell
Area of the cell
Shape descriptors
Angle
Time
Coordinates

iCalc
Membrane activity

iFAs
Area of the FAs
Elongation
Angle
Number of FAs
Coordinates

iPixel
Cell width
Cell height

B. Data segmentation

Orientation of the cell

Size of the FAs

Small particles (Area<1μm^2)
vs.
Large particles (Area>1μm^2)

Position of the FAs in the cell

Particles (polar coordinates)
obtained with ImageJ,
cell's CofM and θ-segmentation

C. Statistics and plotting

Mean average of the three conditions and calculations of standard error of the means:
- Stretched on AuNPs
- Un-stretched on AuNPs
- Stretched on FN

Figure 5.5: Visual description of the MatLab *iMacro* macro. **(A)** Folder containing the text files and the information obtained from each file. **(B)** Data segmentation possibilities: Orientation of the cell, size of the FAs and position of the FAs in the cell. **(C)** Average of the parameters of interest, plotting and saving.

Part III

Results and Discussion

Chapter

6

Characterization of the ECM-mimetic, elastic PEG-DA HGs

This chapter describes the fabrication of the quasi-hexagonal arrays of AuNPs on glass coverslips, their reliable transfer to ECM-mimetic, elastic scaffolds and their posterior monitored stretching.

6.1 Self-assembly of the nano-pattern by BCMN

Figure 6.1 shows a 50000x magnified SEM image of AuNPs deposited on a glass coverslip.

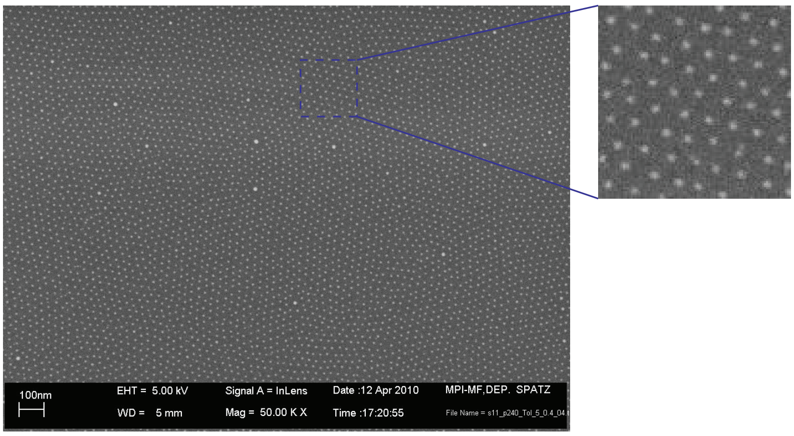

Figure 6.1: 50000x magnified SEM image of AuNPs deposited on a glass coverslip by the BCMN technique. A zoom in the blue dashed area is shown.

The ΔLs between the AuNPs and the ordering parameter of the array will determine the position of the ligands presented to the cells and are therefore crucial in this work. Both parameters were obtained via the aforementioned ImageJ plugin Dot Analyzer (section 3.2.1) and are shown in figure 6.2 together with their dependance of the type of diblock-copolymer and the retraction speed.

The ΔLs increase with an increasing length of the used diblock-copolymers (micelles formed in solution are correspondingly larger) and decrease with a decreasing retraction

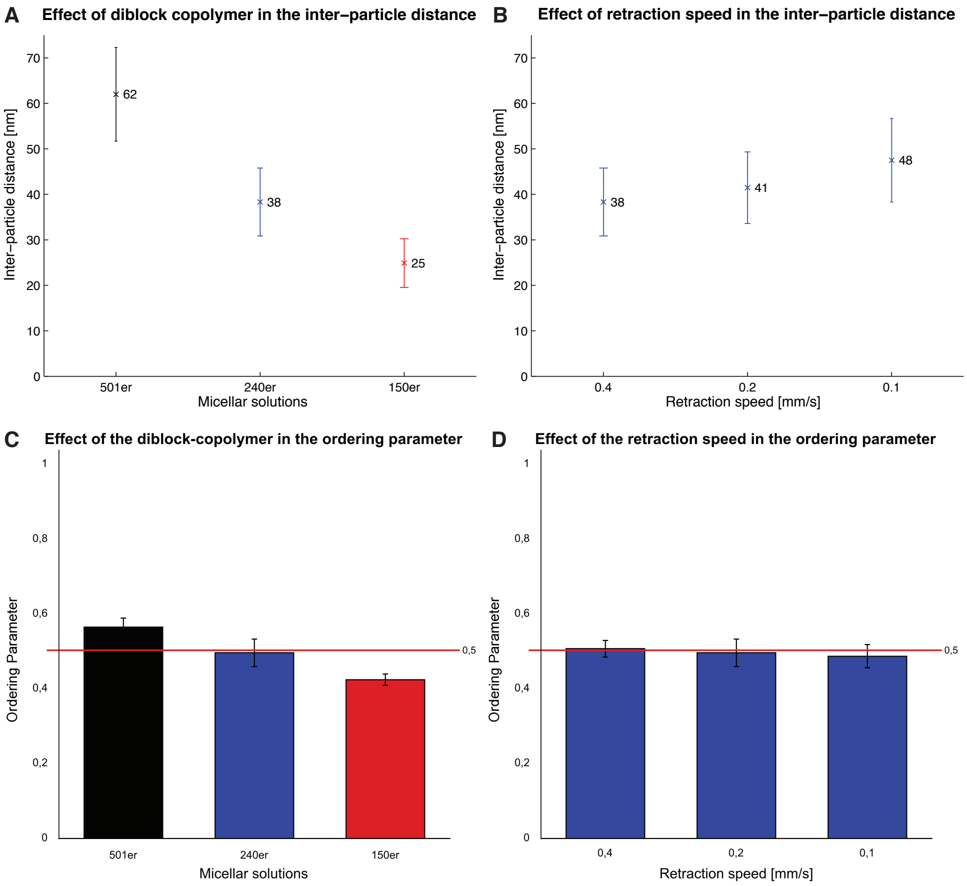

Figure 6.2: Characterization of the dip-coated surfaces. **(A)** ΔLs between the AuNPs obtained by varying the length of the diblock-copolymers. **(B)** ΔLs between the AuNPs obtainable by varying the dip-coating retraction speed. **(C)** Ordering parameters of AuNPs arrays obtained by dip-coating three different micellar solutions at a $0.2\,mm/s$ retraction speed. Red line represents the minimal acceptable ordering parameter set for the experiments (0.5). **(D)** Ordering parameters of AuNPs arrays obtained by dip-coating a 240er micellar solution at varying retraction speeds. Red line represents the minimal acceptable ordering parameter set for the experiments (0.5). Error bars refer to the standard deviation in the mean.

speed (if the substrate is retracted too rapidly from the solution, multilayers of micelles will pile up resulting in a tighter packing on the surface). However, the ability to influence the ΔL between the AuNPs is greater when varying the length of the diblock-copolymers than when varying the retraction speed. Therefore it is common to change polymers when radical differences in the ΔL between the particles are required. In all checked surfaces the ordering parameters were close to 0.5 or better. As mentioned in section 2.3.1, the osmotic repulsion of the solvating chains that lead to isometric micelles and consequently to a narrow size distributions is one of the factors accounting for perfectly ordered arrays of micelles. Figure 6.2 (C) shows clearly this trend as a decrease of the ordering parameter proportional to the shortening of the polystyrene chains (chains getting solvated by the selective solvent, toluene).

The size of the AuNPs is also relevant for the project as it influences how many ligands can link to a single particle. For that purpose, the surfaces were checked by Atomic Force Microscopy. An AFM image can be seen in figure 6.3. In agreement with data already published by the group, the size of the particles obtained by BCMN with a 240er micellar solution and L = 0.5 is between 8 and 12 nm. Due to sterical hindrances, it can be safely assumed that only one integrin will be able to link to each particle carrying the RGD motif and that the localization of particles, and after the bio-functionalization of the ligands, on the surface is translated into the localization of the receptors in the cells' membrane.

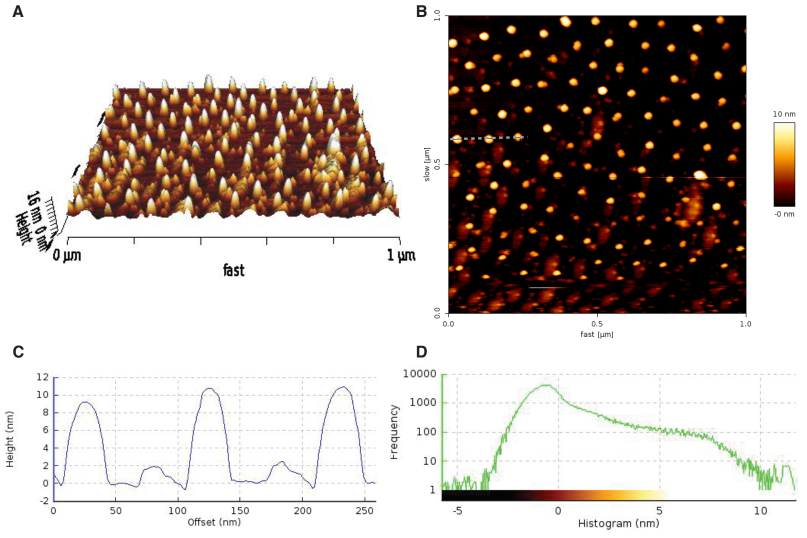

Figure 6.3: AFM scanings of the surfaces with AuNPs. **(A)** Image of an AFM scan showing a 3D reconstruction of the AuNPs deposited on the coverslips. **(B)** Image of an AFM scan showing a top view of the AuNPs deposited on the coverslips as bright points. **(C)** Height profiles of three AuNPs (gray dashed line in (B)). **(D)** Logarithmic height distribution of the scanned surface showing maximum height values between 8 and 12 nm.

6.2 Transfer of the AuNPs to a stretchable substrate

The transfer of the AuNPs to the HGs (transfer nano-lithography) is also crucial for this work, as the AuNPs are the only anchor points on the otherwise PEG protein repellent surface where the RGD ligand can bind. As shown in figure 6.4 occurs reliably thanks to the customized aluminum casting molds and the execution of an established protocol. Major improvement in the transfer nano-lithography technique was the introduction of a Hamamatsu Lightning cure LC8 lamp with a band pass filter for illumination at a very sharp peak at 365 nm making the curing much more accurate and precise. Moreover, the lamp has an internal feedback loop function that measures constantly the intensity of the beam and regulates the output power so that it matches the desires of the user.

Accordingly, we obtain a highly homogeneous light source which additionally is parallel thanks to the introduction of a fiber optic collimator between the end of the light guide and the sample holder. Since the whole setup is mounted on rails one could use it for much more sophisticated curing experiments, such as the production of stiffness steep gradients [Wong et al., 2003]. Unfortunately, during this work not every patterned HG could be checked for a successful transfer prior to the stretching experiments. The reason for that being the required integrity of the substrate that will enable a homogeneous, robust, uniform stretching. Instead, the process was periodically checked by performing additional transfer nano-lithography using the same conditions and chemicals but on a 10x10 mm HG that was then examined in the cryo SEM.

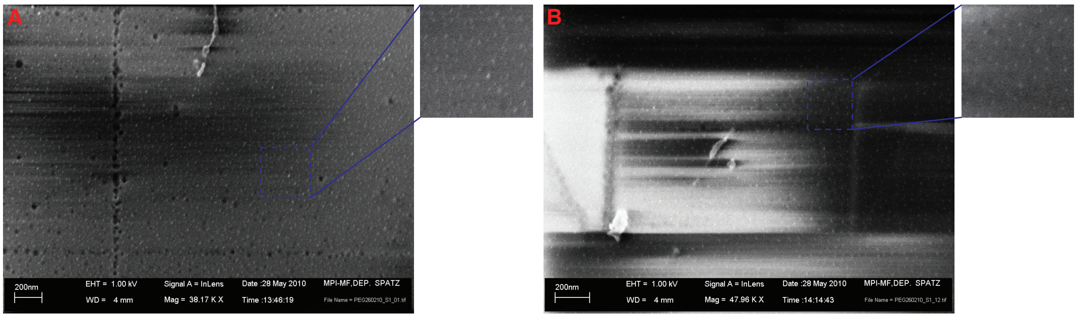

Figure 6.4: Characterization of the transfer nano-lithography. **(A)** 38000x magnified cryo-SEM image of AuNPs transferred to the PEG-10K-DA HGs' surface. A zoom in the blue dashed area is shown. **(B)** 48000x magnified cryo-SEM image of AuNPs transferred to the PEG-10K-DA HGs' surface. A zoom in the blue dashed area is shown.

Since it's not possible to apply ImageJ *Dot Analyzer* plugin to the cryo-SEM images, the ΔL between the AuNPs on the HGs' surface has to be calculated with the swelling ratio of the used 40 % w/v PEG-DA prepolymer solution. Results for the two tested prepolymer solutions with 40 % and 120 % w/v are summarized in figure 6.5. As expected, a less concentrated solution exhibits a lower swelling ratio because it's directly proportional to the cross-linking density which of course will be higher the more concentrated the diacrylate monomers are.

Equation 6.1 shows the calculated ΔL between the AuNPs (240er solution at 0.2 mm/s retraction speed) on the swollen PEG-10K-DA 40 % w/v HGs:

$$41\,nm \times 1.41 = 58\,nm \tag{6.1}$$

The ΔL between the AuNPs on the HGs' surface (58 nm) is at physiological levels where inter-ligand distances are regulated at 30-60 nm [de Beer et al., 2010] and below the critical ΔL (73 nm) that disrupts cell-spreading capabilities of REF cells [Cavalcanti-Adam et al., 2007].

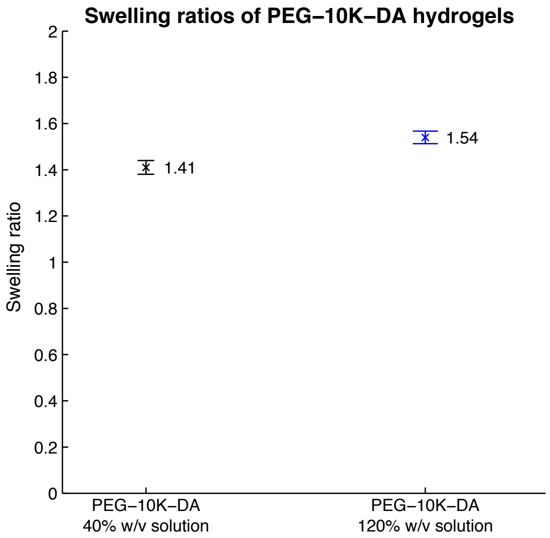

Figure 6.5: Swelling ratios of photo-polymerized HGs with different prepolymer % w/v concentrations solutions (40 % and 120 %). Error bars in substrate elasticity refer to the standard deviation of the mean.

6.3 Cell adhesion on ECM-mimetic, elastic PEG-DA HGs

6.3.1 Functionalization with the RGD motif to control the biochemical signals

In order to invoke preferentially the $\alpha_v\beta_3$, $\alpha_5\beta_1$ and $\alpha_{IIb}\beta_3$ integrins [Pfaff et al., 1994], the AuNPs bound to the HGs were bio-functionalized with the cyclo-(-RGDfK-)-thiol peptide depicted in figure 2.4. Figure 6.6 shows how cells can't spread to the PEG-DA HGs' surface unless particles have been transferred to the surface and these have been bio-functionalized with the RGD motif (no cells over the dipping edge, which is the upper-edge of the surface immersed in the micellar solution). Furthermore, it can be seen how the REF cells used in this study react different to increasing inter-ligand distances proving that the space between the ligands is protein repellent and that the AuNPs presented to the cells are in fact the only possible anchoring points to their underlying substrate.

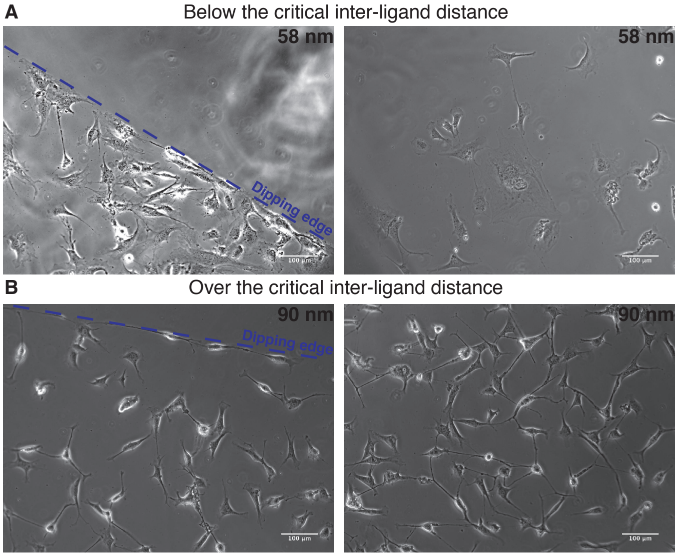

Figure 6.6: Comparison of cells spreading on HGs functionalized with AuNPs at different inter-particles distances. Dashed blue line represents the dipping edge. **(A)** Spacing of the peptides bound to the AuNPs on this surface (around 58 nm) is below the critical inter-ligand distance (73 nm). **(B)** Spacing of the peptides bound to the AuNPs on this surface (around 90 nm) is over the inter-ligand critical distance (73 nm).

6.3.2 Stiffness of the substrates

Another property of the HGs that may affect cells' ability to adhere and spread is their stiffness or Young's modulus. Below a certain critical value, anchorage dependent cells will not be able to generate the sufficient tension on the surface that enables them to build effectively actin fibers. It is widely known how cells respond through cytoskeleton organization to the resistance that they sense and how many cellular processes are optimized for a range of stiffnesses similar to their native environments [Discher et al., 2005]. For some kinds of fibroblasts this range of stiffnesses is around 10kPa, nevertheless during this work stiffer substrates were employed mainly for two of reasons:

1. In order to be able to stretch cells and the FAs plaque a material stiffer than the structures to be stretched is needed. Otherwise the strain will not be transferred 1:1 to them and the effective amplitude of the stretching steps will get reduced.

2. Given that the HGs have to be thin so that microscopy techniques can be applied through them, stiffer HGs are easier to handle.

Characterization was conducted through indentation experiments with a JPK AFM on the un-functionalized surfaces of PEG-10K-DA HGs polymerized under the same conditions as the substrates used for cell experiments (Figure 6.7).

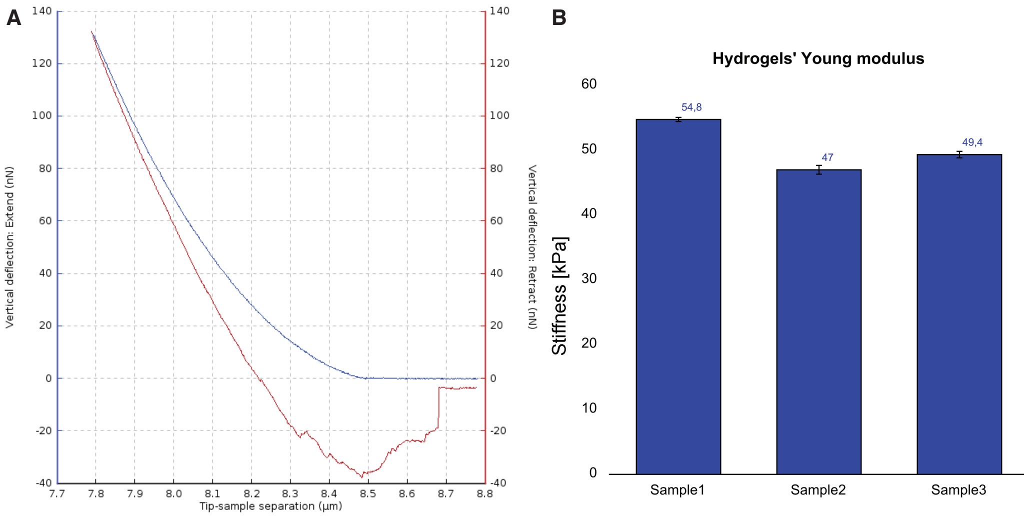

Figure 6.7: (A) Example of a force-distance curve obtained with a JPK AFM on the surface of a PEG-10K-DA HG. Blue line represents the indentation of the tip on the surface and the red line the retraction. **(B)** Young's modulus of three 40 % w/v PEG-10K-DA HGs (each sample three different positions). Error bars in substrate elasticity refer to the standard deviation of the mean.

Mean Young's modulus for the three samples of a same batch is 50.5 ± 3.9 kPa ($n = 3$) which is in good accordance with data previously reported in the group [Louban, 2009] and high enough for the cells to assemble stress fibers [Zemel et al., 2010] and for the HGs to transmit the strain to the cells and to the FAs. AS a matter of fact, based on a thorough characterization of the stiffnesses of HGs of different concentrations [Louban, 2009] a 40 % w/v concentration was deliberately chosen so that HGs had a higher stiffness than fibroblasts.

6.4 Uniaxial, static stretching of the HGs

6.4.1 Stretching method combining casting and pulling

Stretching HGs (a mesh of long, highly hydrated, interconnected chains with a high water content) in a reproducible and controlled manner was indeed the mayor challenge to be overcome during the presented work for two reasons:

1. Risk of slipping away: The presence of water in the HGs and around them turns them into slippery bodies as shear friction between thin layers of water is considerably lower than friction between dried solids.
2. Risk of ripping apart: HGs have to be thin so that light can go through with limited perturbation and pliable so they can be stretched. Appropriate protocol for their handling and stretching had to be established.

As already mentioned, the casting mold defined the final shape of the HGs and these in turn defined the required clamping procedure to be able to apply the stretching steps, so the optimal combination between casting mold and pulling method had to be chosen. Figure 6.8 shows the potential stretching methods evaluated for this work.

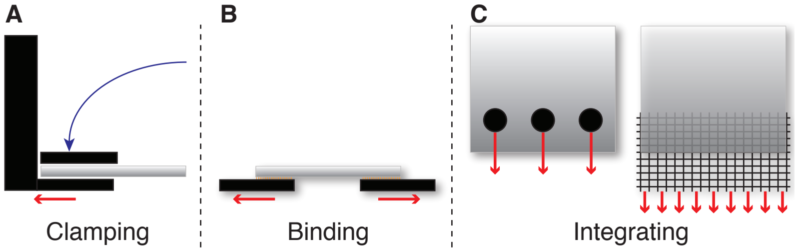

Figure 6.8: Potential stretching methods evaluated for this work. **(A)** Clamping the HGs between a clamp and an upper, screwable cover. **(B)** Binding of the HGs to a support and pulling from the support. **(C)** Integrating elements in the HGs and pulling from the elements.

Table 6.1 lists advantages and disadvantages of the methods and the outcomes of the tests. The highest priority was to have a reliable and reproducible method to trasmitt the strain to the HGs because a visual confirmation was difficult: Transparent samples immersed in a semi-transparent liquid and partially hidden by the clamps at the sides and the objective on the top. In order to monitor the strain transmission to the HGs during the tests, latex μ-beads were copolymerized in the HGs and the distance between them was used as internal measurement of the strain.

Table 6.1: Evaluation of the stretching methods.

METHOD	**Clamping**	**Binding**	**Integrated Mesh**	**Integrated Cylinder**
Advantages	Clean Simple	Good grip	Good grip	Clean Good grip Reproducible
Disadvantages	Weak grip Not reproducible	Complicated Not reproducible	Disruptive swelling	Time consuming
Tests	Slip or rip	Not tested	Ripped	Successful

Clamping of the HGs and pulling

For the casting of the prepolymer solution, simple microscope slides were used on which teflon sheets of different thickness were glued to serve as spacers defining the width of the HGs (Figure 6.10 (A)). Depending on the pressure applied to the sample via the clamps, they got ripped or slipped already during the stretching steps or the first seconds of observation. Transmission of the strain could not be quantified.

Binding of the HGs and pulling from the supports

Binding the HGs covalently to a support and pulling from these supports was a promising method in terms of the grip it could provide. However, the gluing step added further complexity to the handling of HGs. Furthermore, many glues are known to be cytotoxic or to release substances. For these reasons this method was no tested but can be considered for other similar setups where no cells are involved.

Integrating elements in the HGs and pulling from these elements

Meshes were expected to transfer the strain very uniformly to the HGs as the prepolymer could flow through them and the contact between the gels and the meshes was maximal [Raeber et al., 2008]. Figure 6.9 shows the three kinds of meshes used. Rigid meshes with holes diameter of 2 and 1 mm were totally destructive for the gels acting as scissors cutting through them during swelling. A more flexible mesh was then used consisting of intertwined aluminum wires leaving 2 mm openings, however with the same disruptive swelling behavior.

In order to integrate the cylinders in the HGs, holes were needed. Punching the HGs was not desired because it would make the process highly unreproducible (difficult to accurately punch all the holes always in the same position relative to the HG and to each other) and the risk of harming the HGs would be higher. Instead, casting molds were manufactured so that the HGs would incorporate the holes already during their curing process. However, the casting mold and the pulling clamps had to be consistent with each

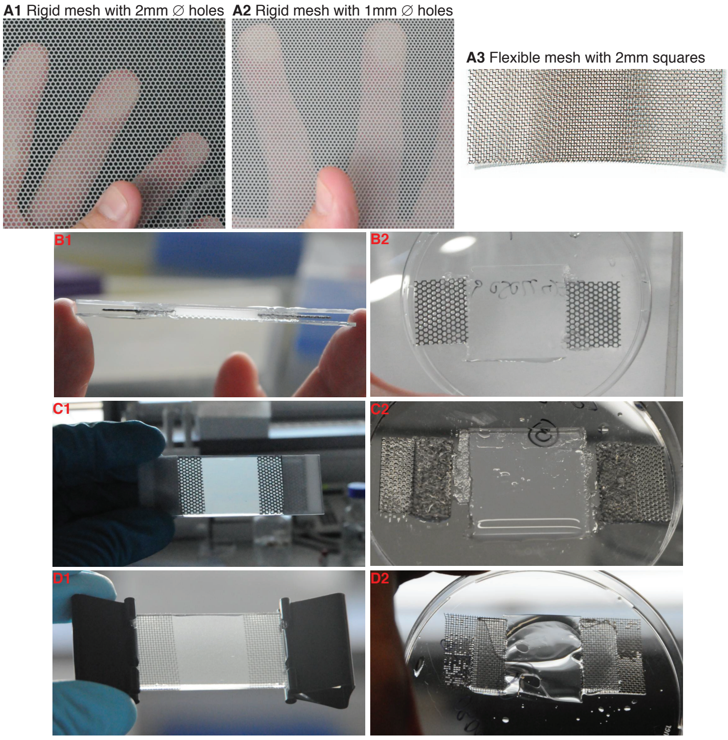

Figure 6.9: Integrated meshes. **(A)** (1, 2, 3) Different meshes tested in this work. **(B)** (1) Assembled rigid meshes with 2 mm diameter holes and (2) result after the polymerization and swelling. **(C)** (1) Assembled rigid meshes with 1 mm diameter holes and (2) result after the polymerization and swelling. **(D)** (1) Assembled flexible meshes with a 2 mm grid and (2) result after the polymerization and swelling.

other, i.e. the casting mold had to be designed, manufactured and then tested together with the designed clamps until the combination of both lead to reproducible, consistent and reliable transmission of the strain. This iterative process where molds specifications set in turn the specifications of the clamps to be used was simplified by the fact that HGs swell isotropically: Swelling only changed the size of the original HG while maintaining the original shape. In order to design the clamps, the dimensions of the molds (specially size of the cylinders and the space between) had to be simply multiplied by the HGs' swelling ratio. Figure 6.10 presents the different working versions of the molds.

HGs with four holes ripped between the holes very often during the stretching (point of stress application) most probably because perforation was too high and there was not enough material from which to pull. Transmission of the strain could not be quantified.

In terms of the HGs with three holes, two possible morphologies (rectangular vs. dog-bone shaped) were compared (Figure 6.11. The blue line is obtained by manually tracking the μ-beads and calculating the distance between them after every stretch step. The black line represents the separation between the clamps. The orange line represents a linear polynomial ($y = a * x + b$) fit to compare the transmission of strain. Stretch was applied in small steps in order to be able to follow the copolymerized μ-beads (displacement in the z-

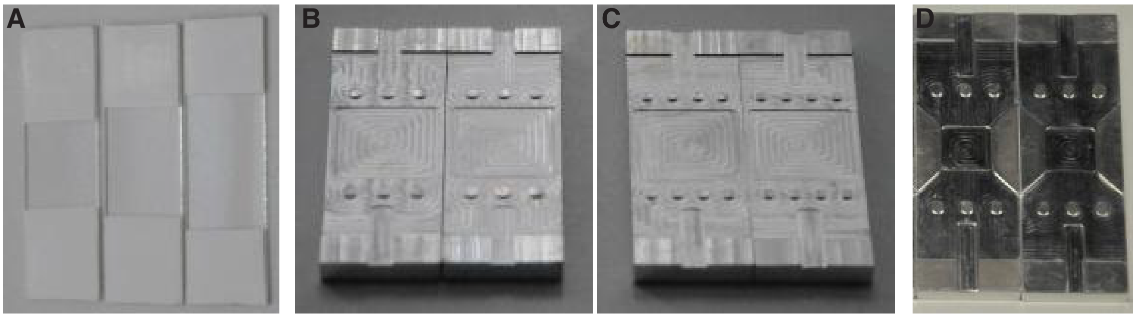

Figure 6.10: Customized casting molds tested in this work. **(A)** Self-made glass casting molds to produce rectangular HGs of different lengths. **(B)** Engineered aluminum casting molds to produce rectangular HGs with three holes. **(C)** Engineered aluminum casting molds to produce rectangular HGs with four holes. **(D)** Engineered aluminum casting molds to produce dog-bone shaped HGs with three holes.

direction) under the microscope and quantify the applied strain. In rectangular HGs strain transmission was inefficient (41 % as shown by the slope of the fitted line). With the dog bone shaped HGs the efficiency of the strain transmission was much higher (87 % as shown by the slope of the fitted line, i.e. 2.12 times more efficient than for rectangular HGs). Due to the fact that prolonged stretch can have inhibitory effects [Wang and Thampatty, 2006] and after a review of the related literature [Brown, 2000], during this work a strain of 15 % was aimed to be transmitted to the HGs. With the fit the actual strain at the step when 15 % should have been reached could be calculated (Equation 6.2).

$$\begin{aligned} \%\ \text{Strain} &= 0{,}87 \times 15\,\% + 0{,}022 \\ \%\ \text{Strain} &= 13{,}07\,\% \end{aligned} \tag{6.2}$$

The question arose whether HGs remain in the stretched state, for how long and how reproducibly. For that purpose, a series of dog-bone shaped HGs containing three holes were stretched in two 7.5 % steps and monitored for a total of 45 minutes. In this case triads of μ-beads were tracked so that the two components of strain could be quantified: tensile describing the extension in the stretching direction and compressive describing the compression in the direction perpendicular to the stretching direction (Figure 6.12). It can be seen how the transmission of strain gets really close to the intended final 15 % tensile strain and the corresponding 7,5 % compressive strain (13.6 % and 6.2 % respectively in figure 6.12*).

Consequently, a dog-bone shaped casting mold with three cylinders was used to cast-in the prepolymer solution and confer the HGs with the optimal morphology for a homogeneous, reproducible and efficient stretching. A close-up in one of such molds can be seen in figure 6.13. Colored coded are the advanced functionalities: The red-dashed area in the middle is where the patterned cover slip with the AuNPs facing upwards laid. The

---

[*] HGs can be approximated to perfectly incompressible materials deformed elastically and to have a Poisson´s ratio of 0.5 [Raeber et al., 2005, 2008]

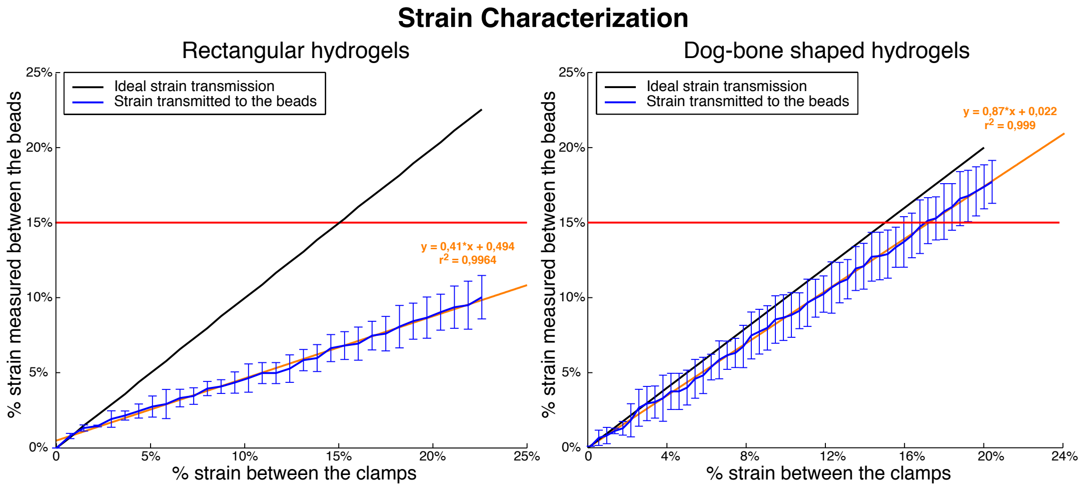

Figure 6.11: Effect of the morphology of the HGs in their strain to stress response. The blue line is obtained by manually tracking the μ-beads and calculating the distance between them after every stretch step. The black line represents the separation between the clamps. Red line represents the aimed 15 %. Orange line is a linear polynomial fit ($y = a * x + b$). **(A)** Strain transmission to rectangular shaped HGs. **(B)** Strain transmission to dog-bone shaped HGs.

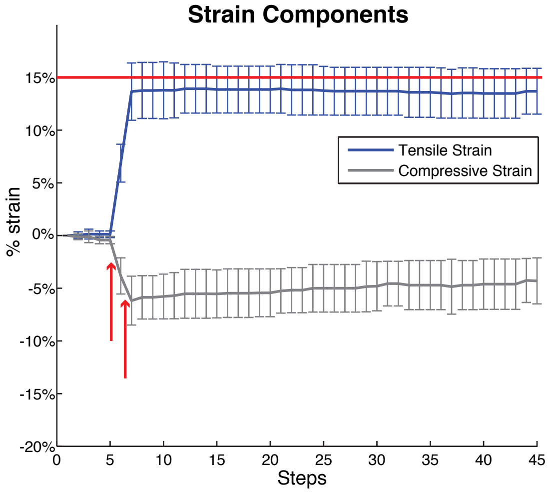

Figure 6.12: Quantification of the applied strain and further observation of the stretched HGs. Strain presented as the absolute distance between the μ-beads. Blue line represents tensile strain and gray line represents compressive strain. Steps 6 and 7 are the stretching steps (indicated by the red arrows). Red line represents the intended 15 %.

yellow-dashed areas are the side openings through which the air could exit the construction as the prepolymer solution homogeneously flows in. The blue-dashed areas correspond to the cylinders that will become holes in the final HGs after polymerization. Finally the black-dashed areas are the platforms where the covering quartz-glass slides laid closing the volume. It's also shown the additional equipment needed for the casting of the HGs and the assembled construction ready to be used.

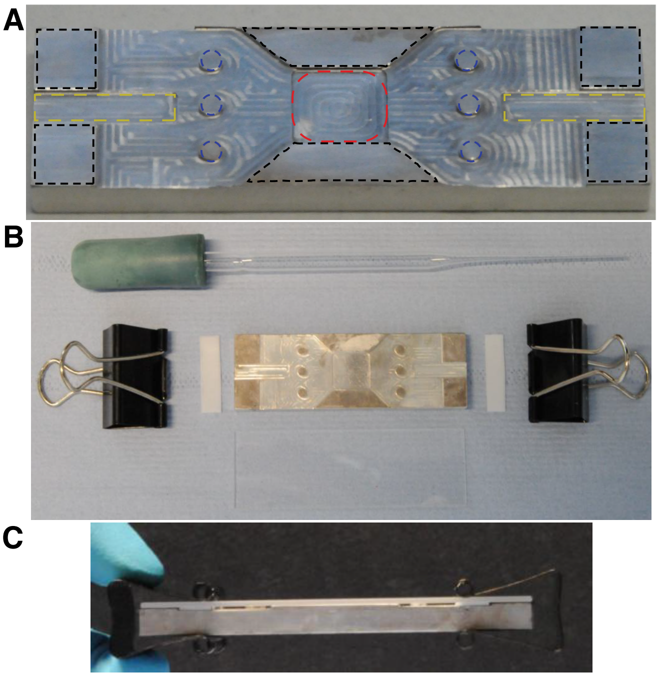

Figure 6.13: Customized casting equipment. **(A)** A detailed image of the final casting mold used to cross-link the prepolymer with the color coded features described in the text. **(B)** Basic additional equipment: a glass Pasteur pipette, a pair of office metallic clamps, white Teflon spacers and a covering quartz microscope-slide. **(C)** All parts assembled and ready for casting

6.4.2 Characterization of the strain field

In order to check the homogeneity of the strain field on the HGs' surface an Autodesk Inventor Professional© strain field analysis was conducted (with the kind help of PhD student Martin Deibler). Results can be seen in figure A.3 as a color-coded distribution of the deformation along the length of the substrate. It can be clearly seen how the deformation increases gradually and uniform, being obviously highest at the points where the load is applied and lowest in the middle. It can be concluded from this analysis that in the center of the HGs the applied strain is homogeneous and that cells spread in this area will be subjected to similar levels of strain.

6.4.3 Anisotropy in the AuNPs pattern

In order to understand the effect of an anisotropy in the AuNPs pattern on the integrin signaling capabilities of the cells, it's necessary to analyze how the quasi-hexagonal ordering of the AuNPs gets disrupted by the stretching step.

Before the stretching only h is unknown because $a_d = a_h = 58\,nm$ and $\alpha = 60°$. h can be calculated by using the Pythagorean theorem as shown in equation 6.3.

$$\begin{aligned} h^2 + \frac{{a_h}^2}{2} &= a_d^2 \\ h &= 50.22\,\text{nm} \end{aligned} \tag{6.3}$$

When the pattern is stretched, there will be a change in the magnitudes of all listed variables (represented with the $'$ symbol). Knowing the theoretical values of tensile (15 %) and compressive (7.5 %) strain $a'_h = a_h \times 1.15$ and $h' = h \times 0.925$. In order to calculate α'

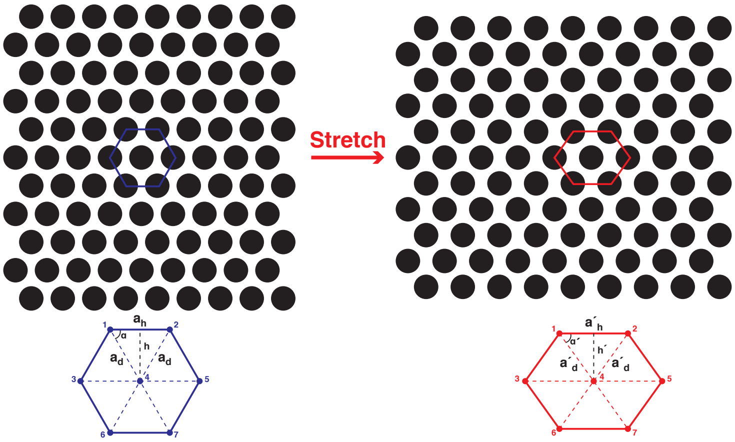

Figure 6.14: Hypothesized anisotropy in the AuNPs' array. Self drawn hexagonal ordering and effect of a 15 % stretching step. The blue hexagon represents seven particles before stretching and the red hexagon represents seven particles after stretching. Variables of importance are indicated in black.

with the help of basic trigonometric functions the known variables can be substituted in equation 6.4:

$$\begin{aligned} \tan\alpha' &= \frac{h'}{\frac{a'_h}{2}} \\ \alpha' &= 54.32\,^\circ \end{aligned} \tag{6.4}$$

Finally, a'_d can be determined as follows in equation 6.5:

$$\begin{aligned} \sin\alpha' &= \frac{h'}{a'_d} \\ a'_d &= 57.19\,\mathrm{nm} \end{aligned} \tag{6.5}$$

The value obtained for a'_d is very close to the initial value for a_d meaning that for each hexagon of particles considered alone only the distance between particles 1 and 2 ($\overline{12}$), between particles 3 and 4 ($\overline{34}$), between particles 4 and 5 ($\overline{45}$) and between particles 6 and 7 ($\overline{67}$) are increased whereas $\overline{41}$, $\overline{42}$, $\overline{46}$ and $\overline{47}$ remain effectively unaltered.

In order to get the ΔL between all particles drawn in the diagram an ImageJ self-written routine (PhD student Stefan Quint) was used that calculates pairwise distances (Figure 6.15).

The values of the radial distribution function were normalized by the factor ($2 \times \pi \times$ pairwise distance $\times$ particles density). By comparing the pairwise distances before and after the stretching the anisotropy of the AuNPs pattern could be characterized. In blue (before stretching) the peak at 58 nm corresponds to a_d and a_h. The peak at 100 nm ($2*h$) corresponds to the distance between the central particles (4) of two adjacent hexagons. The peak at 116 nm ($2*a'_h$) corresponds to the distance between two non-adjacent particles parallel to the stretch direction. In red (after stretching) the peak around 58 nm gets split into two smaller peaks at 57 nm (a'_d) and 67 nm (a'_h). A new peak appears in the stretched state at 94 nm ($2*h'$) which corresponds to the distance between the central particles (4) of two adjacent hexagons in the stretched state. Another new peak appears at 115 nm (a'_d) corresponding to the diagonal distance between the central particles (4) of two adjacent

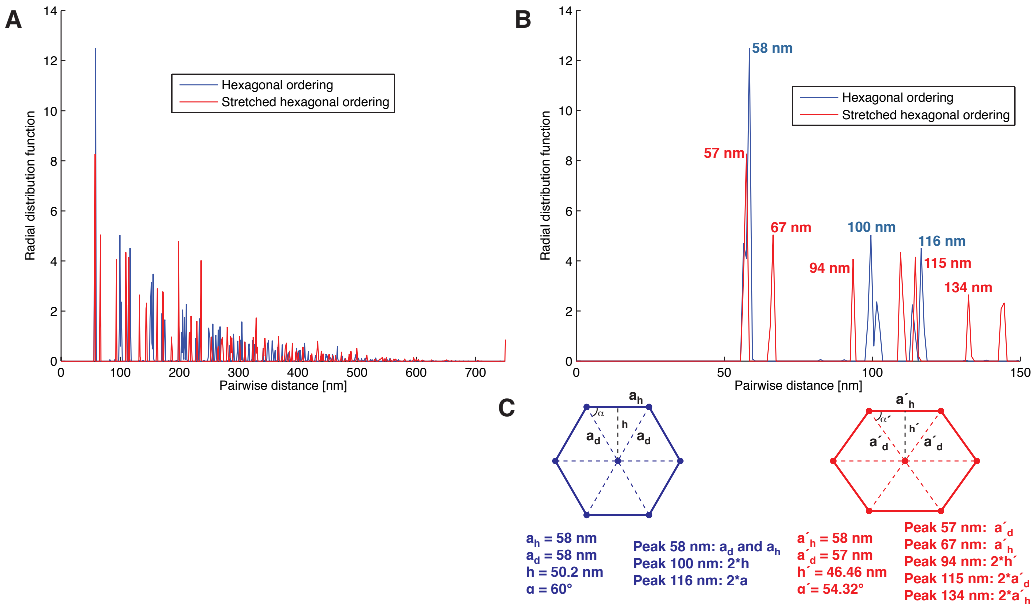

Figure 6.15: Theoretical anisotropy in the AuNPs' array. **(A)** Pairwise distance between all particles. **(B)** Pairwise distance between particles up to an ΔL of 150 nm. **(C)** The blue hexagon represents seven particles before stretching and the red hexagon represents seven particles after stretching. Hypothesized correspondence between peaks in the graphs and the variables is shown. Variables of importance are indicated in black.

hexagons. Finally the peak at 134 nm $(2 * a'_h)$ corresponds to the distance between two non-adjacent particles parallel to the stretch direction. Further peaks are not of interest for this work because the distances between the particles are then out of the range molecular inter-actuators (α-actinin, FN,...) can bridge.

Chapter

7

Cell response to uniaxial, static strain

The main goal of this work was to establish a reliable and reproducible method to stretch static and uniaxially PEG-based HGs seeded with living cells. For that purpose, the % w/v of the HGs, the casting procedure and the stretching method had to be optimized. Additionally the required image processing and data analysis tools to conduct cell adhesion and FAs morphology studies had to be put in place.

7.1 REF-YFP-Pax cells morphology on the HGs

Starting point of the comparison of cells response was their reaction to the different surface functionalizations used in this work (PEG-10K-DA HGs + AuNPs + RGD vs. PEG-10K-DA HGs + FN). Looking at the un-normalized values of cells' mean area a considerable difference could be seen between cells seeded on HGs + FN (5,576 ± 575 μm^2) and cells seeded on HGs + AuNPs + RGD (2,387 ± 239 μm^2) (Figure 7.1).

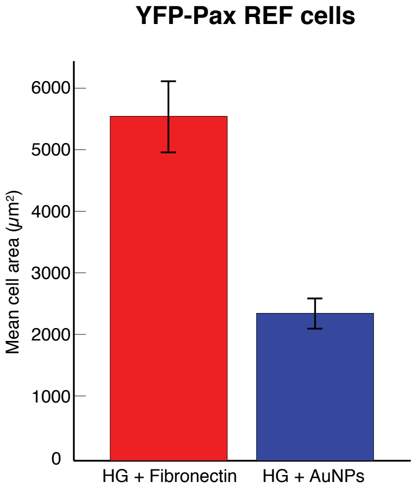

Figure 7.1: Area of the YFP-Pax REF cells seeded on PEG-10K-DA HGs + FN (red) and on PEG-10K-DA HGs + AuNPs + RGD. Error bars correspond to the standard error of the mean (n = 7-10).

Cells seeded on HG + AuNPs + RGD are presented with a restricted availability of anchoring points (~ 500 molecules per μm^2 on a 58 nm patterned surface [Cavalcanti-Adam et al., 2007]) maybe leading to an insufficient receptor density in the cell's membrane and to an incomplete spreading of the cell (the so called low-density focal adhesions [Wehrle-Haller and Imhof, 2002]). Mean area value of cells seeded on HG + AuNPs + RGD at an inter-ligand distance of 58 nm is in good accordance with data already published in the group (2,712 ± 752 μm^2) [Cavalcanti-Adam et al., 2007]. The higher mean area value for cells seeded on HG + FN may come from the homogeneous availability of anchoring points or from additional signals coming from FN molecules arranged on the surface in a manner that cryptic sites are revealed [Pompe et al., 2005, Vogel, 2006].

Additionally, the FAs of the YFP-Pax REF cells seeded on HGs + AuNPs + RGD and on HGs + FN were compared (Figure 7.2). YFP-Pax REF cells seeded on HGs + FN have a higher mean number of FAs (191 ± 20) than on HGs + AuNPs + RGD (88 ± 11). The mean area value of FAs of YFP-Pax REF cells on HGs + FN is however lower (0.91 ± 0.03 μm^2) than on HGs + AuNPs + RGD (1.71 ± 0.12 μm^2).

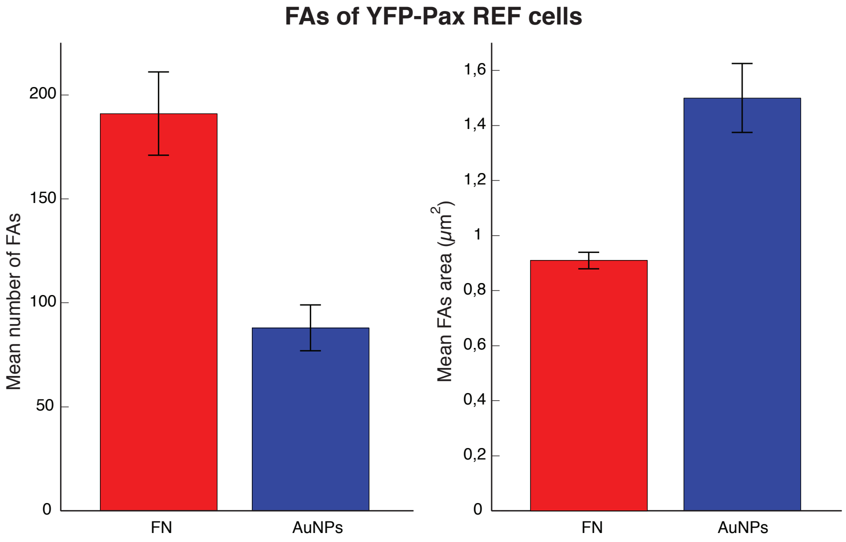

Figure 7.2: Mean number and mean area value of FAs of the YFP-Pax REF cells seeded on PEG-10K-DA HGs + FN (red) and on PEG-10K-DA HGs + AuNPs + RGD. Error bars correspond to the standard error of the mean (n = 7-10).

The values of mean area of the FAs on HGs + AuNPs + RGD are smaller than previously reported in the group for similar substrates (5.5 ± 2.9 μm^2 [Arnold et al., 2004], 4.4 ± 2.2 μm^2 [Arnold et al., 2009]) although other studies studying the molecular diversity of cell-matrix adhesions show that a big part of the adhesion sites population falls below 2.5 μm^2 [Zamir et al., 1999]. The values of mean area of the FAs on HGs + FN are even smaller. The reason why FAs are in general smaller may come from the thresholding applied to the images during this work as part of the high-throughput FAs analysis routine established. The explanation why the FAs of cells seeded on HGs + AuNPs + RGD are larger than on HGs + FN maybe that on a surface where only $\sim$ 500 molecules per μm^2 a larger area is needed in order to establish the adhesive point. However the picture is incomplete unless the total FA area is contemplated (number of FAs multiplied by the mean average area value). Total FA area value of cells on HGs + AuNPs + RGD is 132 μm^2 which represents a 5 % of cells total adhesive area. Total FA area value of cells on HGs + FN is 173 μm^2 which represents a 3 % of cells total adhesive area. Although cells on HGs + FN have a value of focal adhesive area a 31 % higher than on HGs + AuNPs + RGD the fraction of FA adhesive area to total cell area is similar in both cases. The slight higher value for cells on HGs + AuNPs + RGD may come from the aforementioned restricted ligand availability that forces cells to expand their FAs so that enough ligands are included.

7.2 Transmission of strain to cells and FAs

7.2.1 Cell adhesion under strain

In the literature it has been described how cells can be subjected to different kinds of strains and to a wide range of amplitudes and frequencies (in the case of cyclic stretch) [Brown, 2000, Jungbauer et al., 2008, Wang and Thampatty, 2006]. However, during this work a restricted availability of anchoring points was presented to the cells and the cells were then pulled grabbing from these anchors. A series of questions arose: Are the HGs stiff enough to transmit the strain to the cells and FAs? Are cells and FAs co-stretched with their underlying substrate or do cells detach of the HGs as a result of the stretching? Do AuNPs remain at the HGs' surface when the strain is applied to the mesh of the HGs or does the elongation of the mesh produce a compression in the z-direction and a retraction of the AuNPs from the surface? For that purpose, cells were observed after the application of the strain, and the strain transmitted to cells and FAs was quantified (Figures 7.3 and 7.4).

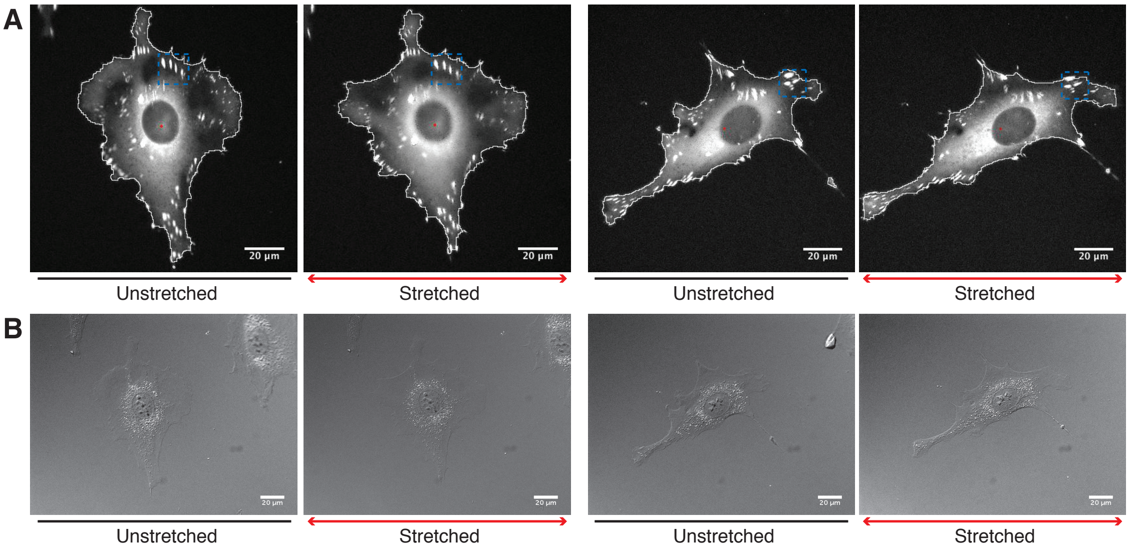

Figure 7.3: Cells being stretched with a 15 % amplitude on the HGs. Blue dashed areas represent the areas shown in figure 7.4 to provide a zoom-in of the FAs. **(A)** Fluorescent images of two cells getting stretched on the HGs. **(B)** DIC images of two cells getting stretched on the HGs' surface.

Figure 7.3 (A) shows images of cells getting co-stretched with their underlying substrate (extension along the main strain direction and compression perpendicular to the strain direction). Figure 7.3 (B) shows how the HGs' surface remains flat after the stretching and no wrinkles appear (the presence of a stiffer object adhered on the surface could generate a surface perturbation visible in wrinkles around the cells).

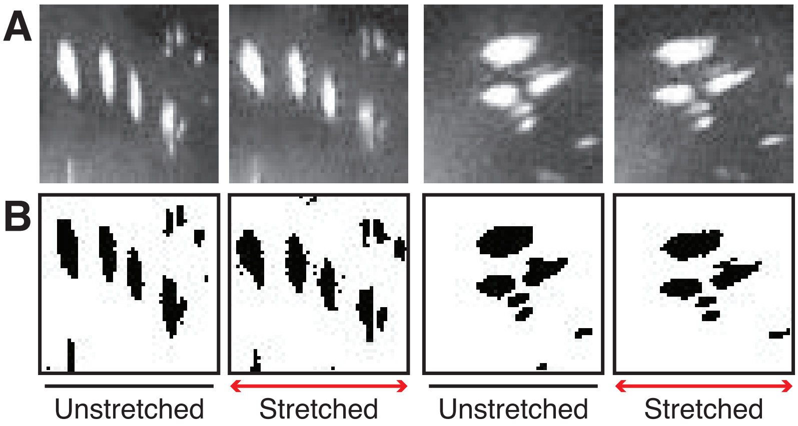

Figure 7.4: FAs being stretched with a 15 % amplitude on the HGs. **(A)** Fluorescent images of FAs getting stretched on the HGs (extension along the main strain direction and compression perpendicular to the strain direction). **(B)** Images of FAs getting stretched on the HGs' surface processed with the *iFAs* ImageJ routine.

Figure 7.4 (A) shows images of FAs getting co-stretched with their underlying substrate. Figure 7.4 (B) shows Images of FAs getting co-stretched on the HGs' surface processed with the *iFAs* ImageJ routine. The bright bodies of the FAs in the fluorescent image get accurately processed as a black particles.

7.2.2 Quantification of strain applied to the cells and FAs

Quantitative verification of the strain being imposed upon the cells was accomplished through the application of the ImageJ macro *iPixel* (Figure 5.4) to the region of interest of the cells (30 % as defined in section 5.2.2). Additionally, the strain transmitted to a selected number of cells was quantified by manually measuring width and height of the cells before and after stretching and applying the equations 5.4 and 5.5. Figure 7.5 shows the results obtained with the macro and the results of the manual measurements.

In the case of the strain measured with the macro a higher variability in the strain values was measured. With the macro a wide portion of the cell is measured and cells' inherent protrusion activity is being co-measured (as shown in the tensile strain values 3.9 ± 1.2 % and compressive strain values 2.2 ± 2.7 % in the un-stretched state where no stretching was applied to the substrate), which was in turn translated in a supplementary (positive for protrusion and negative for retraction) change in the width and height of the cell. Contrarily, when the cell was manually measured it was intentionally done on a single line where no protrusion activity was apparent and close to cell's CofM. Nevertheless, there's a substantive difference between the strain values measured with *iPixel* for the stretched (tensile 10.8 ± 2.2 % and compressive 8.3 ± 1.5 %) and the un-stretched cases proving that the macro is useful to quantify the approximate strain applied to a wide population

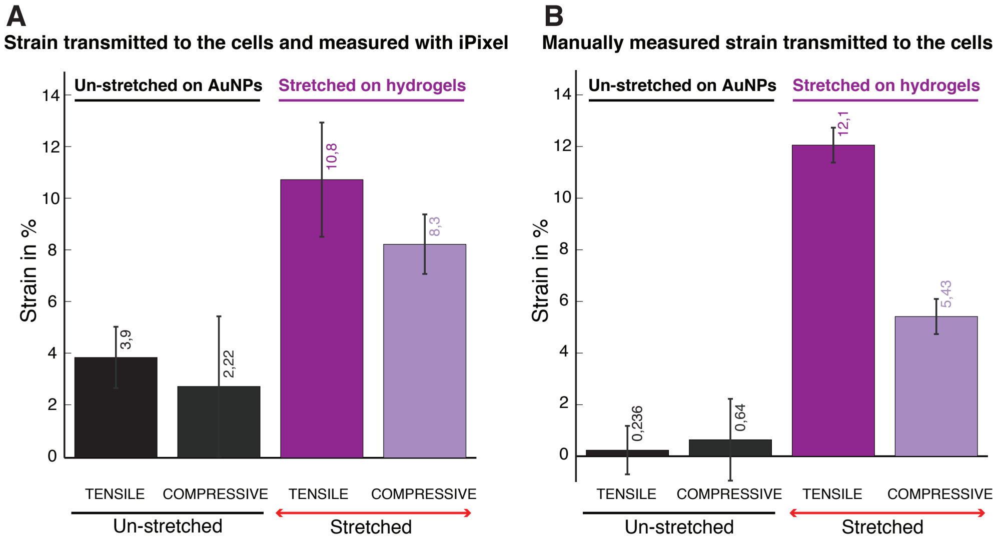

Figure 7.5: Quantification of the strain transmitted to the cells on the HGs. Stretched represents the comparison between the images of the cells before and after the stretching steps. Un-stretched represents the comparison between the images in the control films equivalent to the before and after stretching time-points. Error bars in strain refer to the standard deviation in the mean. **(A)** Tensile and compressive strain applied to the cells and measured with the ImageJ macro *iPixel* on the central 30 % part of the cells. **(B)** Strain applied to the cells and measured manually in ImageJ

of cells, fast and with the possibility of changing the range of the region of interest by typing a number during its execution.

In the case of the strain measured manually: The values for tensile and compressive strain in the stretched case (tensile 12.1 ± 0.7 % and compressive 5.43 ± 0.7 %) validate the approach of this work ranging from the choice of the substrates characteristics to the stretching and the quantification methods: a 91,7 % of the strain imposed onto the HGs (13,2 %) is transmitted to the cells (12,1 %). Transmission of strain from HGs to cells may have an efficiency lower than 100 % because fibroblasts can be seen as stiff bodies [Engler et al., 2006]. One could even theorize about stretching HGs seeded with cells as a single cell force spectroscopy (SCFS) method, in which different kind of cells seeded on HGs of the appropriate stiffness and pulled under scrutiny with controlled forces could shed some light on the dynamics and the magnitudes of cells reaction to an imposed stimuli. Moreover, Poison's ratio calculated between tensile and compressive elements of strain transmitted to the cells is 0.448, close to the theoretical 0.5 of incompressible materials. In the un-stretched state there's still a low level of protrusion activity being measured as strain (tensile 0.2 ± 0.9 % and compressive 0.6 ± 1.6 %) but considerably lower than for the *iPixel* case.

Furthermore, the biological focus of this work lied on the FAs of the cells. In order to quantify the strain transmitted to the FAs an ellipse was fitted to a selected number of FAs (Figure 7.6). With the values of major axis and angle of the major axis to the direction of strain application, the parallel and perpendicular components of the axis to the stretch direction and with them tensile and compressive strain could be calculated (equations 5.4 and 5.5).

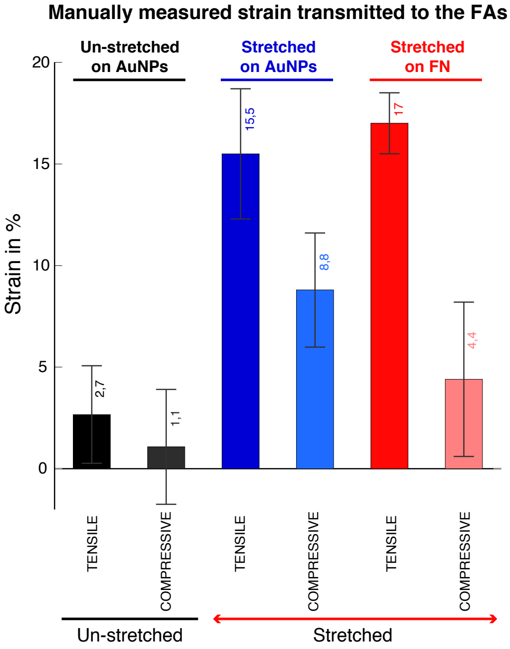

Figure 7.6: Quantification of the strain transmitted to the FAs on the HGs. Stretched represents the comparison between the images of the FAs before and after the stretching steps. Un-stretched represents the comparison between the images in the control films corresponding to the before and after stretching time-points. Error bars in strain refer to the standard deviation in the mean.

The apparent levels of strain in the un-stretched state (tensile 2.7 ± 2.4 % and compressive 1.1 ± 2.8 %) are high in comparison to those measured for the cells meaning that there is a change in the FAs' morphology in the equivalent period of time between before and after stretching. The reason for this variability may hide in a combination between the autofocus routine on the microscope and the posterior image processing done with ImageJ. In order to segment the images into features of interest and background, grayscale values were manually set to lower and upper threshold values, so that only the FAs appeared as particles. Although the thresholding values were kept constant for an entire film, there were some slight variations in the focus planes between the time points of the film. As a result, a constant thresholding applied on structures with slightly different grayscale values could originate black bodies with slightly different morphologies that could be interpreted as tensile or compressive strain. A dynamic threshold where the lower and upper values are adapted so that the real shape of FAs is captured in a more reliable manner could be one of the possible solutions, however such level of sophistication in the image processing was out of this work's scope. Another possibility could be that the FAs react actively to the fluorescent light with a higher turnover, however a visual inspection of the un-processed films ruled this possibility out leading to the conclusion that it is an artifact introduced by the image processing.

In the stretched state, a differentiation was done whether cells were stretched on HGs + AuNPs + RGD (blue) or on HGs + FN (red). Higher tensile and compressive strain values (Figure 7.6) are measured than in the case of cells' strain. Most direct explanation would be the mentioned image processing artifact affecting FAs' morphology. Another possibility could be that due to the dynamic nature of FAs (with turnovers in the range of minutes [Schneider et al., 2009]) their morphology varies slightly in the time period between before and after stretching. A third possibility could be that for the same strain being applied FAs' morphology reacts differently to cells' morphology. This apparent contradiction could be accounted for if we consider cells and FAs from their mechanical properties point of view, more specifically isotropy. A material is said to be isotropic in a property if this property remains identical in all directions (in this case morphology variation to an applied strain). Given the higher complexity of cells with cytoskeleton elements laid in random directions they can be approximated to a homogeneous continuum and hence considered isotropic [Vaziri and Gopinath, 2008]. Due to the random spatial arrangement of inner elements the orientation of the cell relative to the direction of the stretch is irrelevant for how its morphology varies. However in the case of FAs, orders of magnitude smaller than cells, the spatial arrangement of structural elements may lead to a discrete nature and hence display an anisotropic morphology variation to strain (poison's ratio of 0.57 for FAs stretched on HGs + AuNPs + RGD and of 0.26 for FAs stretched on HGs + FN). Examples abound in literature about isotropic structures with abnormal poison's ratios [Lee and Lakes, 1997]. As a matter of fact Clare M. Waterman describes integrin-based cell adhesions as having a layered architecture [Kanchanawong et al., 2010] and Hornberger et al. [2005] proposes a model (shown in figure 7.7) where they present actin cytoskeleton-linked multiaxial stretch-specific mechano-sensors that react distinctly to multiaxial vs. uniaxial stretch.

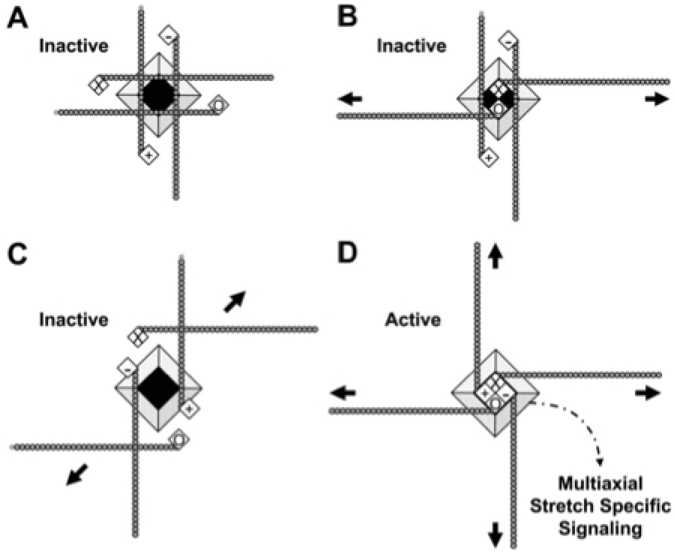

Figure 7.7: Anisotropic FAs. The relative FA protein positions determines the biochemical outcome of the applied stretch. **(A)** Without input the FA remains inactive. **(B)** and **(C)** Uniaxial stretch does not initiate signaling. **(D)** Multiaxial stretch combined with the anisotropic nature of FA architecture initiates the signaling [Hornberger et al., 2005].

7.3 Analysis of cells' temporal change in the stretched state

All figures of this section have the same organization: graph on the left hand-side shows the temporal change of the parameter in discussion for cells both parallel and perpendicular to the stretch direction. Graph in the middle shows the temporal change of the parameter in discussion for the cells defined as parallel to the stretching direction (Figure 5.3). Graph on the right hand-side shows the temporal change of the parameter in discussion for the cells defined as perpendicular to the stretching direction.

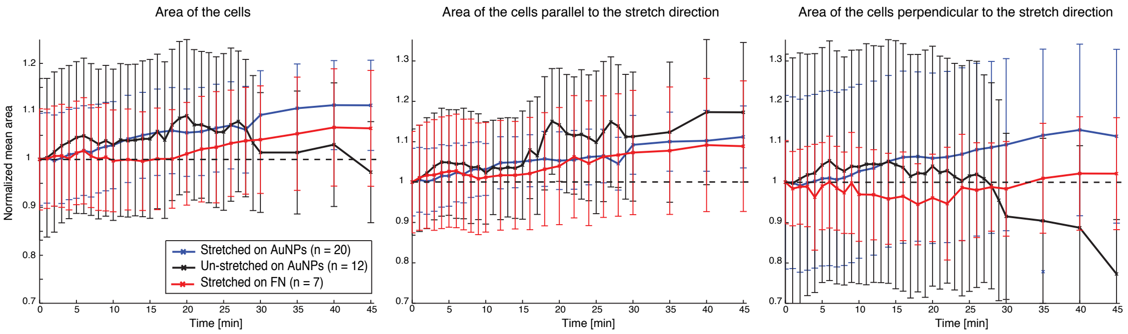

Figure 7.8: Normalized mean area of the cells subjected to uniaxial, static stretch. Blue line represents the temporal change of the mean normalized area of cells stretched on HGs + AuNPs + RGD. Black line represents the temporal change of the mean normalized area of cells seeded on HGs + AuNPs + RGD. Red line represents the temporal change of the mean normalized area of cells stretched on HGs + FN. Error bars refer to the standard error of the mean.

Temporal change of cells' normalized area (Figure 7.8): Comparison of the three conditions for cells both parallel and perpendicular to the stretch direction. The values of normalized mean area of un-stretched cells on HGs + AuNPs + RGD scatters quite randomly around the value of 1 as expected (initial conditions do not change). There is a slight increase in cells' normalized mean area for the cases of stretched cells on HGs + AuNPs + RGD (10 %) and on HGs + FN (5 %). Comparison of normalized mean area of cells parallel to the stretch direction vs. cells perpendicular to the stretch direction. Un-stretched cells parallel to the stretch direction grow a 15 % in area, whereas un-stretched cells perpendicular to the stretch direction reduce their area in 20 %. Both cells on HGs + AuNPs + RGD and on HGs + FN parallel to the stretch direction show an increase in normalized mean area (10 %). Area increase is higher for the cells on HGs + AuNPs + RGD perpendicular to the stretch direction (10 %) than for the cells on HGs + FN perpendicular to the stretch direction (values scatter around 1).

Temporal change of cells' area variation (Figure 7.9): Comparison of the three conditions for cells both parallel and perpendicular to the stretch direction. For the un-stretched cells on HGs + AuNPs + RGD there seems to be three 15 minutes phases where the cells present stadiums of increasing protrusion activity. However this increase in mean area variation is not so marked for the cases of stretched cells on HGs + AuNPs + RGD and on HGs

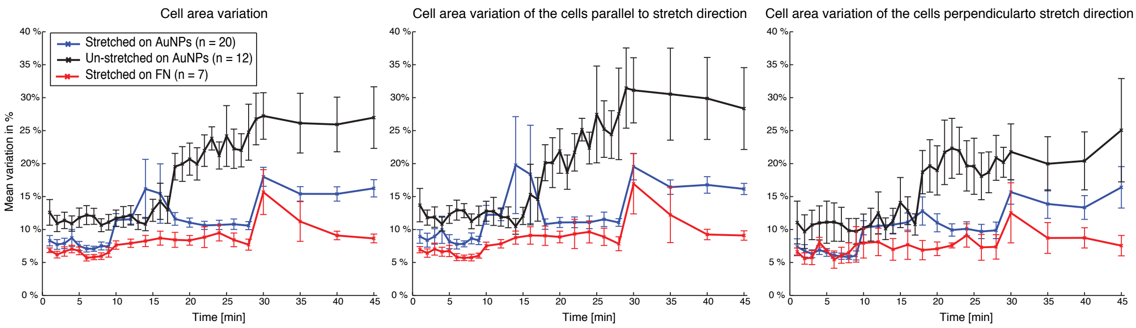

Figure 7.9: Mean area variation of the cells subjected to uniaxial, static stretch. Blue, black and red lines represent the same as in figure 7.8 but referred to the area variation of the cells. Error bars refer to the standard error of the mean.

+ FN. Nevertheless, cells stretched on HGs + AuNPs + RGD present higher variation values (ranging from 10 % to 17 %) than cells stretched on HGs + FN (ranging from 7 % to 13 %). Comparison of mean area variation of cells parallel to the stretch direction vs. cells perpendicular to the stretch direction cells. A small difference can be found between the values of the mean area variation of cells parallel to the stretch direction (ranging from 8 % to 18 %) with the values of the mean area variation of cells perpendicular to the stretch direction (ranging from 7 % to 13 %) on HGs + AuNPs + RGD. On HGs + FN there is no significant difference between cells parallel or perpendicular to the stretch direction.

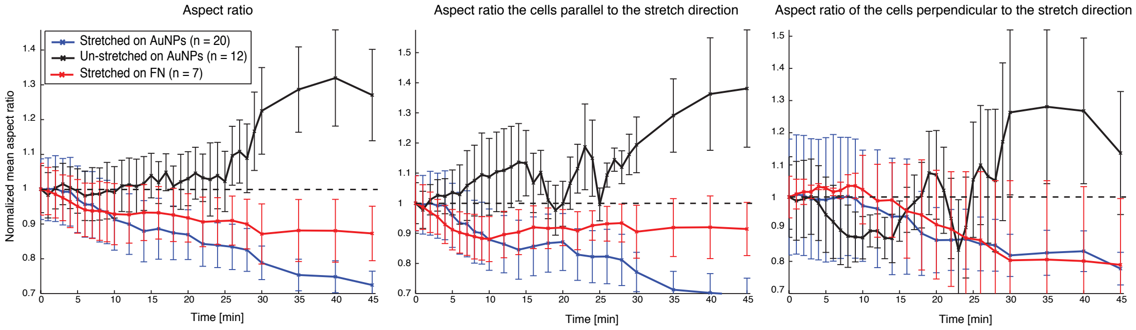

Figure 7.10: Normalized mean aspect ratio of the cells subjected to uniaxial, static stretch. Blue, black and red lines represent the same as in figure 7.8 but referred to the mean normalized aspect ratio of the cells. Error bars refer to the standard error of the mean.

Temporal change of cells' normalized aspect ratio (Figure 7.10): Comparison of the three conditions for cells both parallel and perpendicular to the stretch direction. Unstretched cells on HGs + AuNPs + RGD behave quite randomly during the first 30 minutes and apparently become much more elongated during the last 15 minutes. After visually checking the films it is confirmed that this behavior is due to cells with abrupt increases in aspect ratio (Figure 7.13). More importantly there is a marked decrease in normalized mean cells' aspect ratios for the cases of stretched cells on HGs + AuNPs + RGD (25 %) and on HGs + FN (10 %). Again, this effect comes from abrupt changes in cells' morphology. Comparison of normalized mean aspect ratio of cells parallel to the stretch direction vs. cells perpendicular to the stretch direction. Un-stretched cells on HGs + AuNPs + RGD behave randomly around the value of 1 for both classifications of cells. For cells parallel to the stretch direction cells get more elongated when stretched on HGs + AuNPs + RGD than on HGs + FN. For cells perpendicular to the stretch direction there's no apparent difference between being seeded on HGs + AuNPs + RGD or on HGs + FN but the trend is still clear downward.

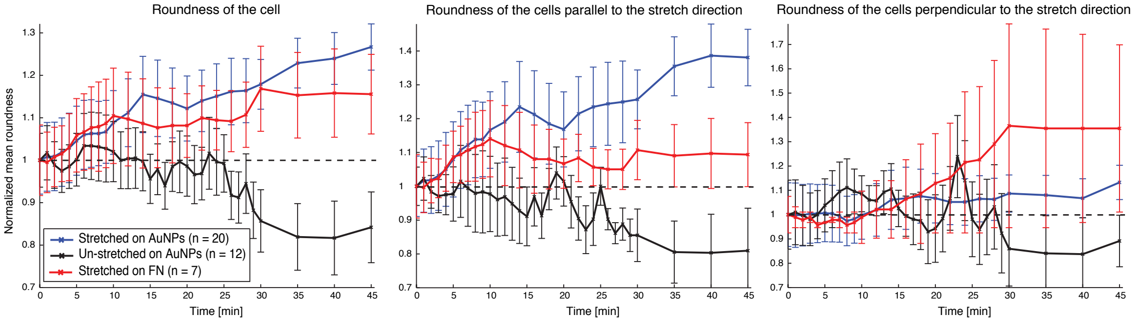

Figure 7.11: Normalized mean roundness of the cells subjected to uniaxial, static stretch. Blue, black and red lines represent the same as in figure 7.8 but referred to the normalized mean roundness of the cells. Error bars refer to the standard error of the mean.

Temporal change of cells' normalized roundness (Figure 7.11). Roundness can be defined as the inverse of the aspect ratio due to the presence of the major axis to the power of two in the denominator of its definition, so similar but inverted trends to the ones observed for the aspect ratio are expected (the more elongated a form the less round it is), which is indeed the case.

Temporal change of cells' normalized circularity (Figure 7.12). In some texts, circularity is also known as formfactor because it gives an idea of the ratio between perimeter and area of the object. In this work it can be assimilated to number of protrusions. Comparison of the three conditions for cells both parallel and perpendicular to the stretch direction: The normalized mean circularity of un-stretched cells on AuNPs scatters quite randomly around the value of 1 as expected. Normalized mean circularity of cells stretched on HGs + AuNPs + RGD show a rising trend (10 %) whereas those values for cells stretched on HGs + FN scatter quite randomly around the value of 1. Comparison of normalized mean circularity of cells parallel to the stretch direction vs. cells perpendicular to the stretch direction cells: For the case of cells parallel to the stretched direction the trends become clearer than when comparing all cells together: cells stretched on HGs + AuNPs + RGD see an increase in the normalized circularity values of around 20 % whereas those values for cells stretched on HGs + FN scatter quite randomly around the value of 1 similarly to

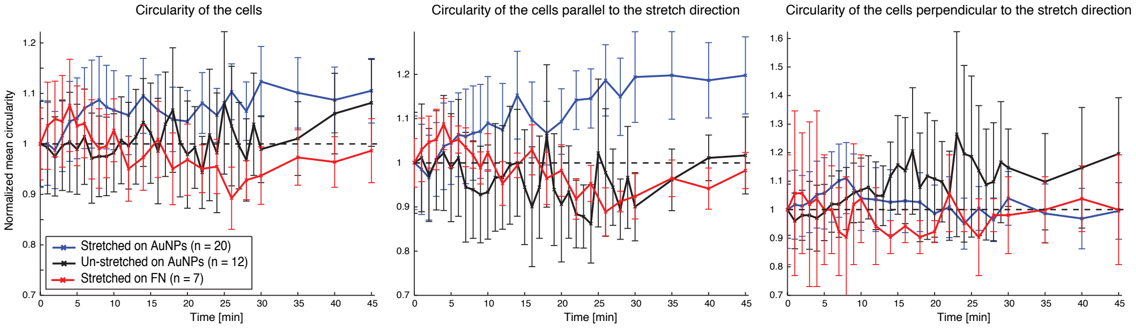

Figure 7.12: Normalized mean circularity of the cells subjected to uniaxial, static stretch. Blue, black and red lines represent the same as in figure 7.8 but referred to the normalized mean circularity of the cells. Error bars refer to the standard error of the mean.

the un-stretched cells on HGs + AuNPs + RGD. In the case of cells perpendicular to the stretch direction the values of normalized mean circularity scatter randomly around the value of 1 for the three conditions.

Overall, standard error of the mean bars are between 5 % to 15 % of the plotted values which is in the usual range for biological experiments. Nevertheless, in some cases are wider: Populations in every condition are rather small; the vertical limits of the y-axis on the plots were kept quite narrow around the minimal and maximal values plotted in order to display clearer the trends in the curves; some shape descriptors are prone to abrupt changes for small variations in the cells resulting in a broader distribution of the values (Figure 7.13); in some cases cells retract big portions of lamellipodia (affecting up to 50 % of cells area) resulting in substantive changes in the shape descriptors and in a broader distribution of the values; in order to allow percentage comparison across conditions where the magnitudes of the parameters are different the curves were normalized by the value of the initial conditions.

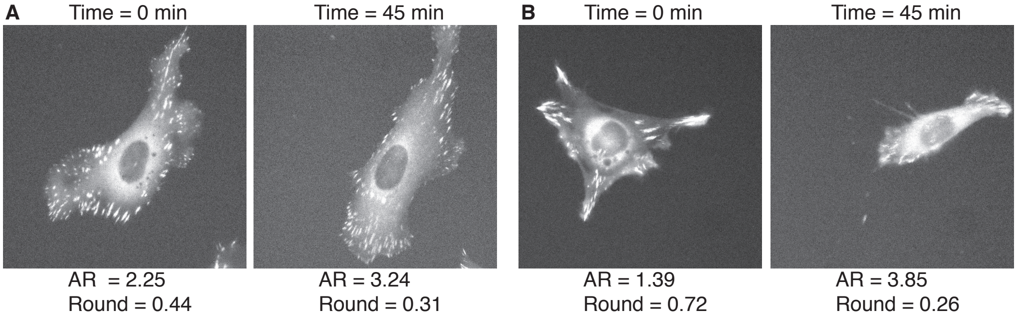

Figure 7.13: Example of changes in cells' shape descriptors. **(A)** Cell retracting a big lamellipodia in a time frame of 45 minutes and becoming a 44 % more elongated. **(B)** Cell retracting a big lamellipodia in a time frame of 45 minutes, becoming a 52 % smaller in area and a 270 % more elongated.

The differentiation between cells parallel and perpendicular to the stretch direction is made because a good correlation between the alignment of cell's outer polarized morphology and the internal cytoskeleton elements is expected, among them the actin network [Lauffenburger and Horwitz, 1996, Ridley et al., 2003]. It is also known that loads applied to the cell surface are preferentially borne by the cytoskeleton and that the transmission of the load relies on the linkage between the ECM and the cytoskeleton through integrin-mediated adhesions [Alenghat and Ingber, 2002]. Consequently a difference in the behavior of FAs of cells laying either parallel or perpendicular to the stretch direction may arise: actin bundles in the case of perpendicular cells will only get further separated whereas actin bundles in parallel cells will get co-stretched and the tension applied on the focal adhesions will increase.

In terms of the discrimination between large ($> 1\mu m^2$) and small ($< 1\mu m^2$) particles, the reasoning was to be able to quantify the newly formed focal contacts as a response to the increased strain. The segmentation of particles depending on their relative position to the cell's center of mass followed a similar reasoning to the parallel vs. perpendicular cells case. However, the drawback of this segmentation is manyfold: through such a stark segmentation the number of particles analyzed per segment is greatly reduced worsening the statistic relevance of the conclusions; the amount of generated graphs (two possible orientations of the cells, two possible size ranges for the particles and four possible segments relative to the center of mass makes a total of 16 graphs for each parameter analyzed) makes them difficult to be compared; the complexity of the code written in MatLab makes the whole processing more prone to errors [Merali, 2010]. Nevertheless, the self-written segmenting routine represents a first step towards an individualized tracking of the particles.

Taking all these trends together the following conclusions regarding the reaction of REF YFP-pax cells to an uniaxial, static strain of 13 % can be drawn:

1. Values of cells' area are too scattered to be able to make a definitive statement
2. Values of stretched cells' area variation are reduced in comparison to the un-stretched cells. However cells stretched on AuNPs show slightly higher values than cells stretched on FN. Similarly cells parallel to the stretch direction show slightly higher values than cells perpendicular to the stretch direction.
3. Values of cells' aspect ratio show decrease, more clearly for cells parallel to the stretch direction than for cells perpendicular direction and more prominent for cells on AuNPs than for cells on FN.
4. Values of cells' roundness follow similar but inverted trends to the values of cells' aspect ratio.
5. Values of cells' circularity (formfactor) show higher variations for the cells parallel to the stretch direction than for the cells perpendicular to the stretch direction and among these the highest values are for cells on AuNPs.

REF YFP-pax cells reacted to the strain with a decreased protrusion activity (area variation), an increased elongation and an increase in circularity (less protrusions). All these reactions were more prominent if cells laid parallel to the stretch direction and seeded on HGs + AuNPs + RGD. A factor accounting for this behavior could be the fact that along the stretching direction the ΔL between the AuNPs + RGD increases and so will do the integrin receptors in the cells membrane. At least temporally, there will be a decrease in ligand density along the stretching direction affecting the capacity of FAs to exert tension on the surface and the capacity of the cells to protrude or retract parts of their membrane. Due to the fact that actin network lays parallel to the strain, this effect will be more prominent for cells laying parallel to the stretching direction than for cells laying perpendicular to the stretch direction: the actin network will fail to pull from the temporally low-density FAs [Wehrle-Haller and Imhof, 2002] and the cell will be hindered in its ability to form a lamellipodium-lamellum interface (actin retrograde flow friction against FAs is crucial for the formation of such interface) [Shemesh et al., 2009]. Only after diffusion of the integrins in the cell's membrane to sites where RGD motifs lay at a more comfortable spacing (Figure 6.14) will the FAs recover their mechano-transductive capabilities (recovered protrusion activity after 25 minutes of the stretching shown in figure 7.9). Nevertheless, in order to be able to analyze significant changes in cell area and morphology, longer time periods of observation are required.

7.4 Analysis of FAs' temporal change in the stretched state

All figures of this section have the same organization: graph on the left hand side shows the temporal change of the parameter in discussion of the FAs belonging to cells both parallel and perpendicular to the stretch direction. Graph in the middle shows the temporal change of the parameter in discussion of the FAs belonging to cells defined as parallel to the stretching direction (Figure 5.3). Graph on the right hand side shows the temporal change of the parameter in discussion of the FAs belonging to cells defined as perpendicular to the stretching direction.

Temporal change of FAs' normalized mean area (Figure 7.14): Comparison of the three conditions for FAs belonging to cells both parallel and perpendicular to the stretch direction: The normalized mean area values of FAs un-stretched on HGs + AuNPs + RGD scatters initially around the value of 1 and then shows a decrease (20 %). The normalized mean area values of FAs stretched on HGs + AuNPs + RGD scatter quite randomly around the value of (initial conditions).The normalized mean area values of FAs stretched on HGs + FN show a rapid (within the first 5 minutes) decrease of a 10 % magnitude and remain at that size with some punctual variations (at the minute 30 there's an 8 % increase in area). Comparison of normalized mean area values of FAs belonging to cells parallel to the stretch direction vs. FAs belonging to cells perpendicular to the stretch direction: The normalized mean area values of FAs belonging to cells un-stretched on HGs + AuNPs + RGD scatters initially around the value of 1 and then shows a decrease (20 %). The normalized mean area values of FAs belonging to cells on HGs + AuNPs

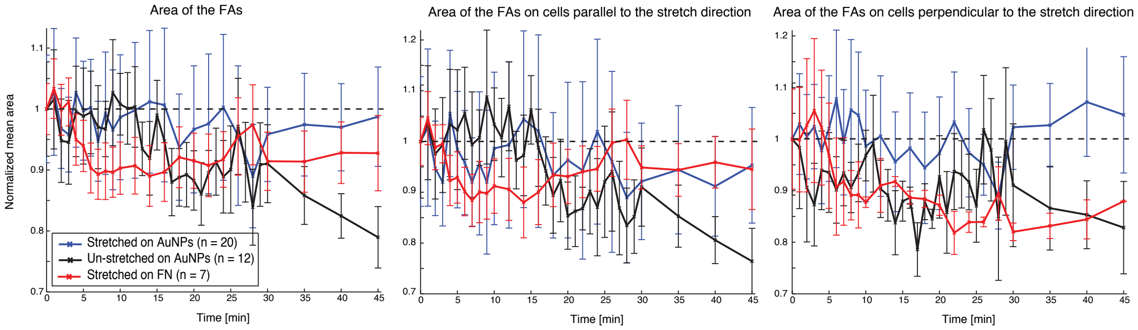

Figure 7.14: Normalized mean area of the FAs subjected to uniaxial, static stretch. Blue line represents the temporal change of the normalized mean area of the FAs belonging to cells stretched on HGs + AuNPs + RGD (on the following FAs un-stretched on HGs + AuNPs + RGD). Black line represents the temporal change of the normalized mean area of the FAs belonging to cells seeded on HGs + AuNPs + RGD (on the following FAs stretched on HGs + AuNPs + RGD). Red line represents the temporal change of the normalized mean area of the FAs belonging to cells stretched on HGs + FN (on the following FAs stretched on HGs + FN). Error bars refer to the standard error of the mean.

+ RGD and parallel to the stretch direction scatter quite randomly around the value of 1.The normalized mean area values of FAs belonging to cells on HGs + FN and parallel to the stretch direction show a rapid (within the first 5 minutes) decrease of a 10 % and then recover partially (5 %). The normalized mean area values values of FAs belonging to cells on HGs + AuNPs + RGD and perpendicular to the stretch direction scatter quite randomly around the value of 1. The normalized mean area values of FAs belonging to cells on HGs + FN and perpendicular to the stretch direction show a rapid (within the first 10 minutes) decrease of a 10 % and remain at that size or become even smaller (15 %) during the remaining observation.

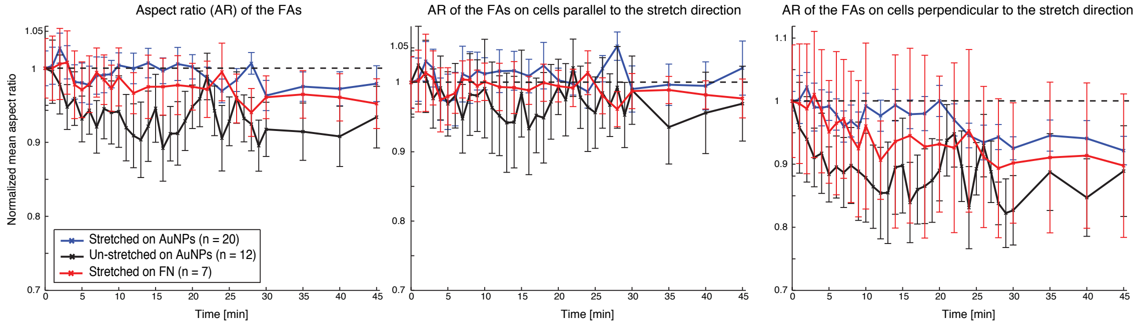

Figure 7.15: Normalized mean aspect ratio of the FAs subjected to uniaxial, static stretch. Blue, black and red lines represent the same as in figure 7.14 but referred to the normalized mean aspect ratio of the FAs. Error bars refer to the standard error of the mean.

Temporal change of FAs' normalized mean aspect ratio (Figure 7.15): Comparison of the three conditions for FAs belonging to cells both parallel and perpendicular to the stretch direction: The normalized mean area values of FAs for the three conditions scatter within an interval of ± 5 % around the value of 1. Only un-stretched FAs on HGs + AuNPs + RGD show a more significant decrease (9 %) interrupted in the minutes 20 to 30. Comparison of normalized mean aspect ratio of FAs belonging to cells parallel to the stretch direction vs. the values for FAs belonging to cells perpendicular to the stretch direction: The normalized mean area values of FAs belonging to cells parallel to the stretch direction scatter within an interval of ± 5 % around the value of 1 for the three conditions. The normalized mean area values of FAs belonging to cells on HGs + AuNPs + RGD perpendicular to the stretch direction show a decrease of 8 % and on HGs + FN of 10 %.

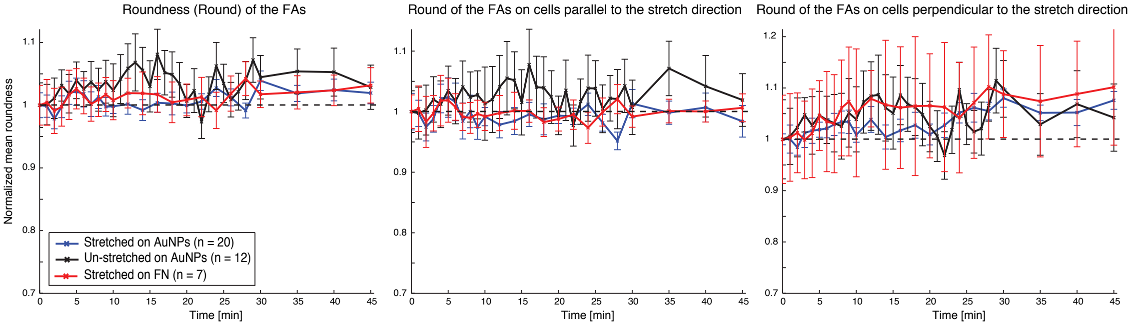

Figure 7.16: Normalized mean roundness of the FAs subjected to uniaxial, static stretch. Blue, black and red lines represent the same as in figure 7.14 but referred to the normalized mean roundness of the FAs. Error bars refer to the standard error of the mean.

Temporal change of FAs' normalized mean roundness (Figure 7.16). Roundness can be defined as the inverse of the aspect ratio due to the presence of the major axis to the power of two in the denominator of its definition, so similar but inverted trends are expected (the more elongated a form the less round it is), which is indeed the case.

Temporal change of FAs' normalized mean angle (Figure 7.17): Comparison of the three conditions for FAs belonging to cells both parallel and perpendicular to the stretch direction. The normalized mean angle values of FAs for the three conditions scatter within an interval of ± 5 % around the value of 1. Only FAs on HGs + FN show a single 10 % increase peak in minute 27. Comparison of normalized mean angle of FAs belonging to cells parallel to the stretch direction vs. the values for FAs belonging to cells perpendicular to the stretch direction. The normalized mean angle values of FAs belonging to cells on HGs + AuNPs + RGD parallel to the stretch direction and on un-stretched cells on HGs + AuNPs + RGD scatter within an interval of ± 5 % around the value of 1. However, for the case of FAs on HGs + FN belonging to cells parallel to the stretch direction there's a 10-15 % increase. The normalized mean area values of FAs belonging to cells perpendicular to the stretch direction scatter within an interval of ± 5 % around the value of 1 for the three conditions.

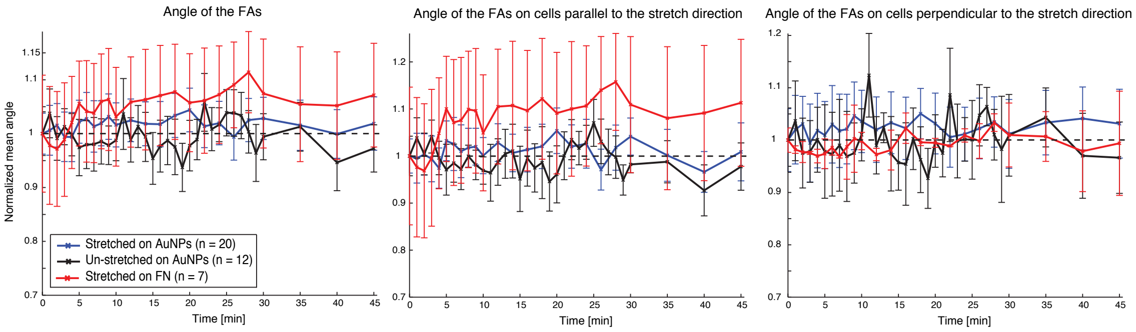

Figure 7.17: Normalized mean angle to stretch axis of the FAs subjected to uniaxial, static stretch. Blue, black and red lines represent the same as in figure 7.14 but referred to the normalized mean angle to stretch axis of the FAs. Error bars refer to the standard error of the mean.

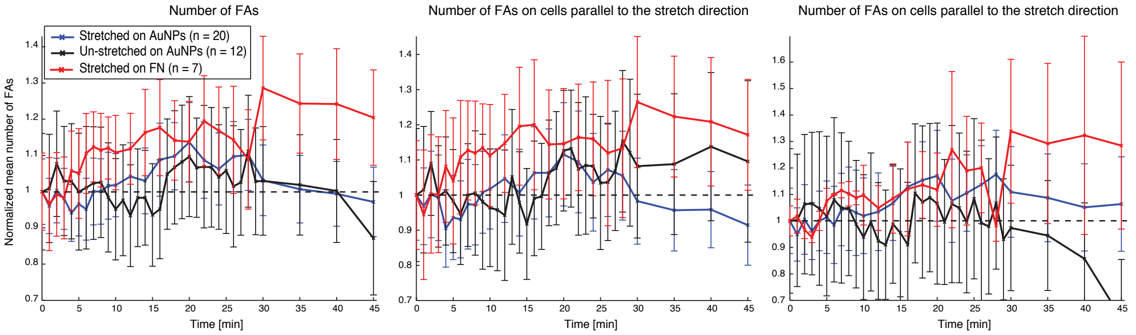

Figure 7.18: Normalized mean number of FAs subjected to uniaxial, static stretch. Blue, black and red lines represent the same as in figure 7.14 but referred to the normalized mean number of FAs. Error bars refer to the standard error of the mean.

Temporal change of FAs' normalized mean number of FAs (Figure 7.18): Comparison of the three conditions for FAs belonging to cells both parallel and perpendicular to the stretch direction. The normalized mean number of FAs belonging to cells stretched and un-stretched on AuNPs scatter within an interval of ± 10 % around the value of 1. The normalized mean number of FAs belonging to cells stretched on HGs + FN show an increase of up to 20 %. Comparison of normalized mean number of FAs belonging to cells parallel to the stretch direction vs. the values for FAs belonging to cells perpendicular to the stretch direction. The normalized mean number of FAs of un-stretched cells on HGs + AuNPs + RGD and of cells on HGs + AuNPs + RGD and parallel to the stretch direction scatter within an interval of ± 10 % around the value of 1. The normalized mean number of FAs of cells on HGs + FN and parallel to the stretch direction show an increase of up to 25 %. The normalized mean number of FAs of un-stretched cells on HGs + AuNPs + RGD show a decrease of a 30 %. The normalized mean number of FAs of cells on HGs + AuNPs + RGD and perpendicular to the stretch direction scatter within an interval of

± 10 % around the value of 1. The normalized mean number of FAs of cells on HGs + FN and perpendicular to the stretch direction show an increase of up to 30 %

Taking all these trends together the following conclusions regarding the reaction of REF YFP-pax cells' FAs to an uniaxial, static strain of 13 % can be drawn:

1. Values of FAs' normalized mean area belonging to un-stretched cells show a decrease, more prominently for cells parallel to the stretch direction. More importantly, whereas values of FAs' normalized mean area on AuNPs scatter around the value of 1, FAs on HGs + FN show a rapid decrease in normalized mean area more predominant in cells perpendicular to the stretch direction than in cells parallel to the stretch direction.
2. Values of FAs' normalized mean aspect ratio belonging to cells perpendicular to the stretch direction show a decrease more prominent in cells on HGs + FN than in cells on HGs + AuNPs + RGD.
3. Values of FAs' normalized mean roundness follow similar but inverted trends to the values of FAs' normalized mean aspect ratio.
4. Only values of FAs' normalized mean angle belonging to cells on HGs + FN and parallel to the stretch direction show an increase.
5. Values of normalized mean number of FAs' belonging to cells on HGs + FN parallel and perpendicular to the stretch direction show an increase.

The FAs of REF YFP-pax cells react to the strain with a decrease in normalized mean area and elongation when stretched on FN and laying perpendicular to the stretch direction and an increase in normalized mean number and angle when stretched on FN and laying parallel to the stretch direction. A reaction of the FAs is clearer when cells are stretched on the substrates where FN is presented to the cells rather than when only the RGD motif is presented. From the literature [Friedland et al., 2009] it is known that integrins and FN molecules interact at multiple sites (Figure 7.19).

The integrin-FN bond has been described in Friedland et al. [2009] to present two different states: relaxed or tensioned. The relaxed bonds involved only the RGD site, but the tensioned bonds required also the interaction of R1374 and R1379 at the synergy site of FN's domain 9. Hence it seems clear that RGD site promotes the recognition between integrins and FN (thereby invoking integrins to the focal contacts) whereas the synergistic sites make possible that the bond sustains an applied force. Notably, there was a reduction of 90 % in adhesion strength for the double R1374/1379A mutant. This could be a plausible explanation of the observed reaction of FAs when stretched on HGs + FN: the ability of the bond to transduce strength is of paramount importance for the FA to effectively act as mechano-sensor as this stimuli can be further transmitted intra-cellularly to downstream signaling cascades. Nevertheless, in order for this thesis to hold true, both the RGD recognition site and the synergistic sites at the FN molecule have to be available for the cell to contact them. FN on the HGs is bound through its

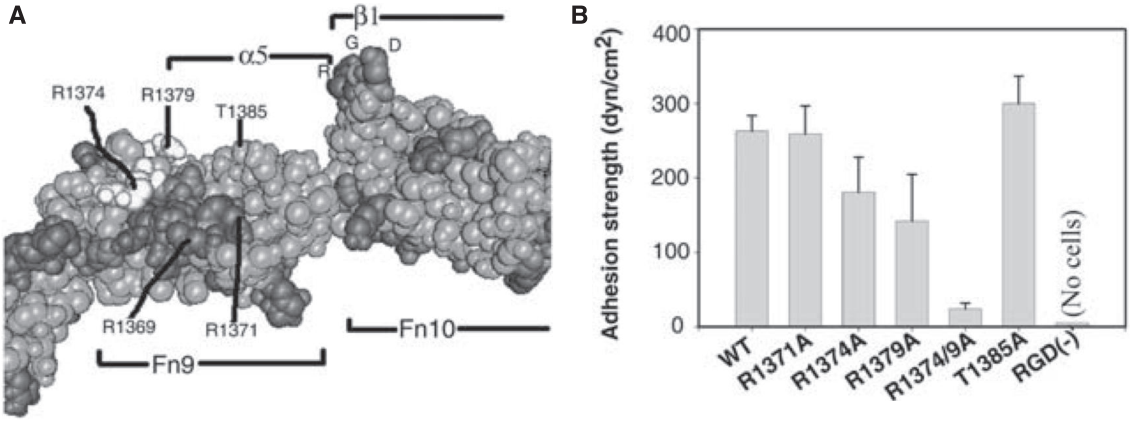

Figure 7.19: FN-Integrins synergistic sites interaction [Friedland et al., 2009]. **(A)** Domains 8 and 9 of the FN molecule. R1374 and R1379 at the domain 9 are responsible for the tensioned bonds whereas the RGD motif is a recognition site responsible for the relaxed bonds. **(B)** A double mutation of the R1374 and R1379 for Ala (R1374/1379A) produce a loss of 90 % adhesion strength, demonstrating their role as bond strength bearers.

amino terminus to the pre-existing carboxylic acid groups on the HGs' surface and its highly probable that it interacts with its hydrophilic parts with the hydrated PEG chains. Furthermore, cells were seeded on the HGs and allowed to adhere for 24h prior to the experiments, time during which FN fibrillogenesis could have taken place [Pompe et al., 2005]. An application of strain to the surface may then get partially transferred to the FN (as it may be forming fibers [Kaiser, 2009]) and reveal otherwise cryptic sites [Puklin-Faucher et al., 2006, Thomas et al., 2008, Vogel, 2006]. In this manner, by applying the strain to the HGs + FN the synergistic sites on the FN molecules may be revealed to the cells adhering to the surface and more complex signaling cascades maybe initiated.

Unfortunately the resolution of the microscopy techniques employed during this work does not allow a funded statement regarding which of the proposed biophysical models fits better the results obtained during this work.

Part IV

Conclusion and Outlook

Chapter

8

Nano-patterned, mechanotunable substrates

During this work elastic PEG-DA HGs were used as carrier substrate on which an array of AuNPs with well defined ΔL was immobilized. ΔL could be successfully varied at the nanometer scale by mechanical stretching of the carrier substrate. Furthermore, by rendering the setup bio-mimetic it could be used for cell adhesion studies with dynamic variation of inter-ligand distances.

8.1 Applicability of the setup

With the setup developed during this work, there was no risk of slipping events and through the dog-bone shape morphology the risk of ripping events was greatly reduced. AuNPs seem to stay in the HGs' surface even in the stretched state. Furthermore, thanks to the customized casting mold and the establishment of a simple stretching protocol, the technique can be easily implemented in a normally equipped chemical laboratory.

One of the most important conclusions of cell studies was that cells seeded in nano-patterned HGs with ΔLs around 58 nm and stretched a 15 % to a final 66 nm ΔL survive the combination of stimuli and live-cell imaging, at least during the period pictures were taken. More importantly, transmission of strain to cells and FAs is successful validating the engineered setup as the pertinent one to perform cell adhesion analysis under mechanical strain.

8.2 Temporal change of cells and of FAs response in the stretched state

Given that in the stretched-state, the ΔL between the AuNPs was below the published critical distance the response observed in cells and FAs was not expected to be a consequence of the disruption in the spreading capabilities of the cells but of the combination of the mechanical strain and the anisotropy generated in the hexagonal pattern of AuNPs.

REF YFP-Pax cells stretched on HGs + AuNPs + RGD showed a more prominent reaction when laying parallel to the stretch direction than laying perpendicular to the stretch direction. The generation of low-density FAs on which the actin network temporally fails to generate tension may account for some of the morphological observations. Nevertheless, in order to be able to analyze significant changes in cell area and morphology, longer time periods of observation are required. The FAs of REF YFP-Pax cells reacted more prominently when stretched on HGs + FN as when stretched on HGs + AuNPs + RGD. The potential revelation of the synergistic sites at FN molecules initiating more complex signaling cascades could account for some of the FAs observed variations.

8.3 Outlook

8.3.1 Further experimentation

Mechano-transduction

It could be shown in this work, how depending on the kind of biochemical signals, cells and their FAs react differently, tailoring their responses to the received input. Hence it seems clear that in our setup, where ligands lay fixed in the surface and the cells have no option to reorganize elements of the ECM, outside-in signaling plays a much more crucial role in the mechano-transductory capabilities of the FAs.

On the complementary role between integrins and their ligands. Catch bonds provide a physical mechanism for force sensing if different bond lifetimes correspond to different activation states that transduce distinct signals. Catch bonds may provide a mechanical mechanism for the cell to regulate adhesion by applying different forces at different times and locations when and where different adhesion strengths are desired [Kong et al., 2009]. In order for this to happen in our setup we would need a bio-functionalization of the AuNPs that would allow the catch-bond mechanism to occur, i.e. not only RGD motif but also the synergistic sites should be present (Figure 7.19).

FAs maturation

Can FAs become focal contacts through manipulation of the substrate cells are laying on? It has been published how cells growing on AuNPs arrays with 58 nm, 73 nm and 108 nm ΔLs show different adhesion behaviors. With this newly developed setup we can vary that ΔL dynamically from a start-point below the threshold distance and stretch them up to an extent where this threshold is overcome and then observe the dynamics of the process. Many questions arise: FAs will be receiving contradictory signals, i.e. an increase in tension that favors their assembly vs. a separation of the integrins up to a point where their signaling capabilities gets reduced and hence favoring their disassembly. Moreover, as shown in section 6.4.3 from the six particles in a hexagon surrounding the central one, only the two particles aligned with the central particle in the stretching direction will have an increased ΔL whereas the remaining four will not. It is therefore questionable whether the effect induced by the increased ΔLs between these two particles will outweigh the kept distance among the remaining four.

Discrimination between the effects of stretching

In order to isolate the effect of the increase in the lateral spacing between the biochemical signals from the the stress induced through the mechanical stimuli, a possibility would be to compare cells being stretched on a time scale where all biochemical actors have time to get reorganized (lateral spacing influence) with cells being rapidly stretched (stress influence). For that further experimentation would be needed to get a hint on the turnover ratios as well as on the K_{on} and K_{off} of such actors.

Co-signaling experiments by simultaneously presenting the cells with different ligands

Under the assumption that binary arrays consisting of AuNPs and nano-particles of other transition metal oxide (MOx) can be assembled simultaneously and in a controlled manner on a substrate, transferred to PEG-DA based systems and each type of particle functionalized selectively, co-signaling experiments under mechanical strain could be conducted (Zyxin or Syndecan-4).

Tuning properties of the HGs for specific applications

It is known from the literature that on stiff substrates, most $\alpha_5\beta_1$ integrin-FN bonds are in the tensioned state. However if cells were seeded on substrates in the stiffness range found in tissues (0.2 to 20 kPa) less resistance would be provided and the proportion of adhesive bonds in the relaxed state should increase. Since the proportion relaxed-tensioned state has been proposed to modulate cells mechano-transduction capabilities, by applying a strain to the substrates and monitoring cells response SCFS experiments could be conducted.

With the proposed substrates but with different ligand functionalization of the particles, other clustering effects could be explored. A clear example would be the formation of the immunological synapse.

Advanced microscopy techniques and image processing

In order to gain a clearer insight into the evolution of FAs in time, an image-processing tracking routine of FAs would be of great advantage. Combined with the powerful segmenting routines developed during this work, single FAs could be monitored and an analysis based on their size, localization or orientation with respect to the stretch direction performed. Additionally, by using microscopy techniques with higher resolution than fluorescent microscopy, FAs morphology variations could be thoroughly characterized. The results could then be used to proof the validity of the different biophysical models accounting for FAs mechano-sensing mechanism.

List of Figures

1.1 *In vivo* strain types and magnitudes 4
1.2 Progress in time of mechano-transduction 5
1.3 Mediators of mechanotransduction 6
1.4 FAs plaque layered architecture 7
1.5 Importance of the inter-ligand distance 9
1.6 FAs theoretical models 10

2.1 Outside-in cell signaling. 13
2.2 Block-copolymer micellar nano-lithography 17
2.3 UV-photopolymerization 19
2.4 RGD peptide mimetic 20
2.5 Peptide binding between carboxyl- and amino-groups 20
2.6 Fabrication of the substrates 22

3.1 Dip-coating 27
3.2 Transfer nano-lithography 28
3.3 Casting mold and stretching method decision tree 29

4.1 Rat Embryonic Fibroblasts eYFP-Pax stably transfected. 34
4.2 Stimuli unit 35
4.3 Experiment design 38

5.1 Visual description of the image processing performed with the ImageJ *iMacro* macro 41
5.2 Visual description of the ImageJ *iCalc* macro 42
5.3 Determination of cells angle to the stretch direction 43
5.4 Visual description of the ImageJ *iPixel* macro 43
5.5 Visual description of the MatLab *iMacro* macro 46

6.1 SEM characterization of the dip-coated surfaces 49
6.2 Characterization of the dip-coated surfaces 50

6.3 AFM characterization of the dip-coated surfaces 51
6.4 Characterization of the transfer nano-lithography 52
6.5 Swelling ratios of different HGs 53
6.6 Effect of inter-ligand distance on REF cells 53
6.7 Young's modulus of the PEG-10K-DA HGs 54
6.8 Potential stretching methods 55
6.9 Integrated meshes 57
6.10 Cast molds used in this work 58
6.11 Effect of the morphology of the HGs in their strain to stress response 59
6.12 Quantification of the applied strain and further observation of the stretched HGs 59
6.13 Customized casting equipment 60
6.14 Hypothesized anisotropy in the AuNPs' array 61
6.15 Theoretical anisotropy in the AuNPs' array 62

7.1 Area of the YFP-Pax REF cells seeded on different substrates 63
7.2 FAs of the YFP-Pax REF cells seeded on different substrates 64
7.3 Strain transmission to cells 65
7.4 Strain transmission to FAs 66
7.5 Quantification of the strain transmitted to the cells on the HGs. 67
7.6 Quantification of the strain transmitted to the FAs on the HGs. 68
7.7 Anisotropic FAs. 69
7.8 Normalized mean area of the cells subjected to uniaxial, static stretch . . . 70
7.9 Mean area variation of the cells subjected to uniaxial, static stretch. 71
7.10 Normalized mean aspect ratio of the cells subjected to uniaxial, static stretch 71
7.11 Normalized mean roundness of the cells subjected to uniaxial, static stretch. 72
7.12 Normalized mean circularity of the cells subjected to uniaxial, static stretch. 73
7.13 Example of changes in cells' shape descriptors. 73
7.14 Normalized mean area of the FAs subjected to uniaxial, static stretch. . . . 76
7.15 Normalized mean aspect ratio of the FAs subjected to uniaxial, static stretch. 76
7.16 Normalized mean roundness of the FAs subjected to uniaxial, static stretch. 77
7.17 Normalized mean angle to stretch axis of the FAs subjected to uniaxial, static stretch. 78
7.18 Normalized mean number of FAs subjected to uniaxial, static stretch. . . . 78
7.19 FN-Integrin bond. 80

A.1 ^{1}H-NMR spectrum obtained for PEG-DA. 107
A.2 Customized Visual Basic Applications Macro. 108
A.3 Autodesk Inventor Professional© strain analysis. 109
A.4 Normalized mean area of the FAs subjected to uniaxial, static stretch. . . . 110
A.5 Normalized mean aspect ratio of the FAs subjected to uniaxial, static stretch.110
A.6 Normalized mean roundness of the FAs subjected to uniaxial, static stretch. 111

A.7 Normalized mean angle to stretch axis of the FAs subjected to uniaxial, static stretch. 111
A.8 Normalized mean number of FAs subjected to uniaxial, static stretch. . . . 111

Bibliography

Francis J Alenghat and Donald E Ingber. Mechanotransduction: all signals point to cytoskeleton, matrix, and integrins. *Sci STKE*, 2002(119):pe6, Feb 2002. 3, 74

R D Allen, G B David, and G Nomarski. The zeiss-nomarski differential interference equipment for transmitted-light microscopy. *Z Wiss Mikrosk*, 69(4):193–221, Nov 1969. 36

K Anselme. Osteoblast adhesion on biomaterials. *Biomaterials*, 21(7):667–81, Apr 2000. 15

Antonietti, S Heinz, M Schmidt, and C Rosenauer. Determination of the micelle architecture of polystyrene/poly (4-vinylpyridine) block .... *Macromolecules*, Jan 1994. 17, 18

M Arnold, EA Cavalcanti-Adam, R Glass, J Blummel, W Eck, M Kantlehner, H Kessler, and JP Spatz. Activation of integrin function by nanopatterned adhesive interfaces. *ChemPhysChem*, 5(3), 2004. 8, 64

M Arnold, M Schwieder, J Blümmel, and E Cavalcanti-.... Cell interactions with hierarchically structured nano-patterned adhesive surfaces. *Soft Matter*, Jan 2009. 64

N Q Balaban, U S Schwarz, D Riveline, P Goichberg, G Tzur, I Sabanay, D Mahalu, S Safran, A Bershadsky, L Addadi, and B Geiger. Force and focal adhesion assembly: a close relationship studied using elastic micropatterned substrates. *Nat Cell Biol*, 3(5): 466–72, May 2001. 4, 6, 9

A Bershadsky, M Kozlov, and B Geiger. Adhesion-mediated mechanosensitivity: a time to experiment, and a time to theorize. *Current Opinion in Cell Biology*, 18(5):472–481, 2006. 8, 10

Alexander D Bershadsky, Nathalie Q Balaban, and Benjamin Geiger. Adhesion-dependent cell mechanosensitivity. *Annu Rev Cell Dev Biol*, 19:677–95, Jan 2003. 6

Achim Besser and Samuel A Safran. Force-induced adsorption and anisotropic growth of focal adhesions. *Biophysical Journal*, 90(10):3469–84, May 2006. 9

TD Brown. Techniques for mechanical stimulation of cells in vitro: a review. *J Biomech*, 33(1):3–14, 2000. 20, 21, 58, 65

Robijn Bruinsma. Theory of force regulation by nascent adhesion sites. *Biophysical journal*, 89(1):87–94, Jul 2005. 8

SJ Bryant, CR Nuttelman, and KS Anseth. Cytocompatibility of uv and visible light photoinitiating systems on cultured nih/3t3 fibroblasts in vitro. *Journal of Biomaterials Science, Polymer Edition*, 11(5):439–457, 2000. 28

EA Cavalcanti-Adam, T Volberg, A Micoulet, H Kessler, B Geiger, and JP Spatz. Cell spreading and focal adhesion dynamics are regulated by spacing of integrin ligands. *Biophysical journal*, 92(8):2964–2974, 2007. 8, 52, 63, 64

Sheryl Coombs, John G New, and Mark Nelson. Information-processing demands in electrosensory and mechanosensory lateral line systems. *J Physiol Paris*, 96(5-6):341–54, Jan 2002. 5

Lee Ann Cooper, Tang-Long Shen, and Jun-Lin Guan. Regulation of focal adhesion kinase by its amino-terminal domain through an autoinhibitory interaction. *Mol Cell Biol*, 23 (22):8030–41, Nov 2003. 7

Alex G F de Beer, E Ada Cavalcanti-Adam, Günter Majer, M Lopez-García, H Kessler, and Joachim P Spatz. Force-induced destabilization of focal adhesions at defined integrin spacings on nanostructured surfaces. *Phys. Rev. E*, 81(5 Pt 1):051914, May 2010. 52

CA DeForest, BD Polizzotti, and KS Anseth. Sequential click reactions for synthesizing and patterning three-dimensional cell microenvironments. *Nature Materials*, 2009. 15

Dennis E Discher, Paul Janmey, and Yu-Li Wang. Tissue cells feel and respond to the stiffness of their substrate. *Science*, 310(5751):1139–43, Nov 2005. 54

A Doyle, F Wang, K Matsumoto, and K Yamada. One-dimensional topography underlies three-dimensional fibrillar cell migration. *Journal of Cell Biology*, Jan 2009. 6

J Drury and D Mooney. Hydrogels for tissue engineering: scaffold design variables and applications. *Biomaterials*, Jan 2003. 14, 15

Adam J Engler, Shamik Sen, H Lee Sweeney, and Dennis E Discher. Matrix elasticity directs stem cell lineage specification. *Cell*, 126(4):677–89, Aug 2006. 4, 67

J Faix and R Grosse. Staying in shape with formins. *Developmental cell*, 10(6):693–706, 2006. 10

Xiaowu Fan, Lijun Lin, and Phillip B Messersmith. Cell fouling resistance of polymer brushes grafted from ti substrates by surface-initiated polymerization: effect of ethylene glycol side chain length. *Biomacromolecules*, 7(8):2443–8, Aug 2006. 15

Brigitte Forster, Dimitri Van De Ville, Jesse Berent, Daniel Sage, and Michael Unser. Complex wavelets for extended depth-of-field: a new method for the fusion of multichannel microscopy images. *Microsc Res Tech*, 65(1-2):33–42, Sep 2004. 40

S Förster and M Antonietti. Amphiphilic block copolymers in structure-controlled nanomaterial hybrids. *Advanced Materials*, Jan 1998. 16, 17

S Förster, M Zisenis, E Wenz, and M Antonietti. Micellization of strongly segregated block copolymers. *The Journal of Chemical Physics*, Jan 1996. 16, 17

Julie C Friedland, Mark H Lee, and David Boettiger. Mechanically activated integrin switch controls alpha5beta1 function. *Science*, 323(5914):642–4, Jan 2009. 79, 80

Z Gao and A Eisenberg. A model of micellization for block copolymers in solutions. *Macromolecules*, 26(26):7353–7360, 1993. 17

B Geiger, A Bershadsky, R Pankov, and K M Yamada. Transmembrane crosstalk between the extracellular matrix–cytoskeleton crosstalk. *Nat Rev Mol Cell Biol*, 2(11):793–805, Nov 2001. 6

B Geiger, JP Spatz, and AD Bershadsky. Environmental sensing through focal adhesions. 2009. 6

P G Gillespie and R G Walker. Molecular basis of mechanosensory transduction. *Nature*, 413(6852):194–202, Sep 2001. 5

F Gittes, B Mickey, J Nettleton, and J Howard. Flexural rigidity of microtubules and actin filaments measured from thermal fluctuations in shape. *J Cell Biol*, 120(4):923–34, Feb 1993. 10

R Glass, M Moller, and JP Spatz. Block copolymer micelle nanolithography. *Nanotechnology*, 14(10):1153–1160, 2003. 17, 26, 27

R Glass, M Arnold, EA Cavalcanti-Adam, J Blümmel, C Haferkemper, C Dodd, and JP Spatz. Block copolymer micelle nanolithography on non-conductive substrates. *New Journal of Physics*, 6:101, 2004. 17

M Glogauer, P Arora, G Yao, I Sokholov, J Ferrier, and C A McCulloch. Calcium ions and tyrosine phosphorylation interact coordinately with actin to regulate cytoprotective responses to stretching. *Journal of Cell Science*, 110 (Pt 1):11–21, Jan 1997. 7

W R Gombotz, G H Wang, T A Horbett, and A S Hoffman. Protein adsorption to poly(ethylene oxide) surfaces. *Journal of Biomedical Materials Research*, 25(12):1547–62, Dec 1991. 15

Z Grabarek and J Gergely. Zero-length crosslinking procedure with the use of active esters. *Anal Biochem*, 185(1):131–5, Feb 1990. 20, 31

S Graeter, J Huang, N Perschmann, and M Lopez-Garcia. Mimicking cellular environments by nanostructured soft interfaces. *Nano Lett*, Jan 2007. 13, 18, 27

HJ Hageman. Photoinitiators for free radical polymerization. *Progress in organic coatings*, 13(2):123–150, 1985. 28

Cornelia Hahn and Martin A Schwartz. Mechanotransduction in vascular physiology and atherogenesis. *Nat Rev Mol Cell Biol*, 10(1):53–62, Jan 2009. 4

Ronald S Harland and Robert K Prud'homme. Polyelectrolyte gels. pages 1–2, May 2009. 15

J Harris. Poly (ethylene glycol) chemistry: biotechnical and biomedical applications. *bcin.ca*, Jan 1992. 15

Ulrich Hersel, Claudia Dahmen, and Horst Kessler. Rgd modified polymers: biomaterials for stimulated cell adhesion and beyond. *Biomaterials*, 24(24):4385–415, Nov 2003. 8

V Hirschfeld-Warneken, M Arnold, and A Cavalcanti-Adam .... Cell adhesion and polarisation on molecularly defined spacing gradient surfaces of cyclic rgdfk .... *European journal of cell biology*, Jan 2008. 21

A Hoffman. Hydrogels for biomedical applications. *Annals of the New York Academy of Sciences*, Jan 2001. 15

N B Holland, Y Qiu, M Ruegsegger, and R E Marchant. Biomimetic engineering of non-adhesive glycocalyx-like surfaces using oligosaccharide surfactant polymers. *Nature*, 392 (6678):799–801, Apr 1998. 15

Troy A Hornberger, Dustin D Armstrong, Timothy J Koh, Thomas J Burkholder, and Karyn A Esser. Intracellular signaling specificity in response to uniaxial vs. multiaxial stretch: implications for mechanotransduction. *Am J Physiol, Cell Physiol*, 288(1): C185–94, Jan 2005. 69

Richard O Hynes. Integrins: bidirectional, allosteric signaling machines. *Cell*, 110(6): 673–87, Sep 2002. 6

D Ingber. Integrins as mechanochemical transducers. *Curr Opin Cell Biol*, 3(5):841–8, Oct 1991. 6

D E Ingber. Cellular tensegrity: defining new rules of biological design that govern the cytoskeleton. *J Cell Sci*, 104 (Pt 3):613–27, Mar 1993. 5

D E Ingber. The mechanochemical basis of cell and tissue regulation. *Mech Chem Biosyst*, 1(1):53–68, Mar 2004. 3

Donald E Ingber. Cellular mechanotransduction: putting all the pieces together again. *FASEB J*, 20(7):811–27, May 2006. 4, 5, 6

M Iza, G Stoianovici, L Viora, and J Grossiord. Hydrogels of poly (ethylene glycol): mechanical characterization and release of a model drug. *Journal of Controlled Release*, Jan 1998. 26

Diana E Jaalouk and Jan Lammerding. Mechanotransduction gone awry. *Nat Rev Mol Cell Biol*, 10(1):63–73, Jan 2009. 4

S Jungbauer, H Gao, JP Spatz, and R Kemkemer. Two characteristic regimes in frequency-dependent dynamic reorientation of fibroblasts on cyclically stretched substrates. *Biophysical Journal*, 95(7):3470–3478, 2008. 65

Peter Kaiser. Fabrication of protein nanofibrils. *Dissertation*, pages 1–129, Oct 2009. 80

Pakorn Kanchanawong, Gleb Shtengel, Ana M Pasapera, Ericka B Ramko, Michael W Davidson, Harald F Hess, and Clare M Waterman. Nanoscale architecture of integrin-based cell adhesions. *Nature*, 468(7323):580–584, Nov 2010. 6, 7, 69

H Kessler. Conformation and biological activity of cyclic peptides. *Angewandte Chemie International Edition in ...* . 8

Fang Kong, Andrés J García, A Paul Mould, Martin J Humphries, and Cheng Zhu. Demonstration of catch bonds between an integrin and its ligand. *J Cell Biol*, 185(7):1275–84, Jun 2009. 7, 84

DR Kovar. Molecular details of formin-mediated actin assembly. *Current Opinion in Cell Biology*, 18(1):11–17, 2006. 10

S Krishnamoorthy, C Hinderling, and H Heinzelmann. Nanoscale patterning with block copolymers. *Materials Today*, Jan 2006a. 17

S Krishnamoorthy, R Pugin, J Brugger, H Heinzelmann, and C Hinderling. Tuning the dimensions and periodicities of nanostructures starting from the same polystyrene-block-poly(2-vinylpyridine) diblock copolymer. *Adv. Funct. Mater.*, 16(11):1469–1475, Jul 2006b. 17

Peter Krsko and Matthew Libera. Biointeractive hydrogels. *Materials Today*, Jan 2005. 16

E Langelier, D Rancourt, S Bouchard, and C Lord. Cyclic traction machine for long-term culture of fibroblast-populated collagen gels. *Annals of biomedical engineering*, Jan 1999. 21

D A Lauffenburger and A F Horwitz. Cell migration: a physically integrated molecular process. *Cell*, 84(3):359–69, Feb 1996. 6, 74

KY Lee and DJ Mooney. Hydrogels for tissue engineering. *Chem. Rev*, 101(7):1869–1880, 2001. 14

T Lee and RS Lakes. Anisotropic polyurethane foam with poisson'sratio greater than 1. *Journal of materials science*, 32(9):2397–2401, 1997. 69

H Lin, T Kai, BD Freeman, S Kalakkunnath, and DS Kalikas. The effect of cross-linking on gas permeability in cross-linked poly (ethylene glycol diacrylate). *Macromolecules*, 38(20):8381–8393, 2005. 26

Ilia Louban. Mimicking cellular environments. *Dissertation*, pages 1–131, Aug 2009. 54, 55

M Lutolf and J Hubbell. Synthesis and physicochemical characterization of end-linked poly (ethylene glycol)-co-peptide . . . . *Biomacromolecules*, Jan 2003. 15

M P Lutolf and J A Hubbell. Synthetic biomaterials as instructive extracellular microenvironments for morphogenesis in tissue engineering. *Nature Biotechnology*, 23(1):47–55, Jan 2005. 14

J Meiners, A Quintel-Ritzi, J Mlynek, and H Elbs. Adsorption of block-copolymer micelles from a selective solvent. *Macromolecules*, Jan 1997. 17

Zeeya Merali. Computational science: ...error. *Nature*, 467(7317):775–7, Oct 2010. 74

E W Merrill. Distinctions and correspondences among surfaces contacting blood. *Annals of the New York Academy of Sciences*, 516:196–203, Jan 1987. 15

Simon W Moore, Pere Roca-Cusachs, and Michael P Sheetz. Stretchy proteins on stretchy substrates: the important elements of integrin-mediated rigidity sensing. *Dev Cell*, 19 (2):194–206, Aug 2010. 6

D Murphy. Fundamentals of light microscopy and electronic imaging. *books.google.com*, Jan 2001. 37

A Nicolas and S Safran. Limitation of cell adhesion by the elasticity of the extracellular matrix. *Biophysical Journal*, Jan 2006. 9

A Nicolas, B Geiger, and SA Safran. Cell mechanosensitivity controls the anisotropy of focal adhesions. *Proceedings of the National Academy of Sciences*, 101(34):12520–12525, 2004. 9

E Ostuni, R Chapman, R Holmlin, and S Takayama. . . . A survey of structure‚àí property relationships of surfaces that resist the adsorption of protein. *Langmuir*, Jan 2001. 15

Ekaterina Papusheva and Carl-Philipp Heisenberg. Spatial organization of adhesion: force-dependent regulation and function in tissue morphogenesis. *The EMBO Journal*, Jan 2010. 6

RJ Pelham and Y Wang. Cell locomotion and focal adhesions are regulated by substrate flexibility. *Proc Natl Acad Sci USA*, 94(25):13661, 1997. 4, 7

M Pfaff, K Tangemann, B Muller, M Gurrath, G Muller, H Kessler, R Timpl, and J Engel. Selective recognition of cyclic rgd peptides of nmr defined conformation by alpha iib beta 3, alpha v beta 3, and alpha 5 beta 1 integrins. *Journal of Biological Chemistry*, 269 (32):20233–20238, 1994. 8, 53

M D Pierschbacher and E Ruoslahti. Cell attachment activity of fibronectin can be duplicated by small synthetic fragments of the molecule. *Nature*, 309(5963):30–3, Jan 1984. 8

M Pluta. Nomarski's dic microscopy: a review. *Proceedings of SPIE*, 10(1994):1994, 1846. 36

T Pompe, L Renner, and C Werner. Nanoscale features of fibronectin fibrillogenesis depend on protein-substrate interaction and cytoskeleton structure. *Biophysical Journal*, 88(1): 527–534, 2005. 64, 80

Eileen Puklin-Faucher, Mu Gao, Klaus Schulten, and Viola Vogel. How the headpiece hinge angle is opened: New insights into the dynamics of integrin activation. *J Cell Biol*, 175(2):349–60, Oct 2006. 80

E Rabani, D Reichman, P Geissler, and L Brus .... Drying-mediated self-assembly of nanoparticles. *Nature*, Jan 2003. 18

G Raeber, M Lutolf, and J Hubbell. Molecularly engineered peg hydrogels: a novel model system for proteolytically mediated cell .... *Biophysical Journal*, Jan 2005. 58

GP Raeber, J Mayer, and JA Hubbell. Part i: A novel in-vitro system for simultaneous mechanical stimulation and time-lapse microscopy in 3d. *Biomech Model Mechanobiol*, 7(3):203–214, 2008. 56, 58

Anne J Ridley, Martin A Schwartz, Keith Burridge, Richard A Firtel, Mark H Ginsberg, Gary Borisy, J Thomas Parsons, and Alan Rick Horwitz. Cell migration: integrating signals from front to back. *Science*, 302(5651):1704–9, Dec 2003. 74

Armando Del Rio, Raul Perez-Jimenez, Ruchuan Liu, Pere Roca-Cusachs, Julio M Fernandez, and Michael P Sheetz. Stretching single talin rod molecules activates vinculin binding. *Science*, 323(5914):638–41, Jan 2009. 7

D Riveline, E Zamir, N Q Balaban, U S Schwarz, T Ishizaki, S Narumiya, Z Kam, B Geiger, and A D Bershadsky. Focal contacts as mechanosensors: externally applied local mechanical force induces growth of focal contacts by an mdia1-dependent and rock-independent mechanism. *J Cell Biol*, 153(6):1175–86, Jun 2001. 6

Yasuhiro Sawada and Michael P Sheetz. Force transduction by triton cytoskeletons. *J Cell Biol*, 156(4):609–15, Feb 2002. 4

Ian C Schneider, Cristen K Hays, and Clare M Waterman. Epidermal growth factor-induced contraction regulates paxillin phosphorylation to temporally separate traction generation from de-adhesion. *Mol Biol Cell*, 20(13):3155–67, Jul 2009. 69

Martin A Schwartz. Cell biology. the force is with us. *Science*, 323(5914):588–9, Jan 2009. 4

US Schwarz and IB Bischofs. Physical determinants of cell organization in soft media. *Medical Engineering and Physics*, 27(9):763–772, 2005. 4

D Schwendel, R Dahint, S Herrwerth, M Schloerholz, W Eck, and M Grunze. Temperature dependence of the protein resistance of poly-and oligo (ethylene glycol)-terminated alkanethiolate monolayers. *Langmuir*, 17(19):5717–5720, 2001. 15

Sandra J Shefelbine, Peter Augat, Lutz Claes, and Ulrich Simon. Trabecular bone fracture healing simulation with finite element analysis and fuzzy logic. *J Biomech*, 38(12):2440–50, Dec 2005. 3, 4, 21

T Shemesh, B Geiger, AD Bershadsky, and MM Kozlov. Focal adhesions as mechanosensors: a physical mechanism. *Proceedings of the National Academy of Sciences*, 102(35): 12383–12388, 2005. 10

Tom Shemesh, Alexander B Verkhovsky, Tatyana M Svitkina, Alexander D Bershadsky, and Michael M Kozlov. Role of focal adhesions and mechanical stresses in the formation and progression of the lamellipodium-lamellum interface [corrected]. *Biophysical journal*, 97(5):1254–64, Sep 2009. 75

JP Spatz, A Roescher, S Sheiko, G Krausch, and M Möller. Noble metal loaded block lonomers: micelle organization, adsorption of free chains and formation of thin films**. *Advanced Materials*, 7(8):731–735, 1995. 17

JP Spatz, S Sheiko, and M Moller. Substrate-induced lateral micro-phase separation of a diblock copolymer the authors especially thank dr. g. krausch for helpful discussions. this work was supported by the deutsche forschungsgemeinschaft (sfb 239). *Advanced Materials*, 8(6), 1996a. 17

JP Spatz, S Sheiko, and M Möller. Ion-stabilized block copolymer micelles: Film formation and intermicellar interaction. *Macromolecules*, 29(9):3220–3226, 1996b. 17

Sergei Sukharev and David P Corey. Mechanosensitive channels: multiplicity of families and gating paradigms. *Sci STKE*, 2004(219):re4, Feb 2004. 7

Wendy E Thomas, Viola Vogel, and Evgeni Sokurenko. Biophysics of catch bonds. *Annual review of biophysics*, 37:399–416, Jan 2008. 80

Ashkan Vaziri and Arvind Gopinath. Cell and biomolecular mechanics in silico. *Nature Materials*, 7(1):15–23, Jan 2008. 69

Miguel Vicente-Manzanares, Donna J Webb, and A Rick Horwitz. Cell migration at a glance. *Journal of Cell Science*, 118(Pt 21):4917–9, Nov 2005. 6

Viola Vogel. Mechanotransduction involving multimodular proteins: converting force into biochemical signals. *Annu Rev Biophys Biomol Struct*, 35:459–88, Jan 2006. 5, 7, 8, 64, 80

JHC Wang and BP Thampatty. An introductory review of cell mechanobiology. *Biomechanics and modeling in mechanobiology*, 5(1):1–16, 2006. 3, 4, 58, 65

AW Watkins and KS Anseth. Investigation of molecular transport and distributions in poly (ethylene glycol) hydrogels with confocal laser scanning microscopy. *Macromolecules*, 38(4):1326–1334, 2005. 16

Bernhard Wehrle-Haller and Beat Imhof. The inner lives of focal adhesions. *Trends Cell Biol*, 12(8):382–9, Aug 2002. 64, 75

H Wolfenson, Y Henis, B Geiger, and A Bershadsky. The heel and toe of the cell's foot: A multifaceted approach for understanding the structure and dynamics of focal adhesions. *Cell motility and the cytoskeleton*, Jul 2009. 6

JY Wong, A Velasco, P Rajagopalan, and Q Pham. Directed movement of vascular smooth muscle cells on gradient-compliant hydrogels,Ä†. *Langmuir*, 19(5):1908–1913, 2003. 52

T Yeung, PC Georges, LA Flanagan, B Marg, M Ortiz, M Funaki, N Zahir, W Ming, V Weaver, and PA Janmey. Effects of substrate stiffness on cell morphology, cytoskeletal structure, and adhesion. *Cell motility and the cytoskeleton*, 60(1):24–34, 2005. 4

Ronen Zaidel-Bar, Shalev Itzkovitz, Avi Ma'ayan, Ravi Iyengar, and Benjamin Geiger. Functional atlas of the integrin adhesome. *Nat Cell Biol*, 9(8):858–67, Aug 2007. 6

E Zamir, B Z Katz, S Aota, K M Yamada, B Geiger, and Z Kam. Molecular diversity of cell-matrix adhesions. *Journal of Cell Science*, 112 (Pt 11):1655–69, Jun 1999. 64

Stefano Zanini, Claudia Riccardi, Elisa Grimoldi, Claudia Colombo, Anna Maria Villa, Antonino Natalello, Pietro Gatti-Lafranconi, Marina Lotti, and Silvia Maria Doglia. Plasma-induced graft-polymerization of polyethylene glycol acrylate on polypropylene films: chemical characterization and evaluation of the protein adsorption. *J Colloid Interface Sci*, 341(1):53–8, Jan 2010. 15

A Zemel, F Rehfeldt, A E X Brown, D E Discher, and S A Safran. Optimal matrix rigidity for stress-fibre polarization in stem cells. *Nature Physics*, 6(6):468–473, Mar 2010. 54

Junmin Zhu, Chad Tang, Kandice Kottke-Marchant, and Roger E Marchant. Design and synthesis of biomimetic hydrogel scaffolds with controlled organization of cyclic rgd peptides. *Bioconjug Chem*, 20(2):333–9, Feb 2009. 15

Acknowledgements

First and foremost, I would like to express my deepest gratitude to Professor Joachim Spatz for giving me the thrilling opportunity of pursuing my PhD in his research group investigating in a very demanded field. I could learn a great deal about interdisciplinary techniques and to collaborate with different kinds of people and cultures. I will never forget the lessons I gathered during my thesis. Also I value his academic support and his scientific vision. Finally I am very grateful for being able to obtain my MBA degree at IE business school simultaneously with my thesis.

To Ralf Kemkemer for his precious time and the visionary supervision of my thesis. For the jokes and the laughs. For the support and the help. For his patience during the first months of my thesis when my german was far from understandable. For his sincere wish that his students become valuable professionals. For the sailing.

To Alexandra Goldyn and Sarah Biela for the ”Feierabendbier” helping me disconnect from the MBA and injecting in me great doses of wisdom, organizational ”savoir faire” and resistance that contributed to me seeing the end of my PhD. Specially to Alex for introducing me in the basics of cell culture and microscopy. I enjoyed our mutual collaboration in the lab that lead to a published paper. To Dr. Simon Jungbauer for introducing me in the field of substrate stretching and for those swäbische lunches with Dr. Christian Greiner in the very beginning where I could barely understand a word. They were a nice mental break from the daily routine. To Marc Gronle for his amazing VBA macro. For his caring interest. To Martin Deibler for helping me discover the rich world of computer programming. For helping me fight my data. For his vast expertise in the lab. For the climbing.

Very special thanks go to my 4-years office mates, Claudio Rolli and Melih Kalafat. For knowing how to share many good moments but more important, all those valleys one goes through during a PhD thesis. Specially to Claudio for accompanying me many days on my way to work and for rescuing me often from the depths of the MBA nights. For MatLab discussions and general support. To Melih for the funniest holidays we spent in Spain and his efforts trying to learn spanish and to teach me turkish. Also to Jovana Matic, for her peculiar sense of humor and her quiet company at later hours.

To Wylie Ahmed for fruitful discussions in the lab, for insightful ideas and of course for all the beers and the fun we shared. Thanks for rescuing me from the depths of the MBA nights.

To Dr. Roberto Fiammengo for his chemical expertise and his kind words and support. Very special thanks to Dr. Ilia Louban for his know-how with the hydrogels, the cryo SEM and the AFM and for his positive spirit and the fun we shared behind beer glasses. To Dr. Nadine Perschmann and Dr. Nicole Rauch for showing me the technique of UV-curing.

I also want to thank all the students I supervised during my PhD. I only hope they could learn from me at the least half of the great deal I could learn from them. In special to Britta Striegl for her hard work at the lab and her always valuable input. To Jenny Diemer for her caring patience and her commitment. To Yi Su and Wylie Ahmed for those initial incursions in the AFM. To Tanmay Pradhan for his quick mind and interesting discussions.

To the AK Spatz, for sharing the know-how and providing tips and critics. Specially to Sebastian Kruss for fruitful discussions, interesting papers, complicity suffering the sometimes twisted ways of programming and for his acid sense of humor. To Simon Ulrich for his loud laughter and his company swimming. Of course to our greek expert Ioannis Grigoridis for his SEM lessons, his mediterranean spirit and all our political discussions. To Henriette Ries for helping me order stuff and for her expertise in the lab. To Christine Mollenhauer for her incredible spirit, her help in the lab with the FN and all the laughs and interesting stories about her time in the USA. To Maria Sycha and Margit Kipp for her dipping expertise. To the lunch team for countless stories and laughs. To the workshops for their magnificent work with the molds and the clamps.

A mi Familia. A mis padres por el apoyo y la fe depositadas en mi persona a la hora de proporcionarme una educación increíble. Por levantarme en tantas ocasiones como caí. Por inculcarme los valores de perseverancia, austeridad y respeto que tantas veces me han ayudado durante estos cuatro años a superar días, semanas e incluso meses de oscuridad. A mis hermanos y cónyuges por sus continuas muestras de apoyo y ánimo. En especial a Gonzalo y Ángela por alojarme en su casa en Tübingen y por todas las ensaladas, cervezas y piñas compartidas. A mis sobrinos por ser una explosión de luz y felicidad que me remontan a mi feliz infancia. A José Félix por su Amistad con mayúscula. Por creer en mí, por escuchar mis quejas y aliviar mi carga compartiéndola.

To Alice... For every day we've been together. For her optimism and the constant smile in her face. For her unbreakable support during these last months often with short nights, long weeks and all the accompanying sacrifices. For her incisive input.

To Dr. Ralf Kemkemer, Alice Schwede and Dr. Roberto Fiammengo for reading this manuscript and helping my shape the definitive version. Specially to Ralf for reminding me how you can't see the forest through the trees.

Me gustaría dedicar unas líneas a mi tía Pilar Sanz, que se fue de nuestro lado el 22.12.2010 dejando un vacío grande en nuestras vidas. El sentido recuerdo de su persona me acompañará toda mi vida.

Appendix

Appendix

A

Appendix

A.1 Abbreviations

AuNPs Gold Nano-Particles

BCMN Block Copolymer Micellar Nano-lithography

CofM Center of Mass

DIC Differential Interference Contrast

ECM Extra Cellular Matrix

EDTA 1-Ethyl-3-(3-dimethylaminopropyl)carbodiimide

EDAC Ethylendiaminetetraacetate

FAs Focal Adhesions

FBS Fetal Bovine Serum

FN Fibronectin

HGs Hydrogels

DIC Normarski Interference Contrast

PBS Phosphate Buffered Saline

PEG-DA Poly(Ethylene Glycol)-Diacrylate

PS Poly(styrene)

P2VP Poly(2-vinylpiridine)

REF Rat Embryonic Fibroblast

RGD arginine (R), glycine (G) and aspartate (D)

SEM Scanning Electron Microscope

SPM Scanning Probe Microscope

THF Tetrahydrofuran

UV Ultraviolet

YFP Yellow Fluorescent Protein

A.2 ^{1}H-NMR-Characterization of PEG-DA modification

The degree of modification of the PEG chains' OH-terminus with acrylate moieties is of great importance because it determines the cross-linking density of the cured HGs, factor from which depends to a great extent the integrity of the substrates and their elastic behavior. For this reason a ^{1}H-NMR analysis of the final product was performed (Dr. Roberto Fiammengo). As shown in figure A.1 and in equation A.1, 85 % of the end groups were successfully modified to acrylate.

$$\begin{gathered}
\frac{10{,}000\ [g/mol]}{44\ [g/mol]} = 227\ Ethylene\ units \\
227\ Ethylene\ units \cdot 4 = 908\ H6\ atoms \\
\frac{908\ H6\ atoms}{2\ Spectrum\ reference} = 454\ H6\ atoms\ referenced \\
\frac{454\ integrated\ H6\ atoms}{532.82\ H6\ atoms\ referenced} = 85\%\ acrylated\ end\ groups
\end{gathered} \tag{A.1}$$

To obtain the degree of modification of the PEG chains' OH-terminus with acrylate moieties calculated the number of ethylene units that there is per PEG chain was multiplied by the Hydrogen atoms at the position indexed as 6 and referenced it to the integration curve of the spectrum (reflects the abundance of the individual protons). That number represents how many H6 atoms are in a PEG-DA electronic environment. Dividing the total number of H6 atoms (sum of atoms that are in a PEG and in a PEG-DA electronic environment) per that figure the percentage of PEG chains that have been modified to PEG-DA could be calculated.

A.3 Customized VBA macro

Figure A.2 presents the interface of the VBA program (Marc Gronle). The program allows the simultaneous control of Zeiss Axiovision and Physik Instrumente softwares enabling us to synchronize the actions of the microscope and the motors actuating on the PEG-DA HGs. As a result, we could design at our ease the single steps along our experiments in a drag-and-drop way.

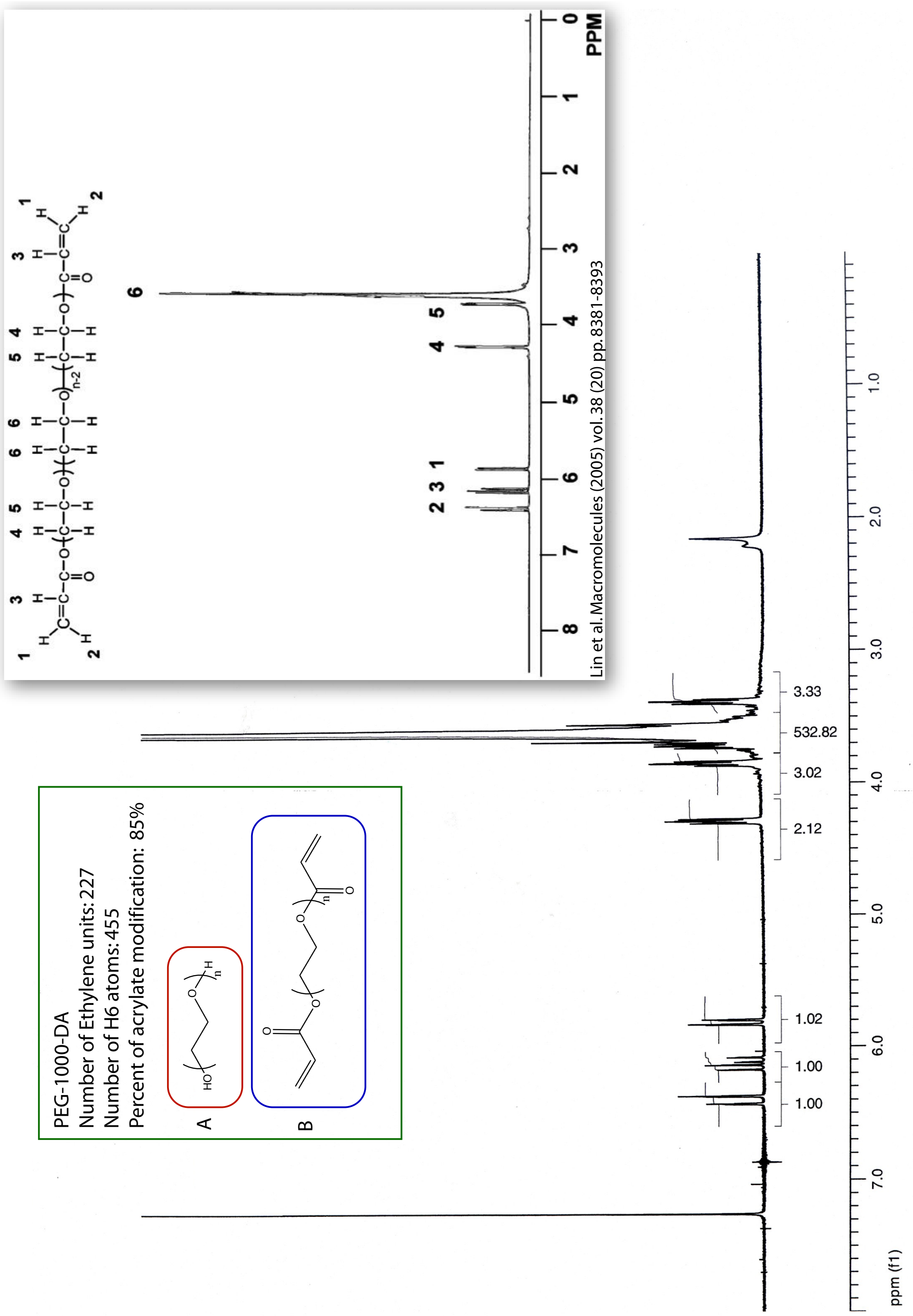

Figure A.1: ^{1}H-NMR spectrum obtained for PEG-DA.

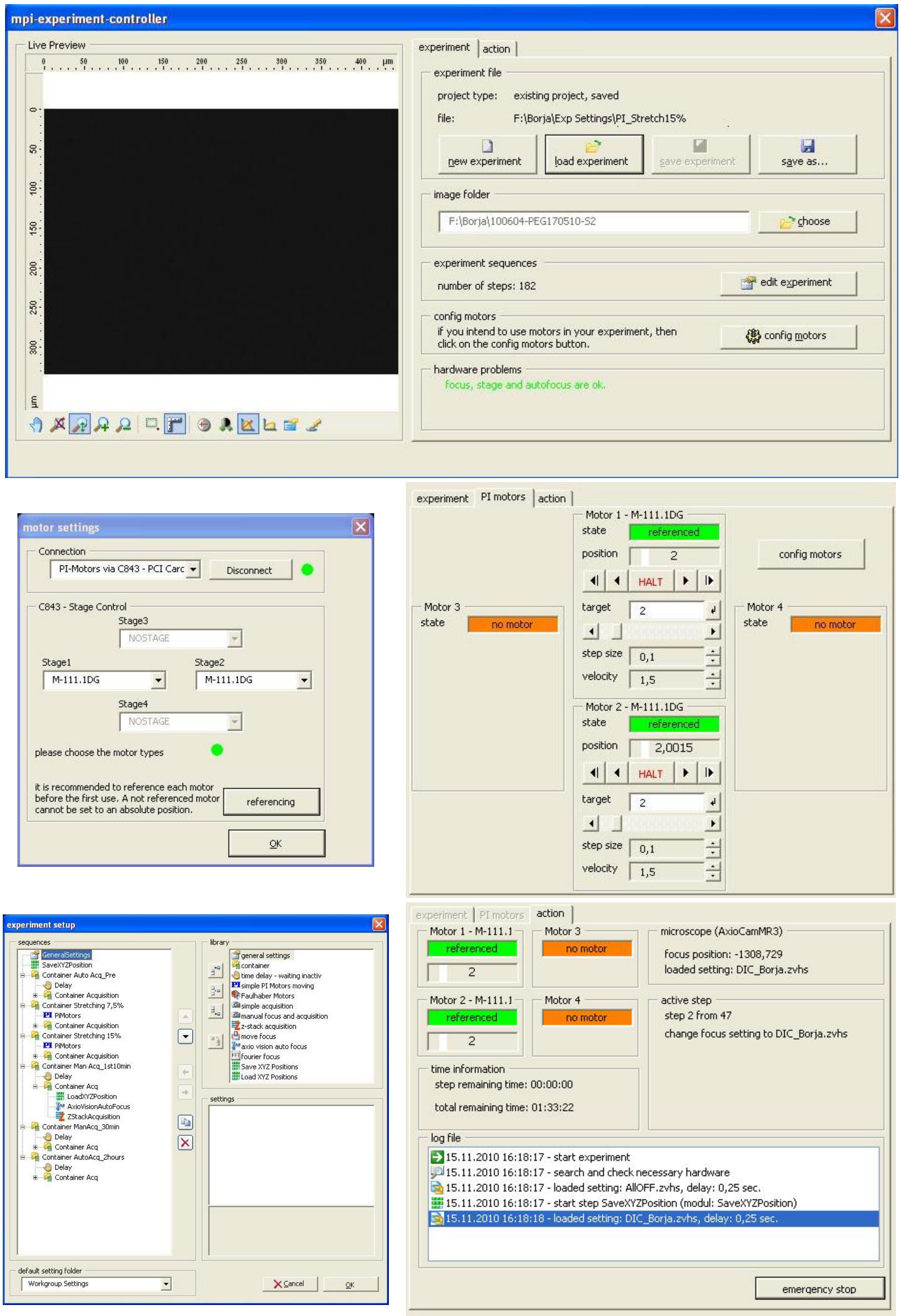

experiment file
project type: existing project, saved
file: F:\Borja\Exp Settings\PI_Stretch15%

image folder
F:\Borja\100604-PEG170510-S2

experiment sequences
number of steps: 182

config motors
if you intend to use motors in your experiment, then click on the config motors button.

hardware problems
focus, stage and autofocus are ok.

Connection
PI-Motors via C843 - PCI Carc

C843 - Stage Control
Stage3: NOSTAGE
Stage1: M-111.1DG
Stage2: M-111.1DG
Stage4: NOSTAGE

please choose the motor types

it is recommended to reference each motor before the first use. A not referenced motor cannot be set to an absolute position.

Motor 1 - M-111.1DG
state: referenced
position: 2
target: 2
step size: 0,1
velocity: 1,5

Motor 2 - M-111.1DG
state: referenced
position: 2,0015
target: 2
step size: 0,1
velocity: 1,5

Motor 3
state: no motor

Motor 4
state: no motor

sequences
- GeneralSettings
- SaveXYZPosition
- Container Auto Acq_Pre
  - Delay
  - Container Acquisition
- Container Stretching 7,5%
  - PiMotors
  - Container Acquisition
- Container Stretching 15%
  - PiMotors
  - Container Acquisition
- Container Man Acq_1st10min
  - Delay
  - Container Acq
    - LoadXYZPosition
    - AxioVisionAutoFocus
    - ZStackAcquisition
- Container ManAcq_30min
  - Delay
  - Container Acq
- Container AutoAcq_2hours
  - Delay
  - Container Acq

library
- general settings
- container
- time delay - waiting inactiv
- simple PI Motors moving
- Faulhaber Motors
- simple acquisition
- manual focus and acquisition
- z-stack acquisition
- move focus
- axio vision auto focus
- fourier focus
- Save XYZ Positions
- Load XYZ Positions

settings

default setting folder
Workgroup Settings

Motor 1 - M-111.1: referenced, 2
Motor 2 - M-111.1: referenced, 2
Motor 3: no motor
Motor 4: no motor

microscope (AxioCamMR3)
focus position: -1308,729
loaded setting: DIC_Borja.zvhs

active step
step 2 from 47
change focus setting to DIC_Borja.zvhs

time information
step remaining time: 00:00:00
total remaining time: 01:33:22

log file
```
15.11.2010 16:18:17 - start experiment
15.11.2010 16:18:17 - search and check necessary hardware
15.11.2010 16:18:17 - loaded setting: AllOFF.zvhs, delay: 0,25 sec.
15.11.2010 16:18:17 - start step SaveXYZPosition (modul: SaveXYZPosition)
15.11.2010 16:18:18 - loaded setting: DIC_Borja.zvhs, delay: 0,25 sec.
```

Figure A.2: Customized Visual Basic Applications Macro.

A.4 Strain Analysis

In order to check the homogeneity of the strain field on the HGs' surface an Autodesk Inventor Professional© strain field analysis was conducted (with the kind help of PhD student Martin Deibler). Results can be seen in figure A.3 as a color-coded distribution of the deformation along the length of the substrate. It can be clearly seen how the deformation increases gradually and uniform, being obviously highest at the points where the load is applied and lowest in the middle. It can be concluded from this analysis that in the center of the HGs the applied strain is homogeneous and that cells spread in this area will be subjected to similar levels of strain.

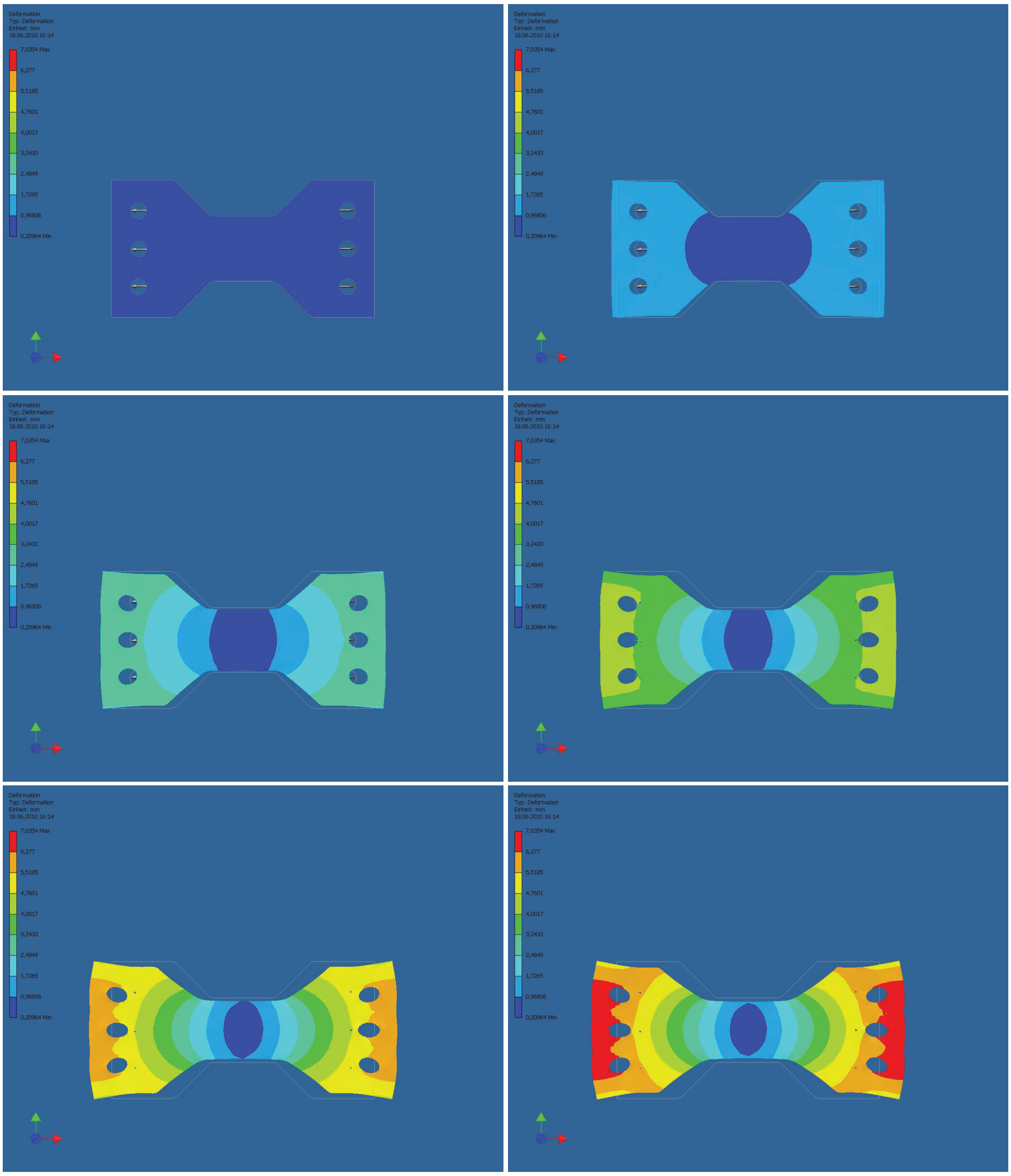

Figure A.3: Autodesk Inventor Professional© strain analysis.

A.5 Evolution in time of FAs' parameters discriminating between small and large particles

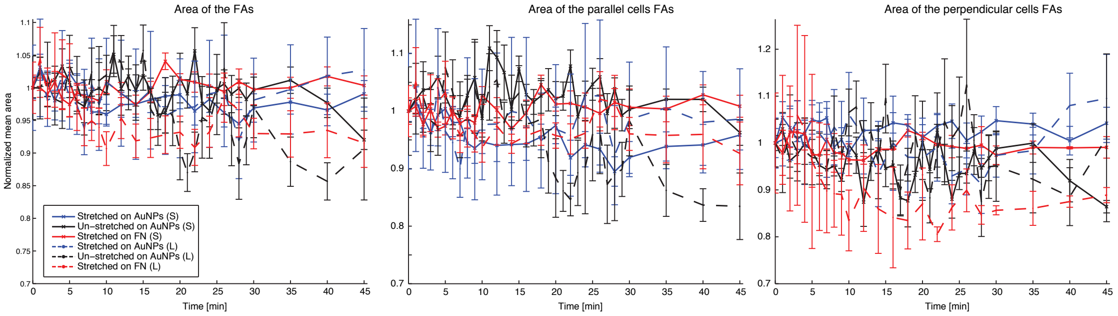

Figure A.4: Normalized mean area of the FAs subjected to uniaxial, static stretch. Blue line represents the evolution in time of the parameter in discussion of the FAs belonging to cells stretched on hydrogels patterned with AuNPs and bio-functionalized with the RGD linker (in the following FAs stretched on AuNPs). Black line represents the evolution in time of the parameter in discussion of the FAs belonging to cells seeded on hydrogels patterned with AuNPs and bio-functionalized with the RGD linker (in the following FAs un-stretched on AuNPs). Red line represents the evolution in time of the parameter in discussion of the FAs belonging to cells stretched on hydrogels homogeneously coated with FN (in the following FAs stretched on FN). Error bars refer to the standard error of the mean.

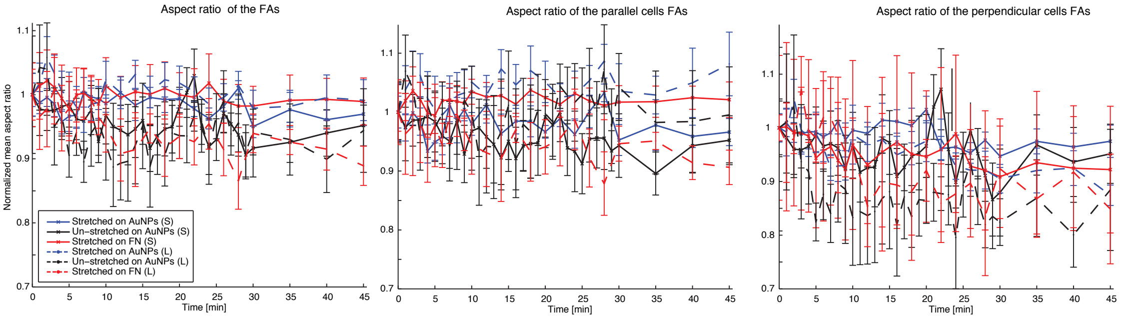

Figure A.5: Normalized mean aspect ratio of the FAs subjected to uniaxial, static stretch. Blue, black and red lines represent the same as in figure A.4. Error bars refer to the standard error of the mean.

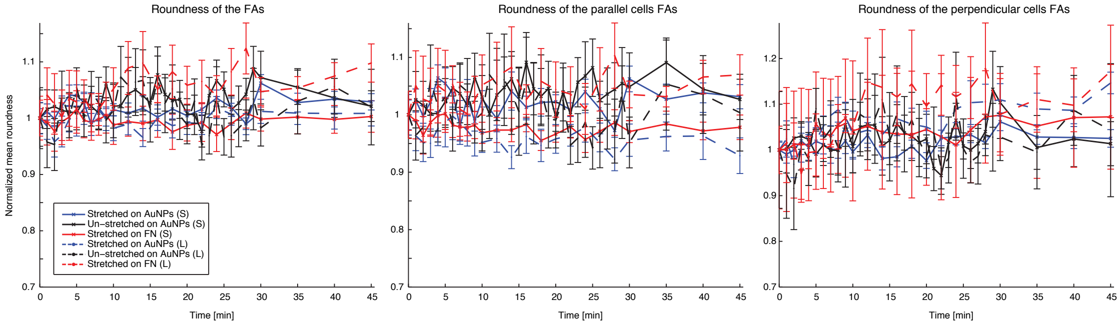

Figure A.6: Normalized mean roundness of the FAs subjected to uniaxial, static stretch. Blue, black and red lines represent the same as in figure A.4. Error bars refer to the standard error of the mean.

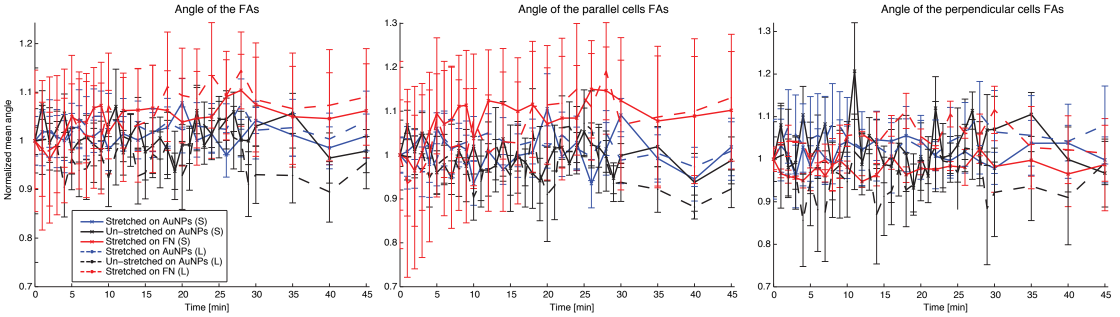

Figure A.7: Normalized mean angle to stretch axis of the FAs subjected to uniaxial, static stretch. Blue, black and red lines represent the same as in figure A.4. Error bars refer to the standard error of the mean.

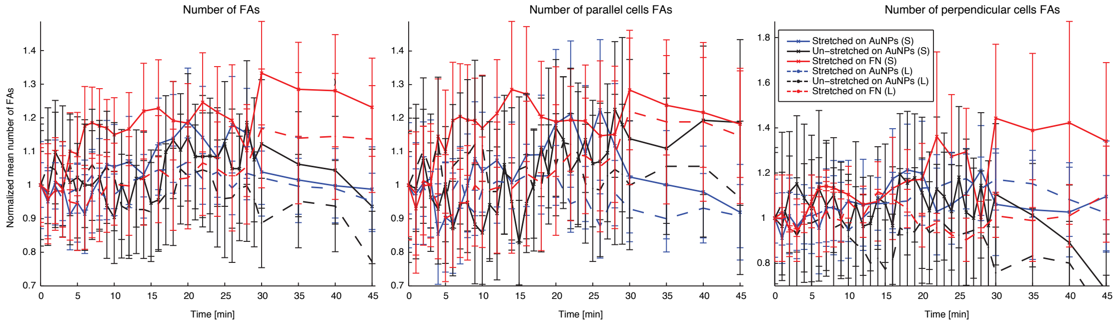

Figure A.8: Normalized mean number of FAs subjected to uniaxial, static stretch. Blue, black and red lines represent the same as in figure A.4. Error bars refer to the standard error of the mean.

A.6 List of publications

1 **Nanopatterned, elastic, ECM-mimetic substrates for cell adhesion studies under strain** (Borja Aragüés Rioja, Ralf Kemkemer, Joachim P Spatz), *In preparation.*

2 **Force-induced cell polarisation is linked to RhoA-driven microtubule-independent focal-adhesion sliding** (Alexandra M Goldyn, Borja Aragüés Rioja, Joachim P Spatz, Christoph Ballestrem, Ralf Kemkemer), *In J Cell Sci*, volume 122, 2009.

3 **Myoblast morphology and organization on biochemically micro-patterned hydrogel coatings under cyclic mechanical strain** (Wylie W Ahmed, Tobias Wolfram, Alexandra M Goldyn, Kristina Bruellhoff, Borja Aragüés Rioja, Martin Moller, Joachim P Spatz, Taher A Saif, Jurgen Groll, Ralf Kemkemer), *In Biomaterials*, 2009.

Ich erkläre hiermit, dass ich die vorgelegte Dissertation selbst verfasst und mich keiner anderen als der von mir ausdrücklich bezeichneten Quellen und Hilfen bedient habe.

Heidelberg, den 20. Mai 2011

....
Borja Aragüés